Universitetet i Stavanger

FACULTY OF SCIENCE AND TECHNOLOGY

MASTER'S THESIS

Study program/Specialization: Petroleum Engineering Drilling and Well Technology	Spring semester, 2018 Confidential
Author: Linn Engan Karlsen	…… (signature of author)

Faculty supervisor: Mesfin Belayneh

External supervisor: Ola M. Vestavik

Thesis title:

Experimental Investigation of Heavy over Light Fluid Mix Phenomena in Vertical Wells

Credits (ECTS): 30

Key words: Heavy over Light Solution Mixing zone Reelwell Drilling Method Extended Reach Drilling Experimental work Multivariate Regression	Number of pages: 99 + Appendixes: 26 Stavanger, 14.06.2018

ABSTRACT

The Heavy over Light (HOL) solution, invented by Reelwell, is a main feature of the Reelwell Drilling Method (RDM) and has the potential to improve the capability to drill through challenging pressure zones. This solution can reduce torque and drag and enable Managed Gradient Drilling (MGD) operations to be performed with little to no wellhead pressure. MGD is an advanced version of Managed Pressure Drilling (MPD) and can provide a constant downhole pressure gradient.

The RDM solution is comprised of using a dual drill string for improved downhole pressure measurement and control. This solution utilizes a passive heavy fluid in the well annulus and an active light fluid for cleaning the well. The MGD performance depends the ability to control the mixing zone between these two fluids during the operations.

The HOL solution in the horizontal sections was verified by Reelwell in a test well in Canada in 2016, but the vertical section still remains to be investigated and verified.

This thesis presents a thorough investigation of the HOL mixing zone in the vertical section of experimental wells. Experiments with different fluid properties and various well diameters has been conducted and the relation between these parameters and the mixing zone length is presented.

The experimental result showed that both the clearance between the well and the drill string and the lower shear yield stress (LSYS) of the light fluid have effects on the mixing zone length. This is also confirmed by theory. Critical values for $\Delta\rho$, ΔPV and for the viscoelastic ratio, $(H_{G'} - L_{G'})/(H_{G''} - L_{G''})$, where the mixing zone is short and stable below these values, have been observed. In addition, the mixing zone as a function of a correlation factor is presented and multivariate regression models have been developed. Finally, it is shown good comparison between the models and the experimental data. For further work, it would be preferable to perform a greater amount of experiments with larger well diameters and longer well pipes.

ACKNOWLEDGEMENTS

I want to thank all the people who have supported me throughout the whole process of writing this thesis.

First of all, I want to thank my faculty supervisor, Professor Mesfin Belayneh. His academic knowledge, guidance and help has really been helpful though the whole writing process.

I would also like to express my gratitude to my external supervisor, Ola M. Vestavik from Reelwell, for giving me the opportunity to write this thesis and for all his help and guidance. Our regular meetings have been very helpful and motivating.

I addition, I also appreciate the theoretical and academic help provided by Professor Rune Time. His knowledge has been highly valuable.

Last, but not least, I would like to thank my family and friends for all the love and support through all my years of studying.

Stavanger, June 2018

Linn Engan Karlsen

TABLE OF CONTENTS

LIST OF FIGURES

FIGURES IN APPENDIX

LIST OF TABLES

TABLES IN APPENDIX

ABBREVIATIONS

AV	Apparent viscosity
ECD	Equivalent Circulating Density
ERD	Extended Reach Drilling
HB	Herschel Bulkley
HOL	Heavy over Light
KH	Kelvin-Helmholtz
LSYS	Lower Shear Yield Stress
MGD	Managed Gradient Drilling
MPD	Managed Pressure Drilling
PV	Bingham Plastic viscosity
RDM	Reelwell Drilling Method
RPM	Rounds per Minute
RTI	Rayleigh-Taylor Instability
SG	Specific Gravity
WOB	Weight on Bit
YP	Yield Point
YS	Yield Stress

1 INTRODUCTION

This thesis presents an experimental investigation of the Heavy over Light mixing zone in the vertical section of Reelwell drilling method. The thesis will focus on the length of the mixing zone in relation with well diameter and different fluid properties.

1.1 BACKGROUND

The oil industry is always searching for new technology and methods that extends the length of the wells. Directional drilling of very long horizontal wells is called Extended Reach Drilling (ERD). ERD makes it possible to reach larger areas from one drilling location and thus maximize productivity and drainage capability [R1]. Figure 1.1 shows the extended reach drilling envelope. The current ERD record is a well drilled in the Shaklin 1 consortium in Russian with 15000 m measured depth [T24]. The limiting factor the reaching to a longer offset is due to high torque and drag so that the axial load transfer to bit not be sufficient to drill ahead.

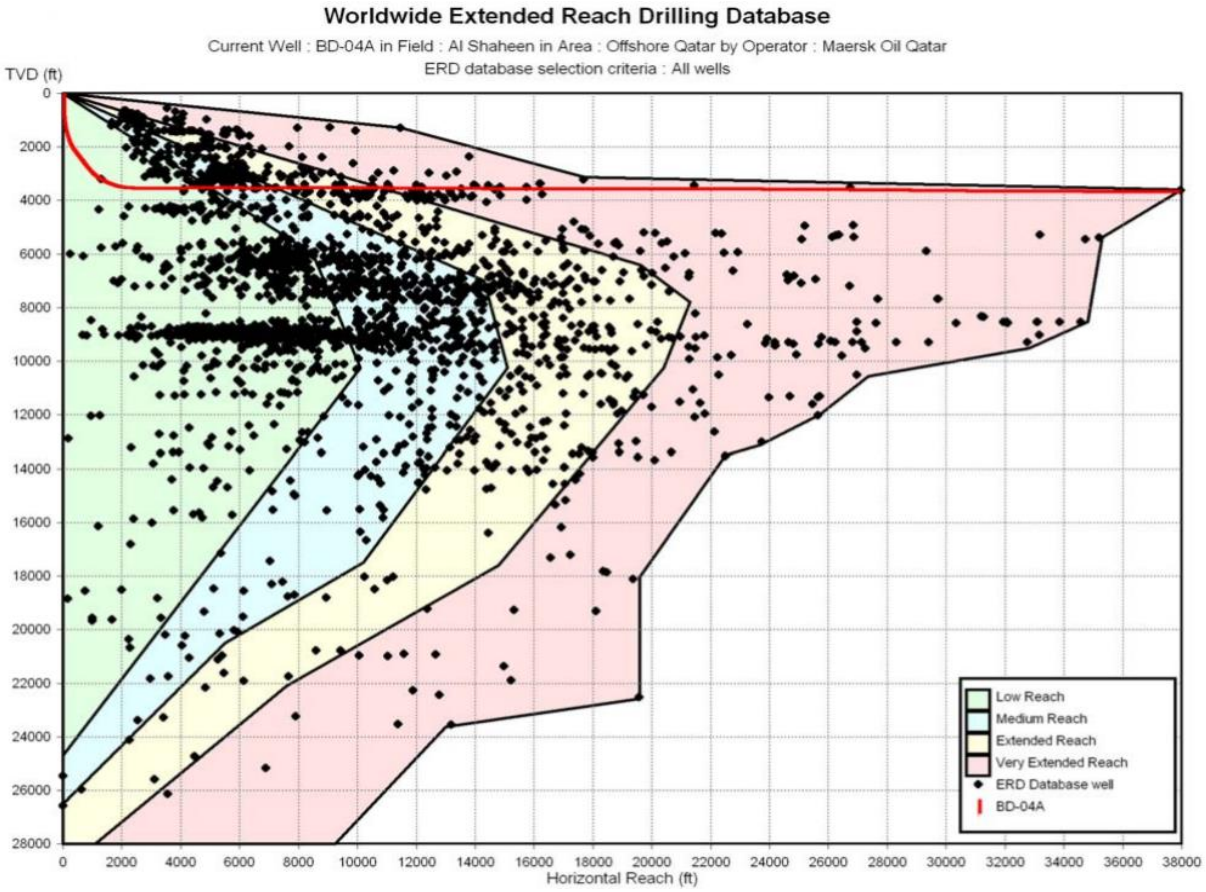

Figure 1.1 - Extended Reach Drilling Envelope [F01]

In order to overcome the challenges associated with the conventional ERD, Reelwell has developed a new drilling concept called Reelwell Drilling Method (RDM). RDM combines Managed Pressure Drilling (MPD) and liner drilling, using a dual drill string with a separate inner pipe for the return fluid from the well [R2]. Due to torque and drag reduction, elimination of dynamic equivalent circulating density (ECD) gradient and operational hydraulic weight on bit (WOB), RDM has the potential to increase the envelope for ERD. Figure 1.2 shows the comparison between the conventional drilling method and the RDM. Unlike the conventional method, the cutting transport in RDM is through a dual pipe. Mechanically, the dual string carries more buckling load than the conventional method.

One of the main features of RDM is the Heavy over Light (HOL) operation and is explained more closely in section 2.2. In short, HOL utilizes a heavy drilling fluid on top of a lighter drilling fluid when drilling. It is expected that a mixing zone will occur in the interface between these two fluids and this phenomenon is what this thesis investigates.

The HOL solution has been studied in three earlier master theses. An experimental study carried out by Eirik Aasberg Vandvik in 2014 investigated several parameters that influenced the dynamics of the heavy light interface and the resulting mixing zone in a horizontal well [T15]. An experimental study of weight particle sagging in horizontal sections was investigated by Magne Hurum in 2015 [T16] and in 2016, Anne May Haaland investigated the HOL solution in vertical sections of a well through simulations using the COMSOL Multiphysics software and experimental work [T17].

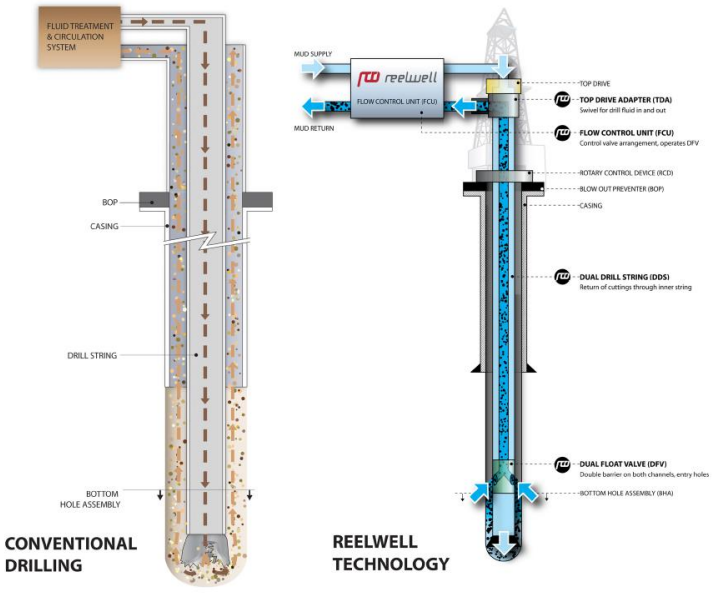

Figure 1.2 – Conventional vs. RDM flow arrangements [F07]

1.2 PROBLEM FORMULATION

For realization of the Reelwell concept, HOL operation in the horizontal section was verified in a test well in Canada by Reelwell in 2016. However, in field scale, Reewell has not yet evaluated the stability of HOL in the vertical section, see figure 1.3. As a part of the technology research and development, this MSc thesis has been designed to study the stability in the vertical section. For this, a small scale experimental rig has been built in the UiS laboratory. The issues related to stability to be addressed are:

- Effect of fluid properties (density and rheological)
- Effect of clearance
- Effect of operational parameters

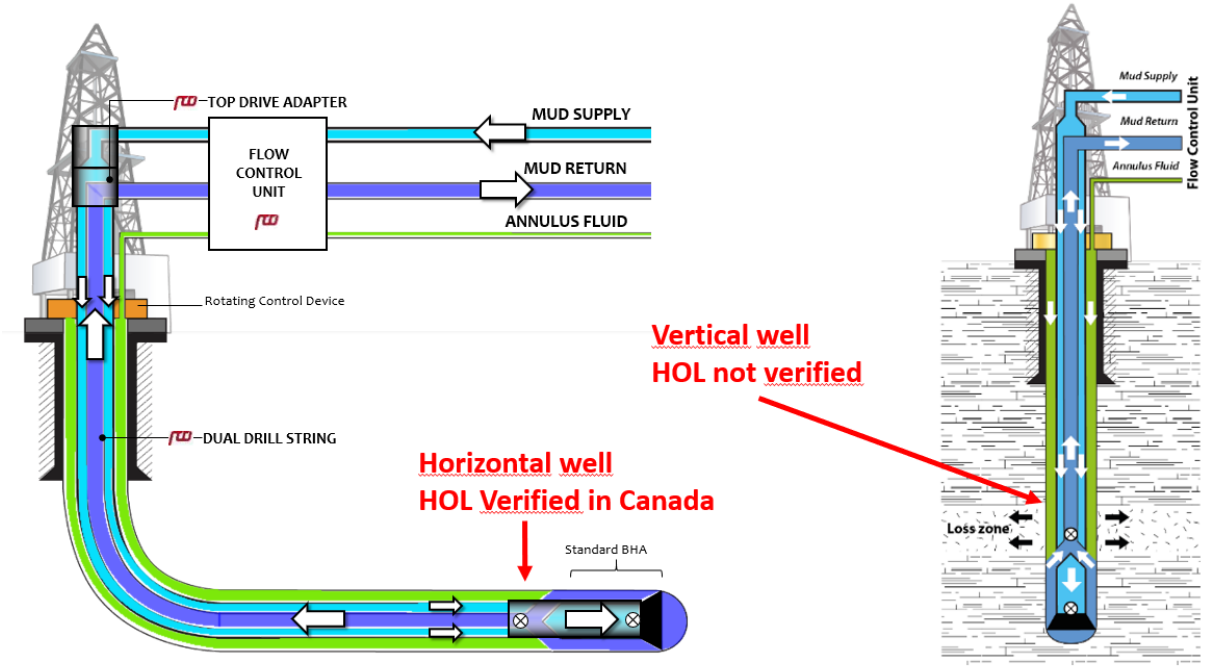

Figure 1.3 - Heavy over Light Fluid Solution [F03]

1.3 ASSUMPTIONS

Field operational conditions and thermodynamics states are difficult to simulate during the experimental studies. The experiments therefore will be conducted under simplified laboratory conditions with the objective obtaining an indication of the mix phenomenon. The assumptions and experimental conditions to consider are the following:

- Experiments are performed at room temperature and pressure. Therefore, no effect on the rheological properties and density of the drilling fluid from the surrounding environments are considered.
- Cuttings effects are not considered.
- Concentric and unbuckled drill string, no cavities or gaps.
- Wellbore instability problems such as unconsolidated formations, collapse etc. are not taken into account. Therefore, uniform wellbore is considered.
- Water-based laboratory formulated fluids with various physical and rheological properties are considered.

1.4 OBJECTIVE

The objective of this thesis is to investigate the heavy over light fluid mix dynamics and stability phenomenon in a vertical well under various well geometry/pipe ratio and drilling fluid properties. The activities are:

- Formulate various heavy and light drilling fluids and characterize their physical and rheological properties.
- Perform experiments that investigates the fluid mix phenomena and stability at the interface under different operational parameters.
- Investigate the main stability controlling parameters.
- Investigate if there exist a correlation between the mixing zone lengths with the single and/or combined drilling fluid parameters.
- Investigation of mixing zone length with picture processing and visual inspection.

From the overall study, results are believed to provide an improved understanding of the nature of the fluid mixing and help to design the right drilling fluid properties for further field case verification.

2 REELWELL TECHNOLOGY

Reelwell is an innovative Norwegian drilling technology company based in Stavanger. The company has developed a new drilling method for Extended Reach Drilling (ERD) called Reelwell Drilling Method (RDM).

2.1 CONCEPT AND BENEFITS

Drilling of long horizontal wells has proven to be challenging with respect to hole cleaning, ECD and torque and drag on the drill string. As illustrated in figure 2.1, where the window for downhole pressure is narrow, the dynamic ECD limits the length of the open hole section, and the result is that several liners or casings must be used to reach target depth. By incorporating a dual drill string with a separate inner channel for return fluid, this enables Managed Gradient Drilling (MGD). Unlike the conventional dynamic gradient, MGD is drilling with a constant downhole pressure gradient that can be controlled to be nearly independent of the flow rate. This enables efficient hole cleaning and reduction in torque and drag on the drill string due to buoyancy [R4].

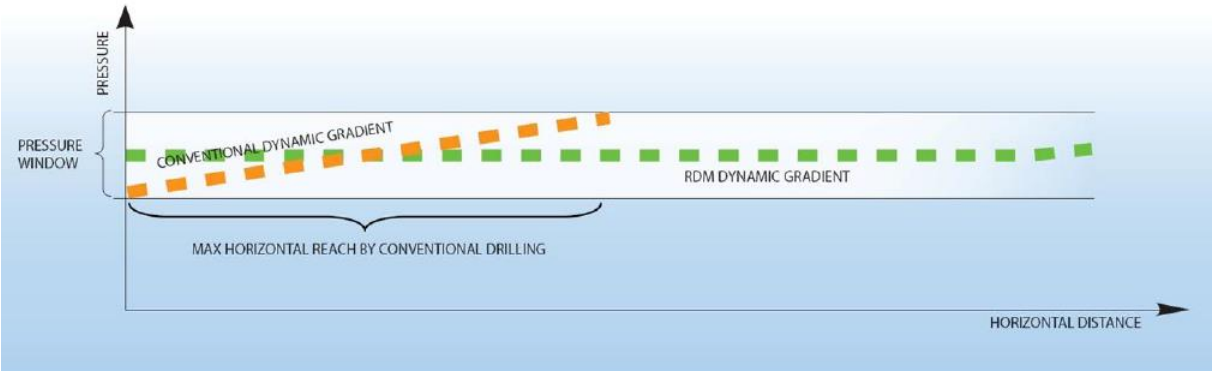

Figure 2.1 - Drilling with RDM and Conventional Method [R5]

2.2 HEAVY OVER LIGHT (HOL)

One of the main features of RDM is the "Heavy over Light" (HOL) operation. The HOL operation utilizes two separate drilling fluids, where the annular well fluid has higher density than the active fluid inside the drill string. The annular well fluid is passive and is used to control the well pressure. The active fluid inside the drill string is used for hole and bit cleaning [R3]. This arrangement is shown in figure 2.2 and enables Managed Gradient Drilling (MGD). This is said to be the advanced version of MPD. The difference is that the downhole pressure gradient is controlled instead of the pressure at one depth [R4].

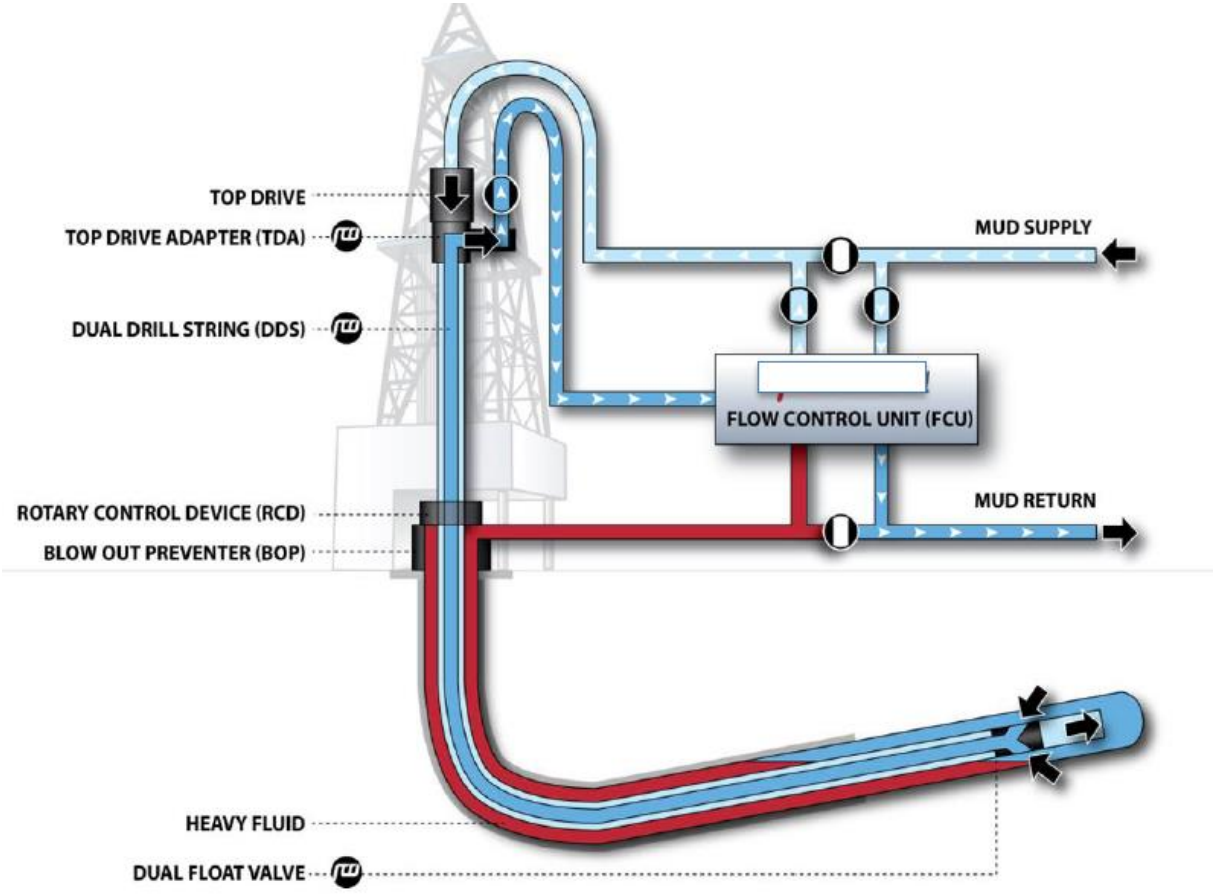

Figure 2.2 - Reelwell Drilling Method with HOL solution [R03]

3 THEORETICAL STUDY

This chapter presents theories directly or indirectly associated with Heavy over Light mixing of fluids.

3.1 DENSITY

Density is one of the characteristic property of drilling fluid. The density of a fluid describes the relationship between the mass of the fluid and how much volume (space) it takes up. Density can be expressed in three different ways: mass density, specific weight and specific gravity.

The mass density is defined as *mass per unit volume*,

$$\rho = \frac{m}{V}, \tag{3.1}$$

where ρ is the mass density,

m is the mass of the substance and

V is the volume of the substance.

Specific weight is a force which is defined as *weight per unit volume* [T01] and is expressed as

$$\gamma = \rho a_g, \tag{3.2}$$

where γ is specific weight,

ρ is density and

a_g is the acceleration of gravity, usually 9,81 m/s^2.

Specific gravity, or relative density as it is also called, is defined as *the ratio of the density of a substance to the density of water at a specified temperature* [T01]. Specific gravity is expressed as

$$SG = \frac{\rho_{substance}}{\rho_{water}}, \tag{3.3}$$

where SG is specific gravity,

$\rho_{substance}$ is the density of the fluid or substance [kg/m^3] and

ρ_{water} is the density of water [kg/m^3], usually at 4 ^{o}C.

Specific gravity is dimensionless [T01].

3.2 GRAVITY

Newton's law of gravitation states that the gravitational force is directly proportional to the product of two masses and inversely proportional to the square of the distance between them [T02].

In a HOL situation, the fluid with the greatest density will be exposed to higher gravitational force. This will result in positioning of the fluid with higher density below the fluid with lower density, i.e. the opposite of what is desired in this thesis.

3.3 BUOYANCY

When an object is placed in a fluid, the buoyancy equals the weight of the displaced fluid. Buoyancy is a surface force that acts in the opposite direction of the gravitational force. Thus, it is only the pressure acting on the projected vertical area that contributes to buoyancy [T03].

For buoyancy in boreholes, the buoyancy factor is defined as the suspended weight in mud divided by the weight in air. The following equation is valid for both vertical and deviated wells when the fluid inside and outside the pipe has the same density [T03]:

$$\beta = 1 - \frac{\rho_{fluid}}{\rho_{pipe}}, \tag{3.4}$$

where β is the buoyancy factor,

ρ_{fluid} is the density of the surrounding fluid and

ρ_{pipe} is the density of the pipe material.

If the fluid density inside and outside the pipe is different from each other, the equation will be

$$\beta = 1 - \frac{\rho_o r_o^2 - \rho_i r_i^2}{\rho_{pipe}(r_o^2 - r_i^2)}, \tag{3.5}$$

where ρ_o is the density of the outer fluid,

r_o is the inner radius of casing or wellbore,

ρ_i is the density of the inner fluid and

r_i is the inner radius of the drill pipe [T03].

3.4 ROTATIONAL FORCE

When the drill string rotates, the angular velocity creates a rotational force. As seen on figure 3.1, the deformation of the fluid will be greatest at the drill pipe wall and will decrease as we move away from the drill pipe wall [T04].

The shear rate and the angular velocity are given by

$$\gamma = \frac{\omega r_{DP}}{r_w - r_{DP}}, \tag{3.6}$$

where γ is the shear rate,

ω is the angular velocity,

r_{DP} is the drill pipe radius and

r_w is the wellbore radius.

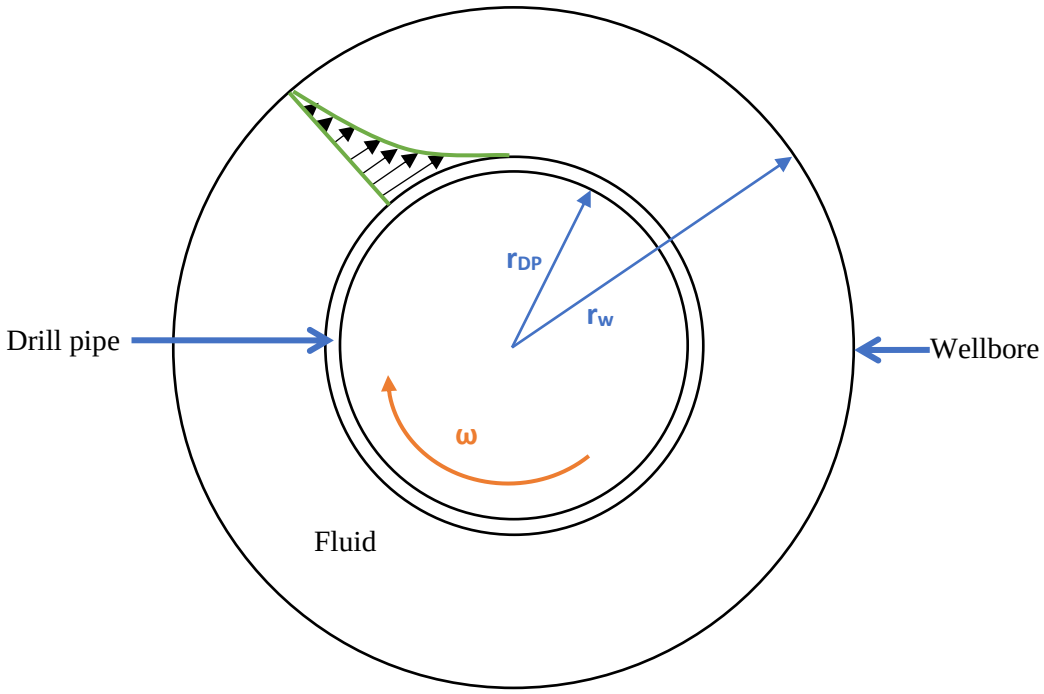

Figure 3.1 - Cross section of a rotating drill pipe [F04]

3.5 CENTRIFUGAL FORCE AND CENTRIPETAL FORCE

The centripetal force is acting on the substance causing it to move in a circular path (see figure 3.2) and is expressed as

$$F = m \cdot \frac{v^2}{r}, \tag{3.7}$$

where m is the mass of the substance,

v is its constant speed and

r is the radius of the circle.

Here, the speed is constant, but the velocity is changing due to the direction which is constantly changing. An acceleration, $\frac{v^2}{r}$, is therefore directed towards the centrum of the circle. [T05]

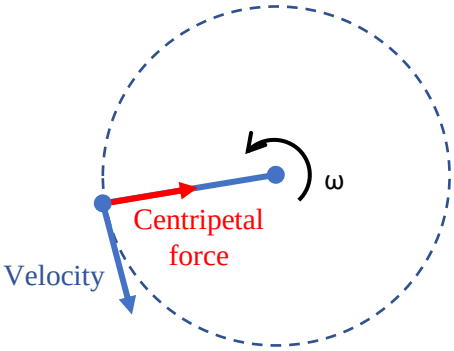

Figure 3.2 - Centripetal Force [F04]

When a cylindrical container filled with a fluid is rotated about its axis, the fluid is forced outwards due to the centrifugal force [T06].

In the HOL fluid mixing zone, the fluid with the highest density will be more affected by the centrifugal force than the fluid with lower density. Therefore, in theory, the heavy fluid will be forced outward toward the wall like shown in figure 3.3.

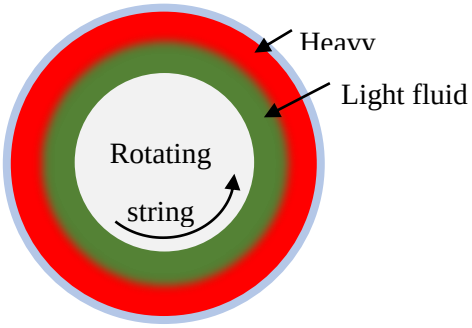

Figure 3.3 - Cross-section of a HOL mixing zone under influence of centrifugal force [F04]

3.6 FLUID MIXTURE

A paper about mixing of influx fluid and drilling fluid during a kick was published by Ejve and Fjelde [T07] in 2002. This paper presents an equation for density mixing of two fluids with different densities as:

$$\rho_{mix} = \rho_g \alpha_g + (1 - \alpha_g)\rho_l, \tag{3.8}$$

where ρ_{mix} is the density of the mixed fluid,

ρ_g is the density of the influx fluid,

ρ_l is the density for the drilling fluid and

α_g is the fraction of influx fluid in the mixture.

This can easily be transformed into an equation for density mixing of heavy and light fluid;

$$\rho_{mix} = \rho_{light} \alpha_{light} + (1 - \alpha_{light})\rho_{heavy}, \tag{3.9}$$

where ρ_{heavy} is the density of the heavy fluid,

ρ_{light} is the density for the light fluid and

α_{heavy} is the fraction of heavy fluid in the mixture.

Figure 3.4 illustrates the fluid mix behavior, which is a linear function of the volume fraction of the heavy and light fluids. Assume that the density of the heavy fluid is 1.6 sg and the density of the light fluid is 1.5 sg. As a certain fraction of light fluid mixing with the heavy fluid, the density of fluid mix reduces linearly.

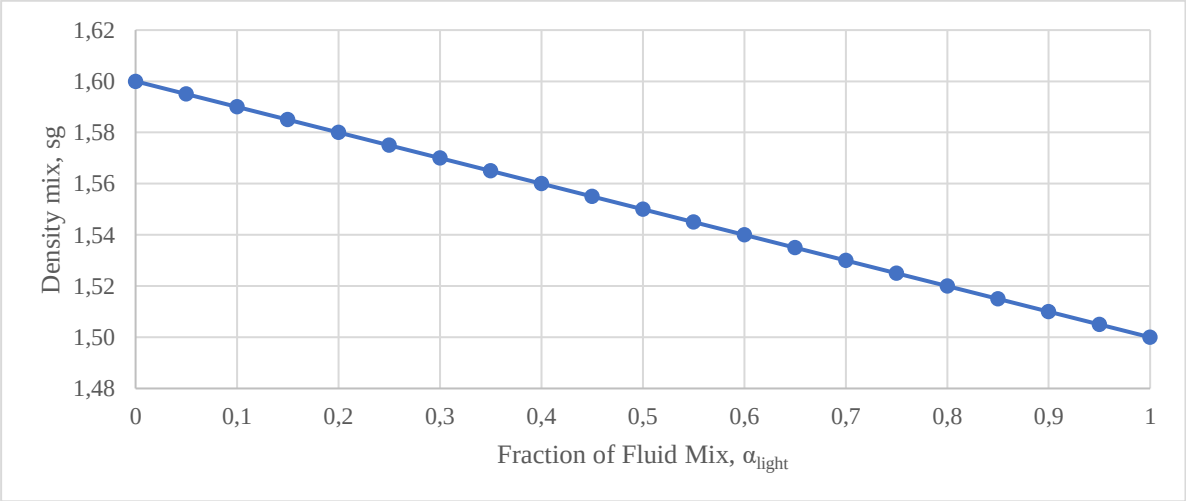

Figure 3.4 - Illustration of Fluid Mixture [F04]

3.7 STOKES LAW

An object placed in a fluid flow experiences a force from the flowing fluid acting on the object. This force is called the drag force and is acting in the flow direction. The drag force comes from the frictional effects combined with the difference in pressure on the two sides of the object and is expressed as [T08]:

$$F = C_D A \frac{\rho V^2}{2} \tag{3.10}$$

where F is the drag force,

C_D is the coefficient of drag,

V is the free stream velocity,

A is the projected area of the object and

ρ is the density of the fluid.

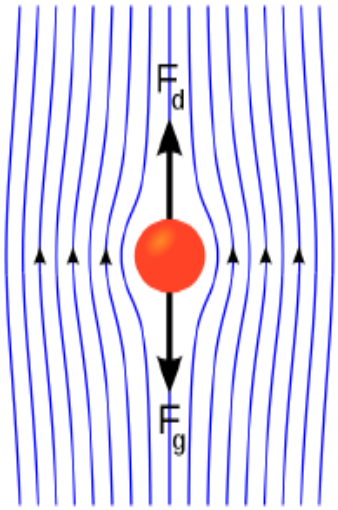

Figure 3.5 – Drag force on a spherical object suspended in viscous fluid [F08]

The drag force for a spherical object falling in a fluid with a constant velocity (figure 3.5) is equal to the submerged weight of the sphere:

$$F = C_D \left(\frac{\pi D^2}{4}\right) \frac{\rho V^2}{2} = \frac{\pi}{6} D^3 g(\rho_s - \rho_f), \tag{3.11}$$

where D is the diameter of the sphere,

ρ_s is the density of the material of the sphere and

ρ_f is the density of the fluid.

C_D varies with the Reynolds number for a given shape of the object. For a spherical object the drag coefficient is set to:

$$C_D = \frac{24}{Re} \quad (for\ Re \leq 1). \tag{3.12}$$

The drag force is then expressed as:

$$F = 3\pi D\mu V, \tag{3.13}$$

where μ is the viscosity [T08].

When balancing equation (3.11) and (3.13), Stokes settling velocity can be given as:

$$V_s = \frac{D^2 g(\rho_s - \rho_f)}{18\mu}. \tag{3.14}$$

3.8 RHEOLOGY

Rheology is the study of deformation and flow of fluids and solids. The rheological properties of the drilling fluids are extremely important for the drilling fluids functions [T09].

There are several rheological models in literature which are developed to characterize the fluid's shear stress as a function of shear rate. Models and measured viscometer response of the drilling fluids are used in order to quantify the rheological properties of a drilling fluid such as yield strength, viscosity and gel strength. These properties determine the fluid flow behavior. In this thesis, the focus is especially on the dynamics of the heavy over light fluid mixing at their interface.

During drilling operations, the rheological properties determine the hydraulics and cutting /solid suspension and transport efficiency.

Figure 3.6 illustrates the shear stress - shear rate of Newtonian and non-Newtonian fluid. The drilling fluid prepared in this thesis work are not described by Newtonian fluids since the fluid systems consists of particles. All the drilling fluids behaves as real plastic/yielded plastic model, which is a modified power law model called Herschel Bulkley. Therefore, for the evaluation of mixing zone with respect to rheological properties, both Bingham plastic and yield stress have been used [T20].

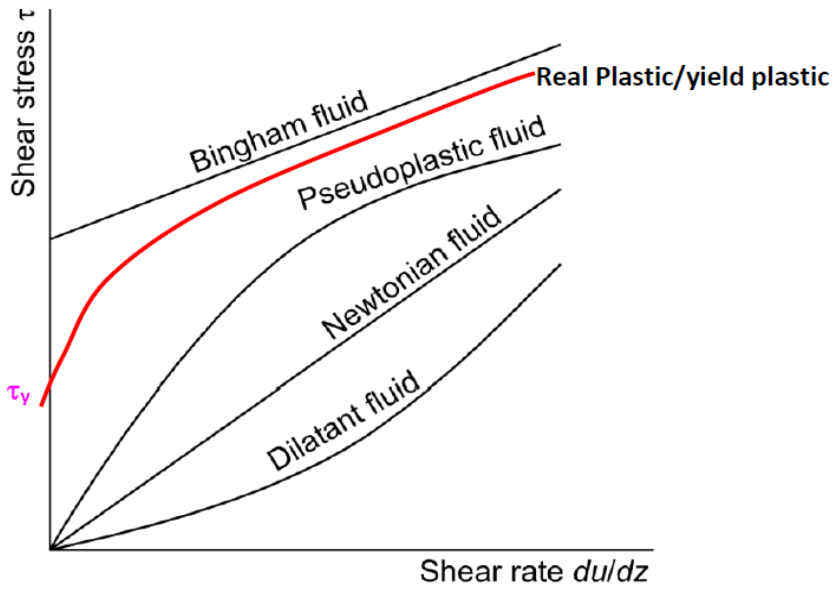

Figure 3.6 - Illustration of shear stress - shear rate behavior of fluids [F06]

3.8.1 BASIC PRINCIPLE

Assume that there are two layers of fluids with contact area *A*. The fluids move in same direction but with different velocities. The two layers with distance *y* move with a velocity *v* and *v* + *dv*. Due to the liquids resistance to flow, a force F is applied between the two layers. The shear stress will then be [T09]:

$$\tau = \frac{F}{A} \text{ [Pa] or [N/m}^2\text{]}, \tag{3.15}$$

and the shear velocity:

$$\dot{\gamma} = \frac{dv}{y} [s^{-1}]. \tag{3.16}$$

The viscosity can then be expressed as:

$$\mu = \frac{\tau}{\dot{\gamma}} \text{ [Pa·s]}. \tag{3.17}$$

3.8.2 VISCOSITY

Viscosity is the resistance of a fluid to flow, or the inner friction of the fluid. The resistance to flow occurs due to friction force between the various components in the fluid and because of electrostatic forces between electrically charged particles or ions. The viscosity depends on the following factors [T09]:

- Temperature
- Pressure
- Shear rate
- Time
- Physical/chemical nature

Flow properties of drilling muds are often characterized by the following measurements:

- Plastic viscosity
- Yield point
- Gel strength
- Apparent viscosity
- Marsh Funnel viscosity

Gel Strength

The gel strength expresses the thixotropic properties of the fluid, i.e. that the shear stress is no longer constant for a stated rate but will change with shear time. Gel strength is related to additive forces between the particles in the drilling mud when the fluid is at rest. Gel strength is measured as a function of time [T09].

Apparent Viscosity (AV) and Marsh Funnel Viscosity

Apparent viscosity and Marsh Funnel viscosity provides a measurement of the total viscosity of the fluid. It is influenced by both plastic viscosity, yield point and gel strength. This is only used as a control parameter for drilling muds [T09].

3.8.3 BINGHAM PLASTIC MODEL

To be able to describe a liquid, different mathematical models have been developed. The Bingham plastic model is a two-parameter model, which describes liquids containing suspensions of solids and that have a yield point. The shear stress varies linearly with shear strain as shown in figure 3.7. The model reads:

$$\tau = YP + PV\dot{\gamma}, \tag{3.18}$$

where PV is the Bingham plastic viscosity [cP] and

YS is the Bingham yield stress (lbf/100ft^2);

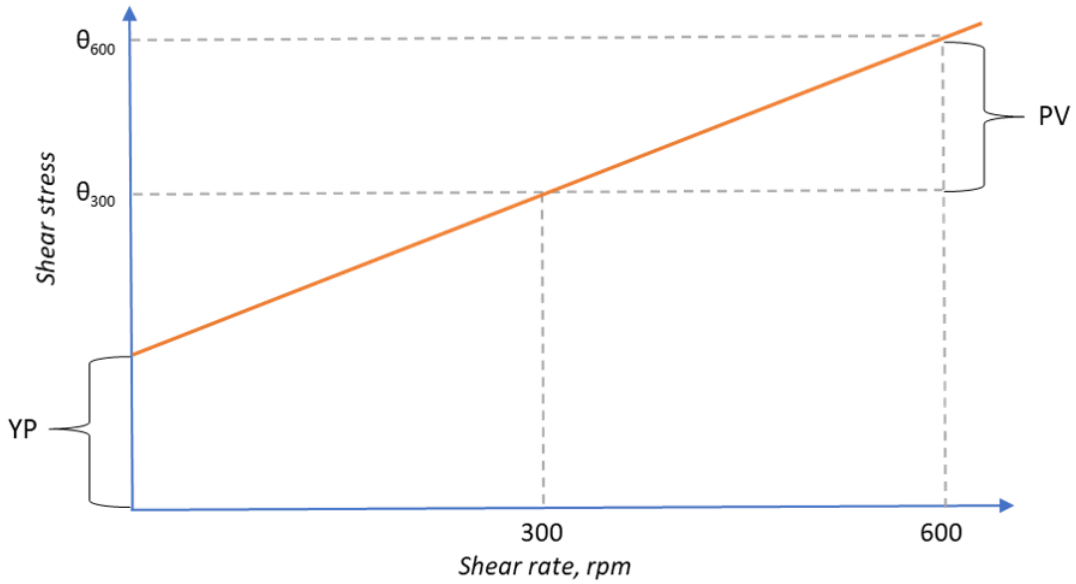

Figure 3.7 - Bingham Plastic Model [F01]

The model parameters are determined based on two measurements from a Fann viscometer at 600 rpm and 300 rpm. From this, the rheological properties of a fluid can be calculated [T09].

Apparent Viscosity (AV)

The relationship between shear stress and shear rate is the apparent viscosity of a Bingham fluid. The apparent viscosity may be expressed by the following equation [T09]:

$$AP = \frac{300 \cdot \theta_{rpm}}{RPM} \quad [cP]. \tag{3.19}$$

Usually, the apparent viscosity is calculated from measurements at 600 rpm;

$$AP = \frac{\theta_{600}}{2} \quad [cP]. \tag{3.20}$$

Plastic Viscosity (PV)

Plastic viscosity is one of the properties of a drilling fluid which describes the resistance to flow. This part is caused by mechanical friction among particles in a fluid, and fluid - particle and fluid elements. There are several parameters that influences the viscosity of the fluid.

The plastic viscosity of a Bingham fluid is represented by the slope of figure 3.7, calculated as [T09];

$$PV = \theta_{600} - \theta_{300}, \qquad [cP]. \tag{3.21}$$

where, θ_{600} and θ_{300} are the reading of a viscometer at 600 RPM and 300 RPM shear rate, respectively.

Yield Point (YP)

The Yield stress/Yield point of a drilling fluid is a part of the flow resistance. It is caused by the electrostatic force of attraction of drilling fluid additives. There are several factors that influences the yield stress value. During this thesis work in addition to water, lignosulfonate has been used to regulate and to obtain a desired yield stress.

Graphically, the intercept of the shear stress - strain (figure 3.7) determines the Bingham Plastic yield stress. From the viscometer data, the yield stress is determined from equation 3.22 as [T09];

$$YP = \theta_{300} - PV = (2 \cdot \theta_{300} - \theta_{600}), \qquad [lbs/100ft^2]. \tag{3.22}$$

3.8.4 HERSCHEL BULKLEY MODEL

Among the non-Newtonian models, drilling fluids behaves as shear thinning and yielded power law type rheology model, which is called Herschel Bulkley. The model describes the viscometer data of the drilling fluids formulated in this thesis work best. Herschel Bulkley is a three-parameter model and the model reads [T09]:

$$\tau = \tau_y + K\dot{\gamma}^n \tag{3.23}$$

or

$$log(\tau - \tau_y) = log\, K + n\, log\, \dot{\gamma} \tag{3.24}$$

where τ_y = yield stress

γ = shear rate

n = flow index

K = consistency index

The yield stress is determined from low shear rate as provided in eq. 3.26

$$\tau_y = 0{,}511 \cdot \theta_0 \ [Pa], \tag{3.25}$$

$$\theta_0 = [2 \cdot \theta_3 - \theta_6]. \tag{3.26}$$

Equation (3.24) shows that K is determined graphically from the measured data when the shear rate is 1, regardless of the n value. K is connected to the viscosity of the fluid.

The flow index n describes the deviation from a Newtonian fluid. The lower n is, the more shear thinning the fluid is. The value of K and n is found from the following equations:

$$n = \frac{log\left(\frac{\tau_1 - \tau_y}{\tau_2 - \tau_y}\right)}{log\left(\frac{\dot{\gamma}_1}{\dot{\gamma}_2}\right)}, \tag{3.27}$$

$$K = \frac{\tau_1 - \tau_y}{\dot{\gamma}_1^n} = \frac{\tau_2 - \tau_y}{\dot{\gamma}_2^n} = \frac{\tau - \tau_y}{\dot{\gamma}^n}, \ [Pa \cdot S^n]. \tag{3.28}$$

By measuring the shear stress at two different shear rates (600 and 399 rpm (1022 and 511 s^1)), equation (3.27) and (3.28) can be solved. n and K can be expressed as

$$n = \frac{log\left(\frac{\theta_{600} - \theta_0}{\theta_{300} - \theta_0}\right)}{log\left(\frac{1022}{511}\right)} = 3{,}32\, log\left(\frac{\theta_{600} - \theta_0}{\theta_{300} - \theta_0}\right), \text{ and} \tag{3.29}$$

$$K = 0{,}511\left(\frac{\theta_{600} - \theta_0}{1022^n}\right) = 0{,}511\left(\frac{\theta_{300} - \theta_0}{511^n}\right)\ [Pa \cdot s^n] \qquad (3.30)$$

Figure 3.8 illustrates the comparisons between measured viscometer data and the Herschel Bulkley model. As shown, the model nearly captures the measured fluids with insignificant deviation.

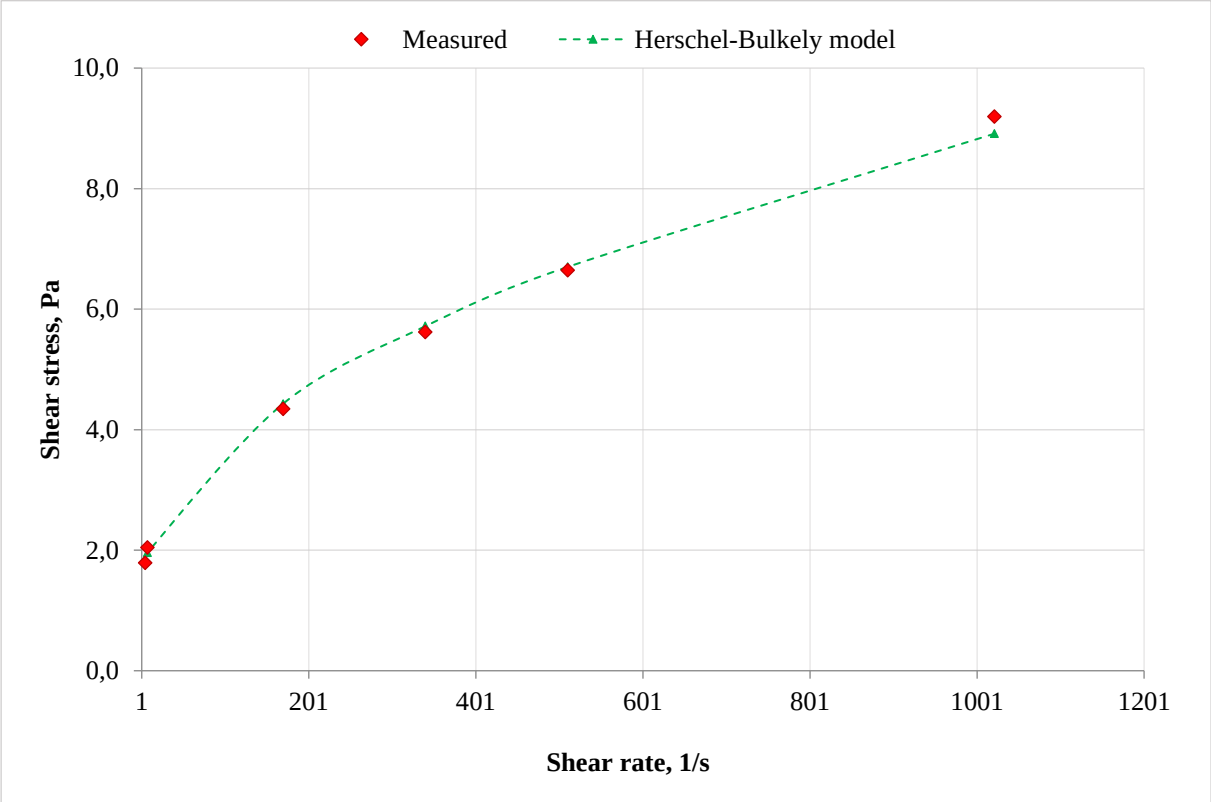

Figure 3.8 - Comparison of viscometer data and Herschel Bulkley Model [F04]

In the experimental part of this thesis, the abbreviation LSYS (Lower Shear Yield Stress) is used instead of θ_3.

3.9 VICOELASTICITY

It is reported in literature that drilling fluid behaves both elastic and viscous and this property is called viscoelasticity [T25] [T26]. The property of viscoelasticity is measured using a rheometer. The viscoelastic property is important for the evaluation of the internal gel structure of the drilling fluid. This is measured by analyzing the response of drilling fluid for an applied dynamic loading. Figure 3.9 shows the measuring principle. A fluid specimen is placed between parallel plates and an oscillatory dynamic load is applied, which introduce shear stress in the sample.

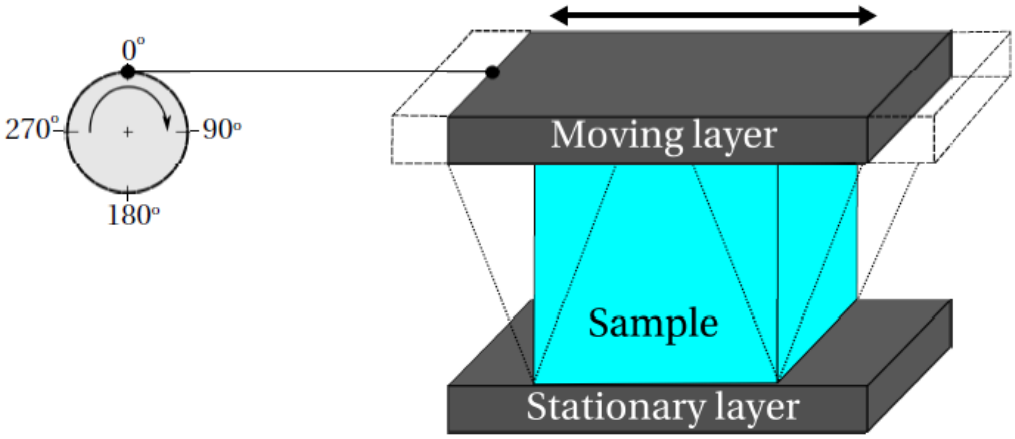

Figure 3.9 - Two-Plates-Model for the Oscillatory test [T26]

Figure 3.10 illustrates the applied dynamic shear stress (τ) and the resulting deformation rate, strain (γ). The applied load stress (τ) and strain (γ) curves are plotted against time. The phase shift angle is the time lag between the stress and strain sine curves and are also called loss angle (δ) [T25].

The time dependent dynamic shear stress and strain are given as [T26]:

$$\gamma(t) = \gamma_o \sin(\omega t) \tag{3.31}$$

$$\tau(t) = \tau_o \sin(\omega t + \delta) \tag{3.32}$$

$$\tau(t) = \tau_o[\sin(\omega t)\cos\delta + \cos(\omega t)\sin(\delta)] \tag{3.33}$$

$$\tau(t) = \gamma_o\left[\left(\frac{\tau_o}{\gamma_o}\cos\delta\right)\sin(\omega t) + \left(\frac{\tau_o}{\gamma_o}\sin\delta\right)\cos(\omega t)\right] \tag{3.34}$$

$$\tau(t) = [G'\sin(\omega t) + G''\cos(\omega t)] \tag{3.35}$$

where - G' is the storage modulus, which is a measurement of the energy stored in the fluid and describes the elastic behavior of the specimen.
- G'' is the loss modulus, which is a measurement of the deformation energy and quantifies the viscous behavior [T25]:

$$G' = \frac{\tau_o}{\gamma_o}\cos\delta \tag{3.36}$$

$$G'' = \frac{\tau_o}{\gamma_o}\sin\delta. \tag{3.37}$$

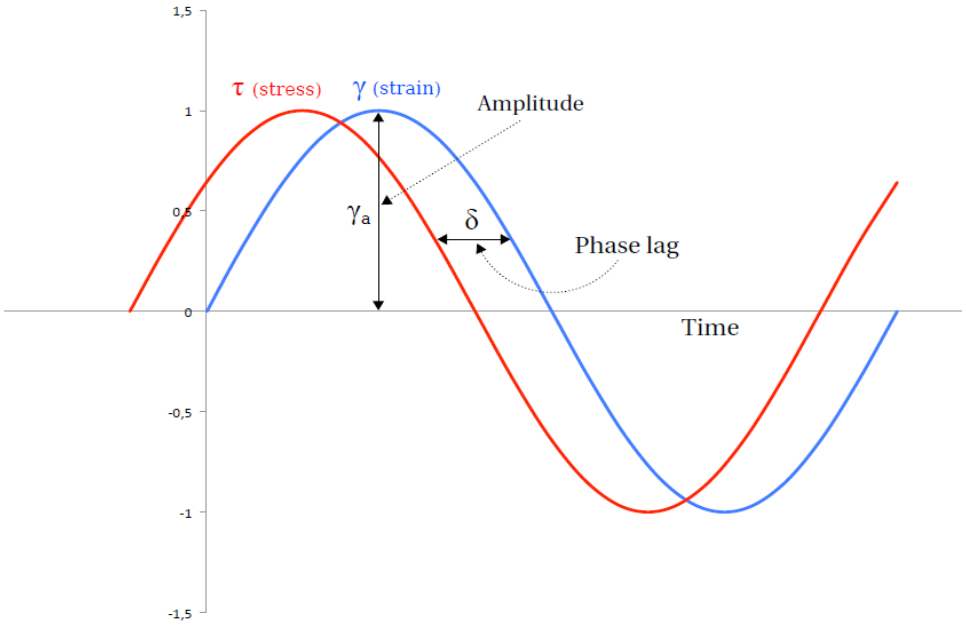

Figure 3.10 - Illustration of stress and strain versus time [T25]

The ratio of G'' (viscous component) and G' (elastic component) is known as the *loss factor* or *damping factor* $(\tan\delta)$ and is defined as:

$$\tan\delta = \left(\frac{G''}{G'}\right) \tag{3.38}$$

The loss angle (δ) is given as:

$$\delta = \tan^{-1}\left(\frac{G''}{G'}\right) \tag{3.39}$$

Based on the value of the storage/loss values and the damping factor/loss angle, one can describe a fluids viscoelasticity. Table 3.1 shows the classifications. When the storage modulus and loss modulus are equal, the fluid behaves equally viscous and elastic. This is a transition point from elastic to viscos and it is called flow point. If the loss modulus is higher than the storage modulus, the system is viscos dominated and when the opposite occurs the system is elastic dominated [T25].

Table 3.1 - Classification of viscoelasticity of fluid [T25]

Ideal viscous behavior	**Behavior of a viscoelastic liquid**	**50/50 ratio: Equal portion of viscous and elastic behavior**	**Behavior of viscoelastic gel or solid**	**Ideal elastic behavior**
$\boldsymbol{\delta = 90°}$	$\boldsymbol{90° > \delta > 45°}$	$\boldsymbol{\delta = 45°}$	$\boldsymbol{45° > \delta > 0°}$	$\boldsymbol{\delta = 0°}$
$\boldsymbol{\tan\delta \to \infty}$	$\boldsymbol{\tan\delta > 1}$	$\boldsymbol{\tan\delta = 1}$	$\boldsymbol{\tan\delta < 1}$	$\boldsymbol{\tan\delta \to 0}$
$\boldsymbol{G' \to 0}$	$\boldsymbol{G'' > G'}$	$\boldsymbol{G' = G''}$	$\boldsymbol{G' > G''}$	$\boldsymbol{G'' \to 0}$

In this thesis, among many others, an oscillatory amplitude sweep test was conducted. During the amplitude sweep test, the damping is amplitude of oscillation while keeping the frequency and the temperature constant.

Figure 3.11 illustrates the amplitude sweep measurement responses, which shows linear viscoelastic range (elastic dominated, G' > G'') and the viscous dominated region (G' < G'').

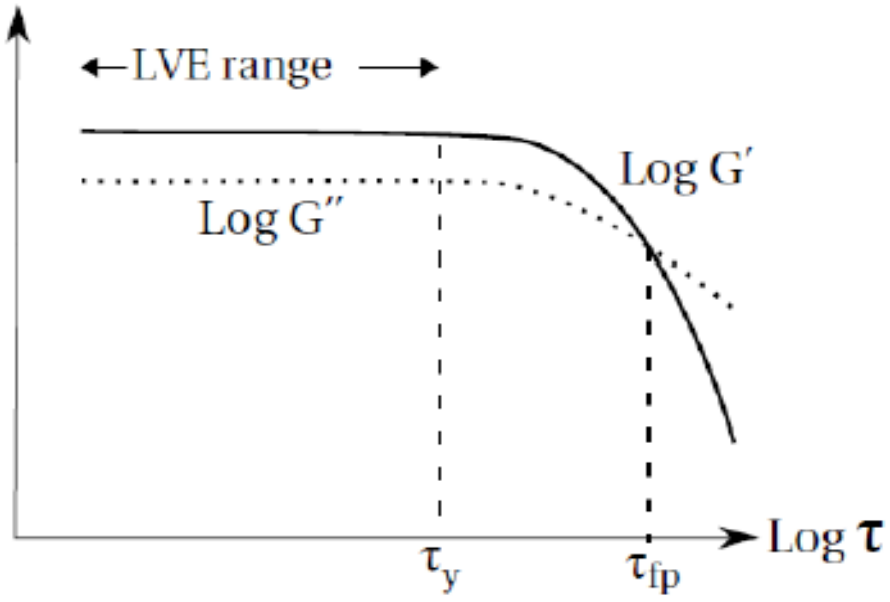

Figure 3.11 - Illustration of amplitude sweep responses [T25]

3.10 RAYLEIGH-TAYLOR INSTABILITY

The Rayleigh-Taylor instability (RTI) is a dynamic process which occurs at the interface when a lighter fluid pushes a heavy fluid. Figure 3.12 shows the forces acting on the fluid interface. Here g is gravity, p is pressure, ρ is density and ω is the vorticity. The velocity field created by the vortex is represented by the thick circular arrows in the figure. This configuration is unstable when $\rho_2 > \rho_1$ and an acceleration is applied in the direction toward the denser fluid. When there is a mismatch between the density gradient and pressure [T10],

$$\nabla\rho \cdot \nabla p < 0, \tag{3.40}$$

RTI is induced.

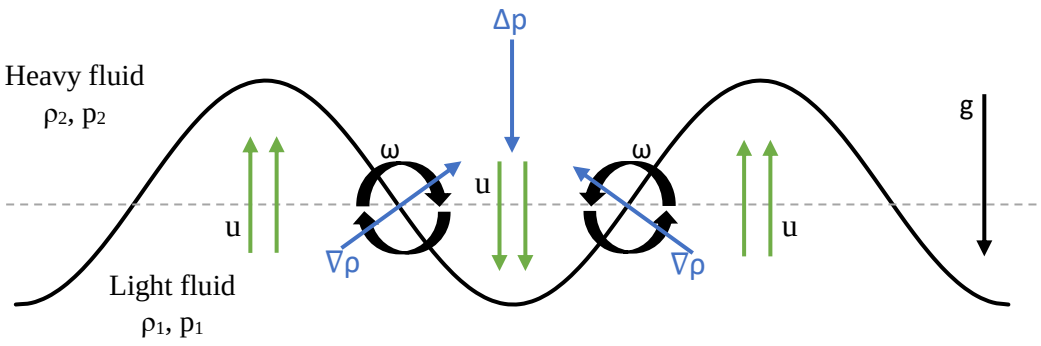

Figure 3.12 - Forces acting on the fluid interface [F04]

RTI can thus be seen as the result for baroclinic torque created by such misalignment. This is given by the inviscid 2D vorticity equation by Cohen and Kundu (2004),

$$\frac{D\omega}{Dt} = \frac{1}{\rho^2}\nabla\rho \times \nabla p. \tag{3.41}$$

The acceleration result in the dominant pressure. As a result of a particular harmonic component of the initial perturbation, vorticity is created by torque on the interface. This will tend to lead to additional misalignment of the gradient vectors, and from this create further misalignment and additional vorticity. The vorticity is generated by the baroclinic term on the right-hand side of equation (3.41). The growth of the amplitude of a small perturbation on a discontinuous interface is found by using a linear stability analysis, resulting in the equation

$$\frac{d^2a}{dt^2} = gkAa, \tag{3.42}$$

where a is the amplitude,

k is the wave number, $k = 2\pi/\lambda$, where λ is the wave length, and

A is the Atwood number, $A = (\rho_1 - \rho_2)/(\rho_1 + \rho_2)$, where ρ_1 and ρ_2 are the densities of the heavy fluid and light fluid respectively [T10].

Figure 3.13 illustrate the numerical simulations of Rayleigh-Taylor turbulence in presence of rotation in the vertical direction [T18]. As shown, the one on the left is not rotating and the two on the right side are rotating. After 30 second simulation, the resulting fluid mix at the interface is shown in figure 3.14. The stability in high RPM shows better than at the static condition.

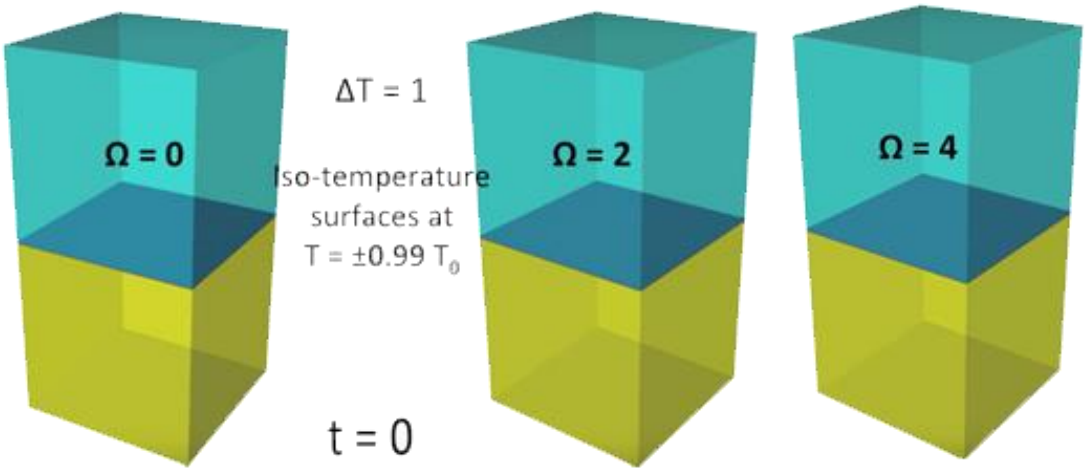

Figure 3.13 – Illustration of numerical simulation of RT turbulence at time = 0 [T18]

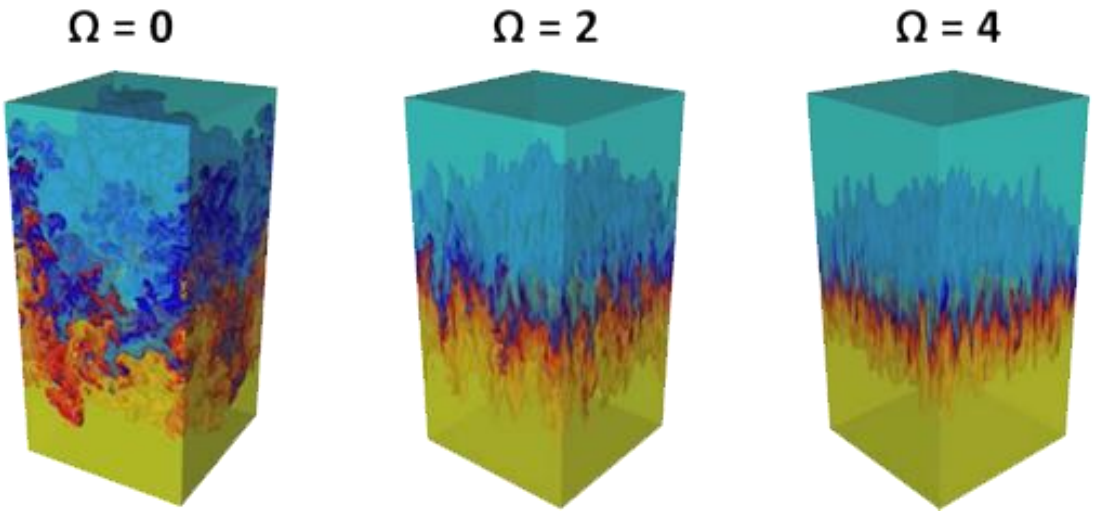

Figure 3.14 – Illustration of numerical simulations of RT turbulence at time = 30 sec [T18]

3.11 KELVIN–HELMHOLTZ INSTABILITY

When the Rayleigh-Taylor instability occurs, the fluids on each side of the interface will have different velocities. If the velocity difference is large enough and a vertical shear occurs, the interface will be unstable. This is called the Kelvin-Helmholtz (KH) instability and is shown in figure 3.15. The theory can be used to predict at what time a liquid becomes unstable and at what time a flow becomes turbulent in a liquid depending on how high density and speed the fluid flow has. The KH instability occurs throughout the whole flow except when the velocity is equal [T12].

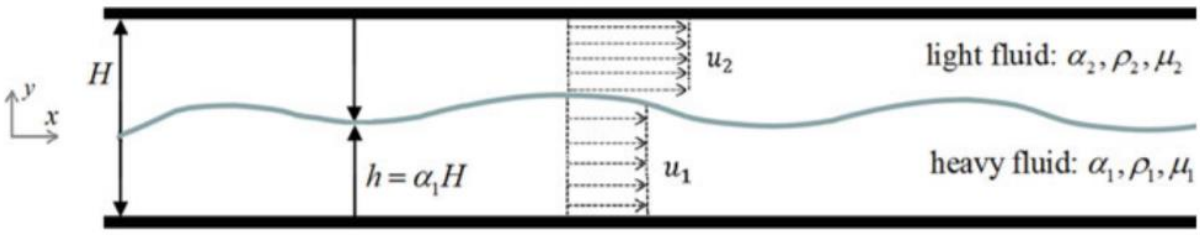

Figure 3.15 - Kelvin-Helmholtz instability [T12]

Figure 3.16 illustrates the numerical simulations of temporal Kelvin-Helmholtz instability at the light-heavy interface. The simulation was conducted using Flow square 4.0. [T29]. The flow goes through a channel of a rectangular cross section horizontally. As displayed in [B], at the interface, the lighter layer is mixing with the heavy.

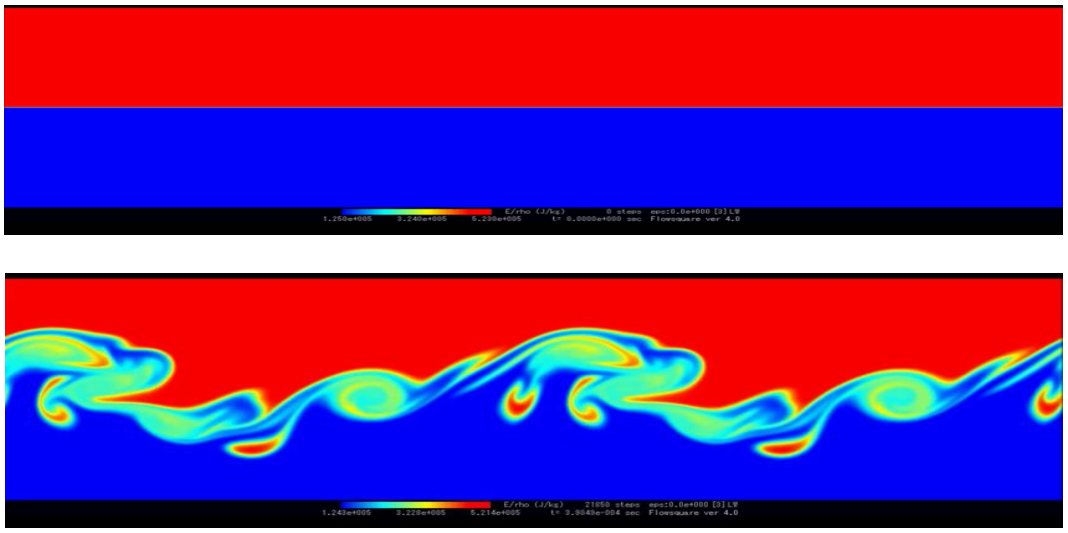

Figure 3.16 - Illustration of temporal Kelvin-Helmholtz instability at the light-heavy interface

4 EXPERIMENTAL STUDY

[All experiments were conducted following the HSE standards of UIS and the Institute of petroleum]

A series of experiments were conducted to learn more about the HOL mixing zone in the vertical section of a well. The main focus was to investigate the mixing zone that occurred during rotating of a string which was supposed to simulate a drill string. Every experiment was documented with pictures taken at various times during the experiments. These pictures were used to analyze the mixing zone and how it developed over time. The properties of the fluids used were also documented and the raw fluid data is available from Appendix C.

There were used three different setups as shown in section 4.2.

4.1 DRILLING FLUID ADDITIVES AND FORMULATION

4.1.1 DESCRIPTION OF DRILLING FLUID ADDITIVES

In this thesis work, bentonite-based laboratory drilling fluids were formulated to prepare heavy and light drilling fluids. The following presents the description of the drilling fluid additives.

Bentonite

Bentonite, better known as clay, is a the commonly used additive in water-based drilling fluids. Its function is mainly to provide viscosity and bentonite is used in this thesis work. Bentonite was originally found in Wyoming, US. Bentonite clay is also known as montmorillonite clay. Montmorillonite provides ability of swelling and has thixotropic properties. The chemical composition of bentonite is shown in Table 4.1. As shown, the bentonite composes of about 10 – 30 % non-clay minerals [T13].

Table 4.1 – Composition of bentonite [T13]

Component	**Percentage of chemical composition**
Silica, SiO_2	64.32
Alumina, Al2O3	20.74
Cumulative water	5.14
Ferric oxide, Fe2O3	3.03
Soda, Na2O	2.59
Magnesia, MgO	2.30
Lime, CaO	0.50
Ferrous Oxide, FeO	0.46
Potash, K2O	0.39
Sulfuric Anhydride	0.35
Titanium Oxide, TiO2	0.14
Phosphoric Anhydride	0.01
Other minor constituents	0.01

As shown in figure 4.1, montmorillonite is composed of two tetrahedral alumina layers with one octahedral silica layer in between. When in contact with water, the montmorillonite will adsorb the water molecule and swelling will occur [T13].

During fluid preparation, the chemistry of polymer, color dye additives and bentonite provided sufficient viscosities for heavy and light drilling fluid.

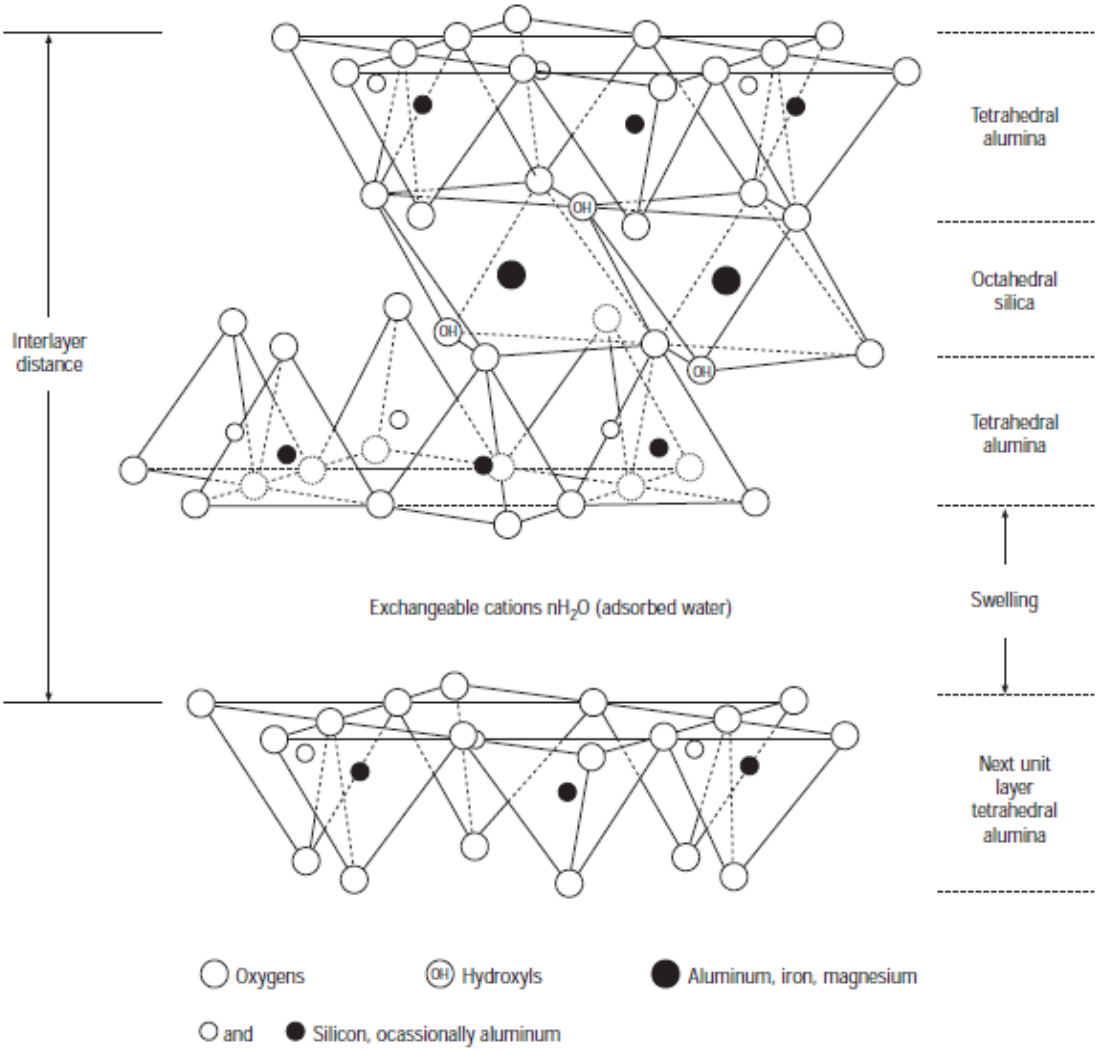

Figure 4.1 - Sketch of the structure of montmorillonite [T13]

Xanthan Gum

Xanthan gum is a long chain anionic biopolymer which is soluble in water. Xanthan gum is used to control the viscosity of the drilling fluid. Figure 4.2 shows the structure of xanthan gum, which comprises of a three-ring side chain and a two-ring backbone. Xanthan gum gives good thixotropic properties. During this thesis work, xanthan gum is used to provide desired drilling fluid properties such as viscosity and yield stress [T19].

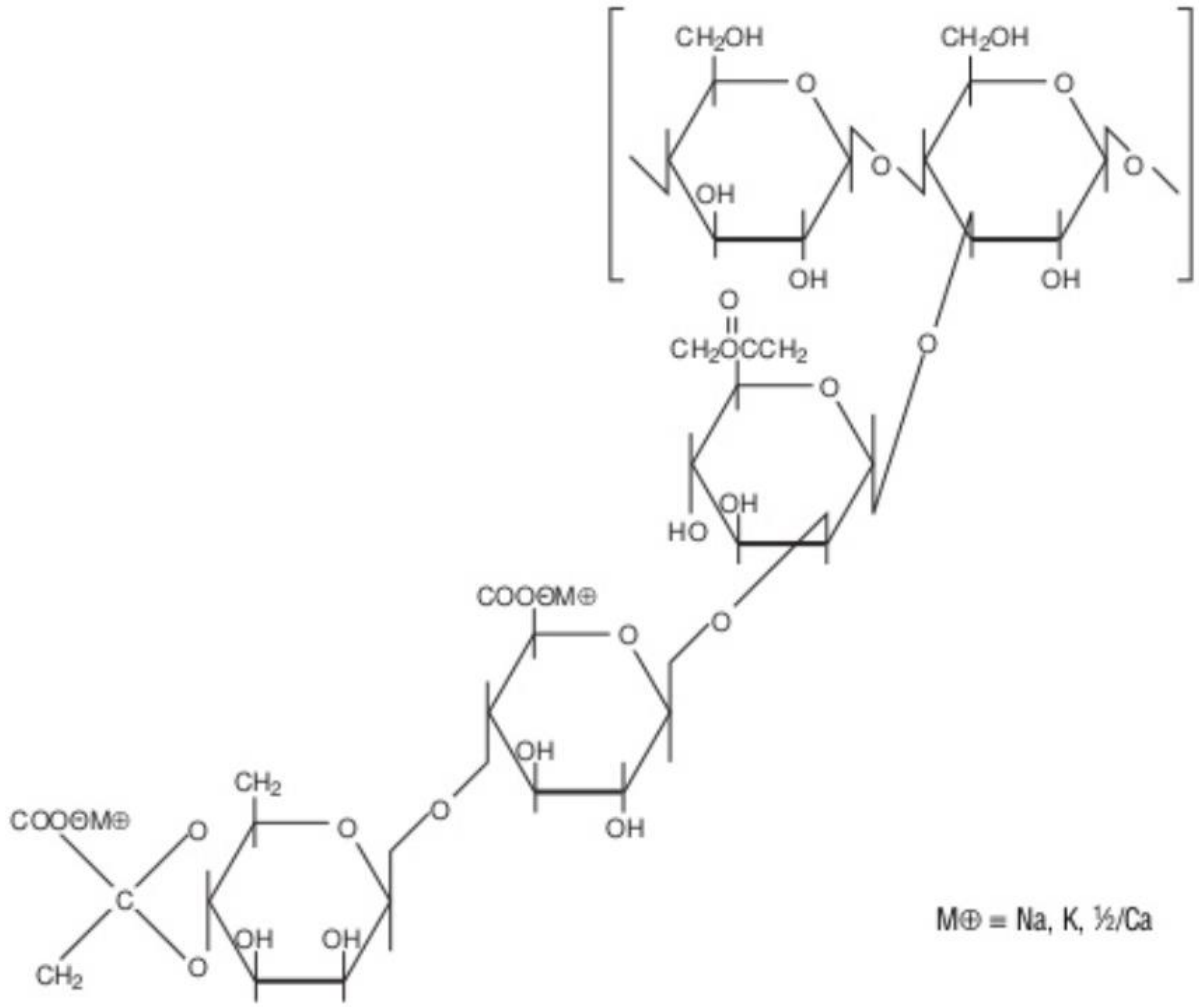

Figure 4.2 - Structure of Xanthan Gum [T19]

Barite

Barite is used commonly used in drilling fluids as a weight control additive. Chemically, barite minerals consist of barium sulfate ($BaSO_4$). The density of barite is 4.2 sg. [T09]

Lignosulfonate

Depending on the concentration of the bentonite and water, the solution may create an aggregated system. If the particle aggregation is flocculated, where the particles are clusted together, the solution will have a high yield stress. In order to disperse and deflocculated the system, lignosulfonate is a commonly used additive in water-based drilling fluid. The additive controls the yield stress of the drilling fluid by reducing the attractive forces between the clay particles in the fluid and rather creates a repulsive force as lignosulfonate attaches to the clay particles [T19].

Color Pigment

In order to have a clear HOL interface the drilling fluids were stained with two different colors using color powder pigments. The light fluid was stained using green chrome oxide and the heavy fluid was stained using red iron oxide. Both pigments are from Kremer Pigmente GmbH & Co. KG and are in soluble in water. The pigments are bought at KEM (Kunstnernes Eget Materialutsalg SA) and are usually used as coloring agent (pigment and dyes) [T22] [T23].

Mixed with drilling fluids, these pigments showed almost no sign of air bubbles. The pigments are shown in figure 4.3.

Figure 4.3 - Red Iron Oxide and Green Chrome Oxide Pigment Powder [F05]

Particle associations

The behavior of the clay particles in a solution is important because it affects significant properties like viscosity and yield point. For better understanding of the clay particle behavior, the four conditions clay particles can form in water are [T09]:

- Flocculated System: the solution will be flocculated when there are net attractive forces between the particles. In this case, as shown in figure 4.4, they will attach end-to-end or surface-to-surface. The flocculated system results in higher viscosity, filtrate loss and yield point [T09].
- Deflocculated system: the solution will only have repulsive forces between the particles. This is the result when the particles have the same electric charge. In order to obtain this system, lignosulfonate was used to deflocculates the system and hence reduce the yield strength of the solution [T09].
- Aggregated System: The solution is described as aggregated when many single particles bond together as shown in figure 4.4 [T09],
- Dispersed System: both the flocculated and deflocculated system will be dispersed in a solution by splitting the clay particles into single plates [T09].

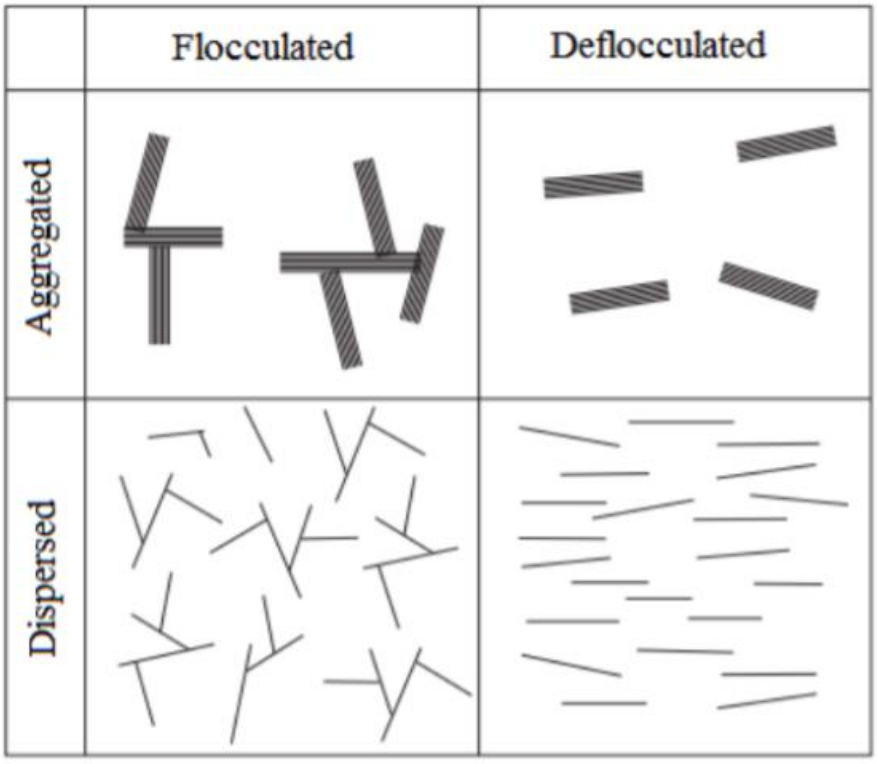

Figure 4.4 - Arrangement of clay particles in drilling fluid [T09]

4.1.2 DRILLING FLUID PREPARATION

Two drilling fluids were made for each experiment; one heavy fluid and one light fluid. A standard fluid was made with water, the polymer Xanthan gum, bentonite and color with a recipe example shown in table 4.2.

The drilling fluids were properly mixed at a very high speed.

Table 4.2 – Example of a standard drilling fluid recipe

Water [g]	500
Xanthan Gum [g]	0,5
Bentonite [g]	25
Color [g]	5

4.1.3 DRILLING FLUID DENSITY MODIFICATION

Then, the fluid rheology and density were measured. If higher density was desired barite was added. The amount of barite added was calculated from equation (4.1)

$$m_{barite} = \frac{\rho_{barite}}{\rho_1} \frac{\rho_2 - \rho_1}{\rho_{barite} - \rho_2} \cdot m_{mud}, \tag{4.1}$$

where m_{barite} is the weight of barite to be added [g],

ρ_{barite} is the density of barite = 4,2 · 8,33 [ppg],

ρ_1 is the initial density of the mud [ppg],

ρ_2 is the desired density of the mud [ppg] and

m_{mud} is the initial weight of the mud [g].

If a lower density was desired, the fluid was thinned out with water. The amount of water added was calculated with equation (4.2).

$$m_{water} = \frac{\rho_{water}}{\rho_1} \frac{\rho_2 - \rho_1}{\rho_2 - \rho_{water}} \cdot m_{mud}, \tag{4.2}$$

where m_{water} is the weight of water to be added [g] and

ρ_{water} is the density of water = 8,33 [ppg].

For some of the fluids it was desired to lower the yield point without lowering the density. To solve this situation, lignosulfonate was added. Mainly, small amounts of lignosulfonate were added until the desired yield point was reached. When adding lignosulfonate, the pH value had to be modified with NaOH because the lignosulfonate does not work in sour liquids.

To be able to visually see the mixing zones, both fluids had to be colored with different colors. In the preliminary experiments, food coloring was used. However, this did not give the color contrast desired and color pigments replaced the food coloring.

For the light fluid, green chrome oxide was used to set color on the fluid and for the heavy fluid, red iron oxide was used, as described in section 4.1.1.

4.2 EXPERIMENTAL SETUPS

Equipment used for these experimental setups are listed in Appendix B.

Preliminary experiments

For preliminary experiments, first, a horizontal setup was built as illustrated in figure 4.5. This was done to get familiar with the experiments and to develop a procedure for later experiments. The results from these experiments are not analyzed in this thesis.

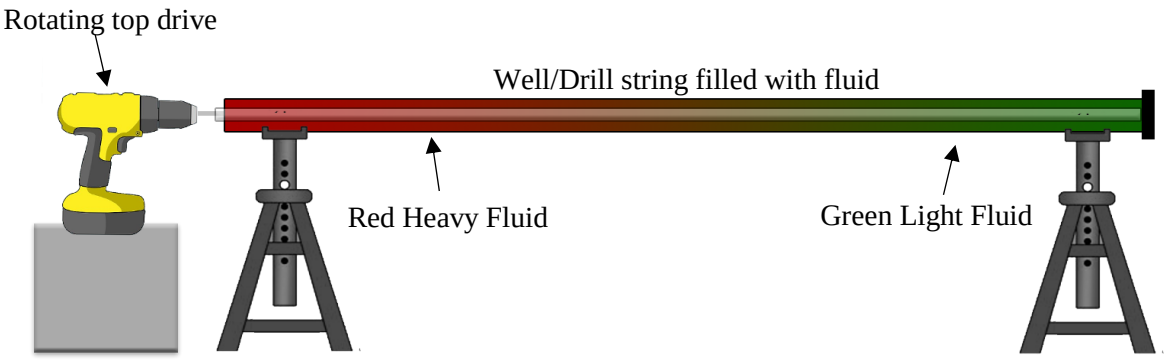

Figure 4.5 - Illustration of experimental setup for preliminary experiments [F04]

Then, vertical experiments were done with a simple setup as shown in figure 4.6.

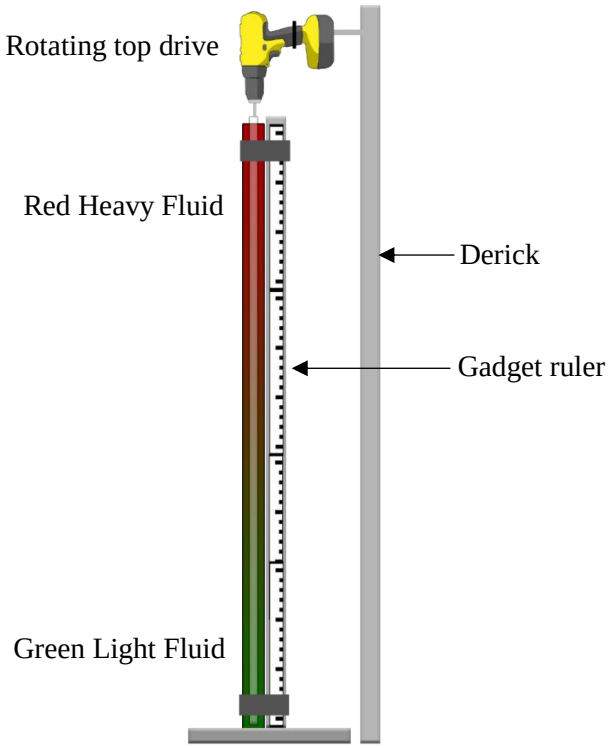

Figure 4.6 - Illustration of vertical preliminary setup [F04]

Main experiments

The experimental setups shown in figure 4.5 and figure 4.6 are exposed to laboratory light from the environment that affects the resolution of the pictures taken during the experiments. To be able to obtain the same lightning conditions for all the pictures, a new setup was built. This design will help identify a clear fluid mix and unmixed zones with better resolution. The design use light-blocking roller blinds to avoid the effect of the surrounding laboratory light. At the back side of the experimental rig, a stripe of LED light was placed to focus on the mixing section. Figure 4.7 shows the main experimental setup used in this thesis work both with and without the light-blocking roller blinds. The pictures taken from this setup is reliable for MatLab picture processing described in section 4.3.3.

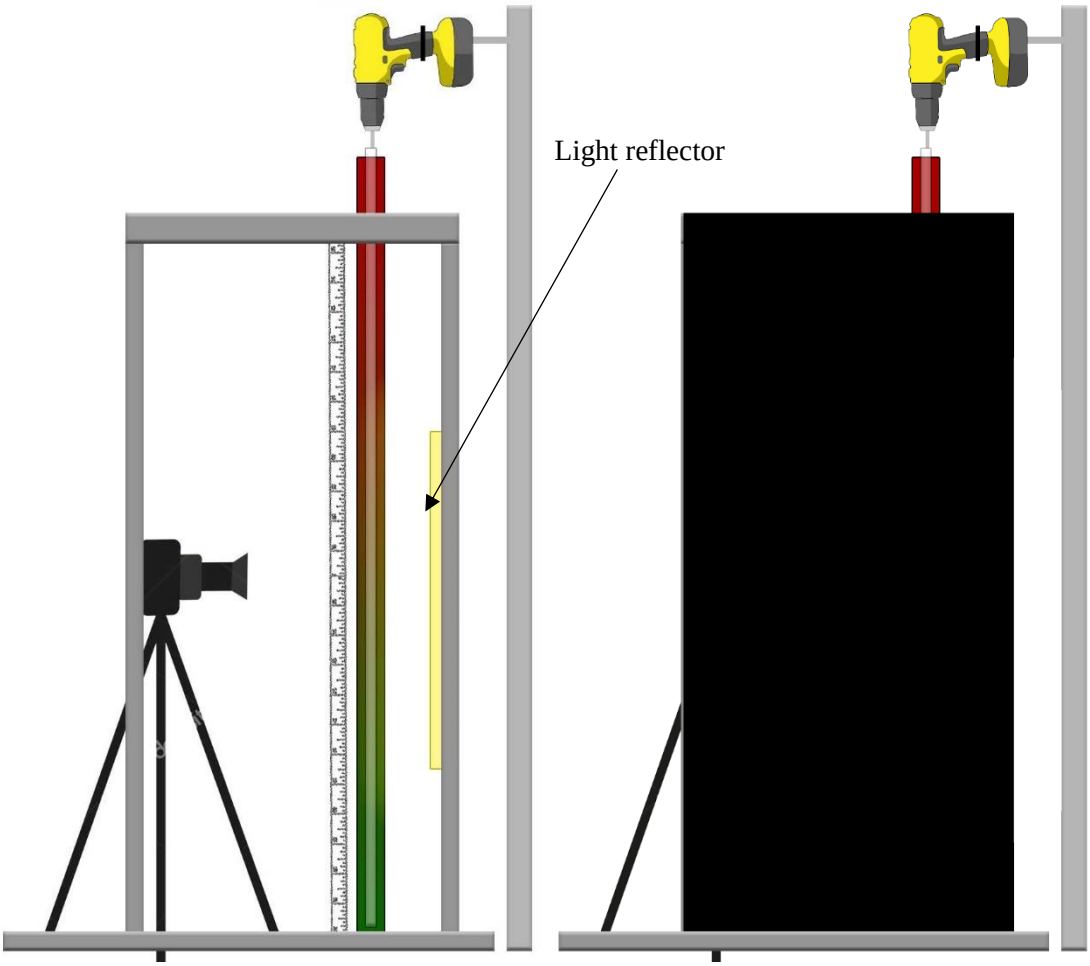

Figure 4.7 - Illustration of main experimental setup [F04]

4.3 EXPERIMENTAL PROCEDURES

Procedures for measuring rheology, gel strength, density and RPM are described closely in Appendix A.

This section deals with drilling fluid preparation, procedures for conducting the experiments and the procedures for determining the length of the mixing zone.

4.3.1 WORK PROCEDURE

The light drilling fluid was first poured into the plastic pipe using a small-diameter hose and a funnel to ensure light fluid only in the lower part of the pipe as shown in figure 4.8.

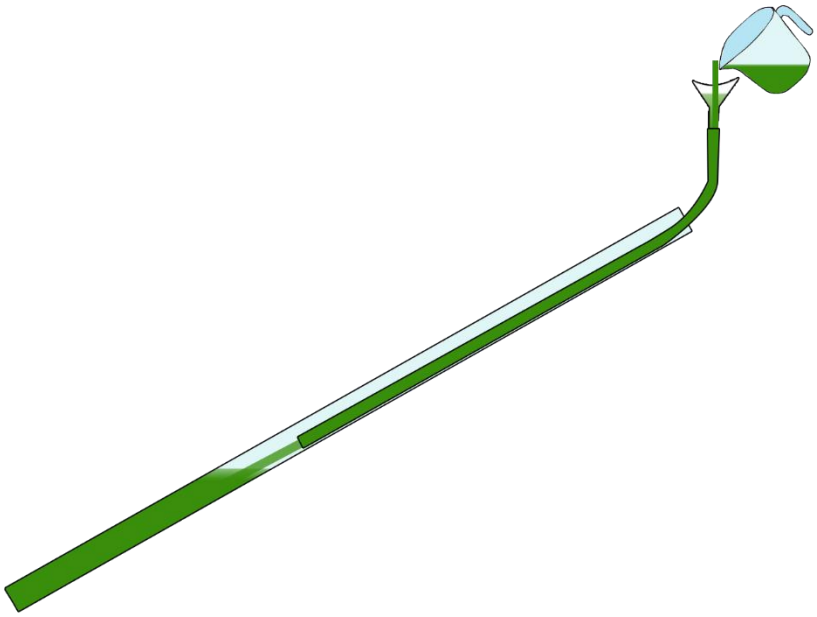

Figure 4.8 - Procedure of pouring light fluid into pipe [F04]

Then, the string/pole used as a rotating drill string was added and the pipe with the light fluid and drill string was set in place before the heavy fluid was poured into the pipe on top of the light fluid. The string was coupled with an electric drill machine and rotation was started.

The drilling machine is normally operating with a very high RPM, which was not desired for these experiments. Tying to obtain a constant low RPM showed to be very challenging and this resulted in a highly variable RPM during the experiments. The value reported for all the experiments are therefore 50 – 250 RPM.

The camera function time-lapse was used to capture the mixing zone development once every minute throughout the whole experiment.

4.3.2 VISUAL ANALYSIS PROCEDURE

All mixing zone analyzes is done by taking pictures during the mixing process and analyzing the pictures afterwards. An example of an image sequence of the mixing development is shown in figure 4.9 where the heavy fluid is red, and the light fluid is green.

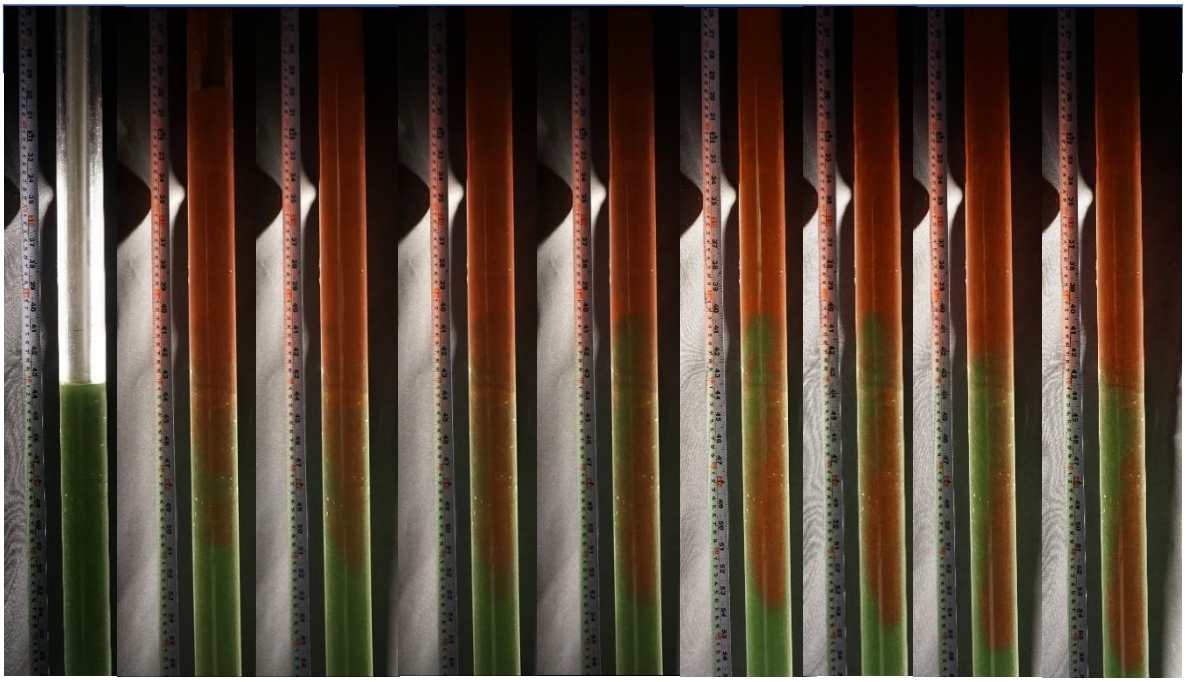

Figure 4.9 - Example of an image sequence capturing the mixing zone each minute [F05]

The mixing zone is simply decided by looking at the colors in the picture and the measuring tape next to the pipe. It is assumed that if an amount of heavy fluid falls down, the same amount of light fluid has to go up in the pipe.

4.3.3 MATLAB ANALYSIS PROCEDURE

In addition to visual inspection, a picture processing method has been employed in this thesis work to determine a precise mixing zone. For this a MatLab code has been written.

Matlab is a mathematical program used for numerical calculations, simulations and visualization. When analyzing the images in MatLab, a command called `improfile` has been used. `improfile` retrieves the intensity values of pixels along a line in an RGB image and displays a plot of the intensity values [T14].

An example of a code used for these analyses are shown below. The code was customized to each individual experiment. Figure 4.10 shows the plots created by the `improfile` command.

```
clc
clf
clear all
```

```
xi = [1 6000];
yi = [2187 2083];
n=200;

subplot(5,1,1)
pic = imread('DSC03567.JPG');
imshow(pic);
improfile(pic,xi,yi,n,'nearest'),grid on,grid minor;
title('Start, test 0424 - 2');
axis([0 6000 0 100]);
xlabel('');

subplot(5,1,2)
pic1 = imread('DSC03576.JPG');
imshow(pic1);
improfile(pic1,xi,yi,n),grid on,grid minor;
title('10 min');
axis([0 6000 0 100]);
xlabel('');

ki = [2152 2049];

subplot(5,1,3)
pic2 = imread('DSC03586.JPG');
imshow(pic2);
improfile(pic2,xi,ki,n),grid on,grid minor;
title('20 min');
axis([0 6000 0 100]);
xlabel('');


subplot(5,1,4)
```

```
pic3 = imread('DSC03596.JPG');
imshow(pic3);
improfile(pic3,xi,ki,n),grid on,grid minor;
title('30 min');
axis([0 6000 0 100]);
xlabel('');

subplot(5,1,5)
pic4 = imread('DSC03606.JPG');
imshow(pic4);
improfile(pic4,xi,ki,n),grid on,grid minor;
title('40 min');
axis([0 6000 0 100]);
xlabel('');
```

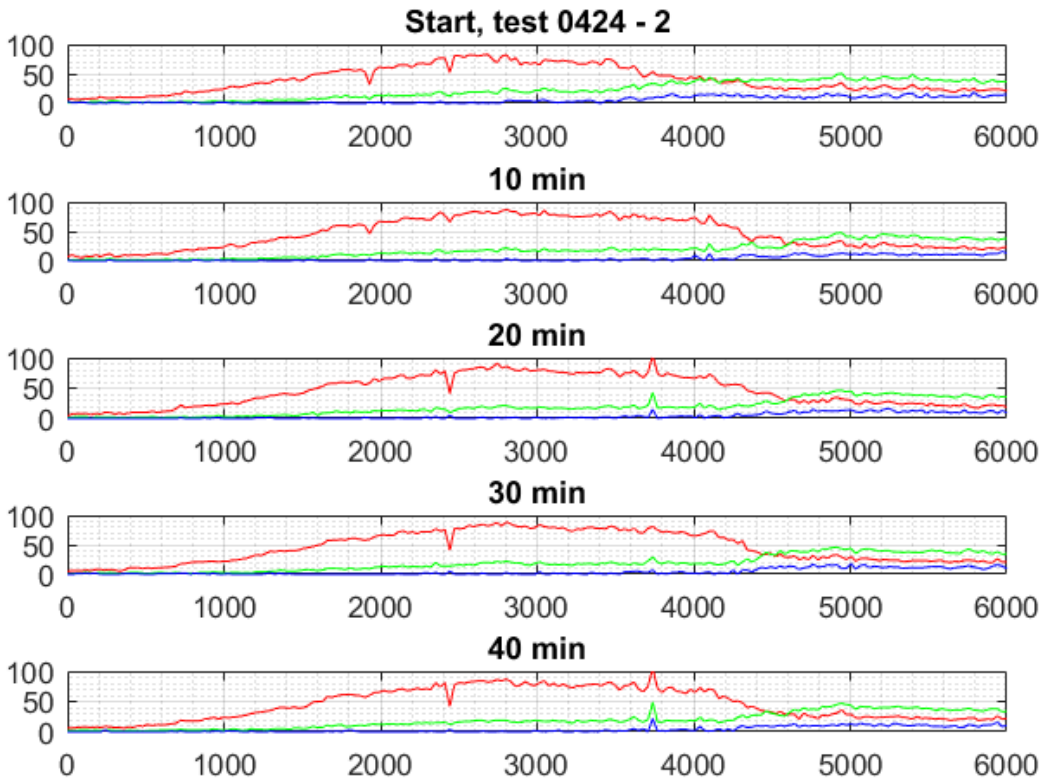

Figure 4.10 - Example of plots created by the improfile command

Mixing zone determination

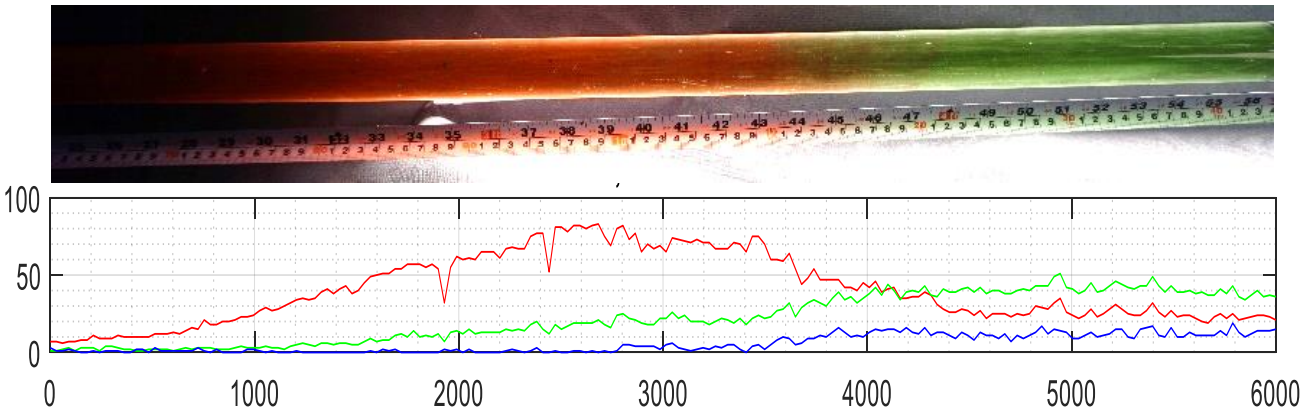

Figure 4.11 - Image captured during mixing and the corresponding improfile plot

Figure 4.11 is an example of an image taken during mixing and the corresponding improfile plot. The values on the x-axis represents the numbers of pixels on a horizontal line in the pipe in the picture. The height Δh of the section shown in the picture is:

$$\Delta h = h_2[cm] - h_1[cm], \tag{4.3}$$

where h_1 is the lowest value read from the measuring tape in the picture and h_2 is the highest value read from the measuring tape in the picture. The height of the mixing zone is determined by comparing the graph from the start of the mixing process to the graph you want to determine the mixing zone from.

$$Mixing\ zone = \frac{\Delta h}{6000} \cdot (h_{end} - h_{start})\ [cm], \tag{4.4}$$

where h_{end} and h_{start} is where the mixing zone ends and start respectively, using the values from the x-axis.

Also, here, it is assumed that if an amount of heavy fluid falls down, the same amount of light fluid has to go up in the pipe.

4.4 COLOR ANALYSIS

In figure 4.12, several mixes with different amount of heavy and light fluid is shown. This is done to see how the color of the mixture changes according to the relationship between de different fluids.

Figure 4.12 - Colors of different fluid mixtures [F05]

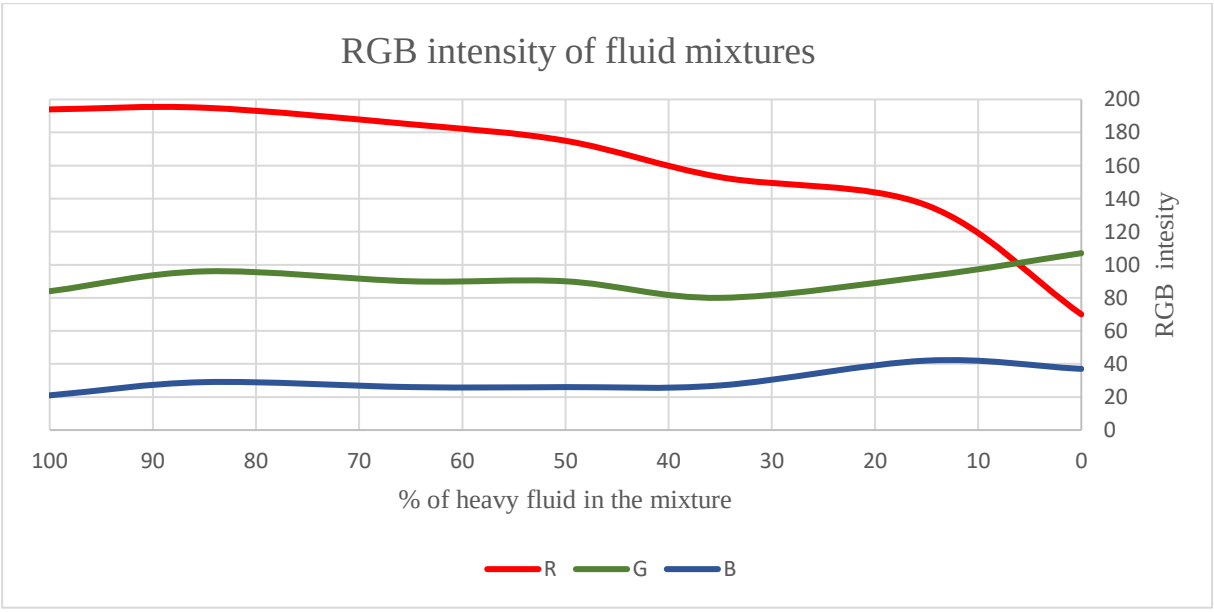

Figure 4.13 - RGB intensity plot of fluid mixtures

Figure 4.13 shows the RGB intensities of the fluids in figure 4.12 plotted against the amount of heavy fluid in the mixture. As shown, the red color is the most dominant one, and this has to be taken into account when analyzing plots and pictures from the experiments. Hence, the mixing zone is not necessarily at the cross-section between the red and the green curve.

5 RESULT ANALYSIS

This chapter presents results from experimental work conducted for this thesis and the eventual correlation between the mixing zone length and mixing zone development rate and well sizes, clearance and fluid parameters. A summary of all the results can be found in Appendix D, and a total overview is illustrated in figure 5.1.

The length of the pipes used as wells in these experiments are limited to 200 cm, i.e. when the mixing zone is reported as 200 cm, full mixing of the pipe has occurred and the actual mixing zone is most likely longer than the 200 cm these experiments were limited to.

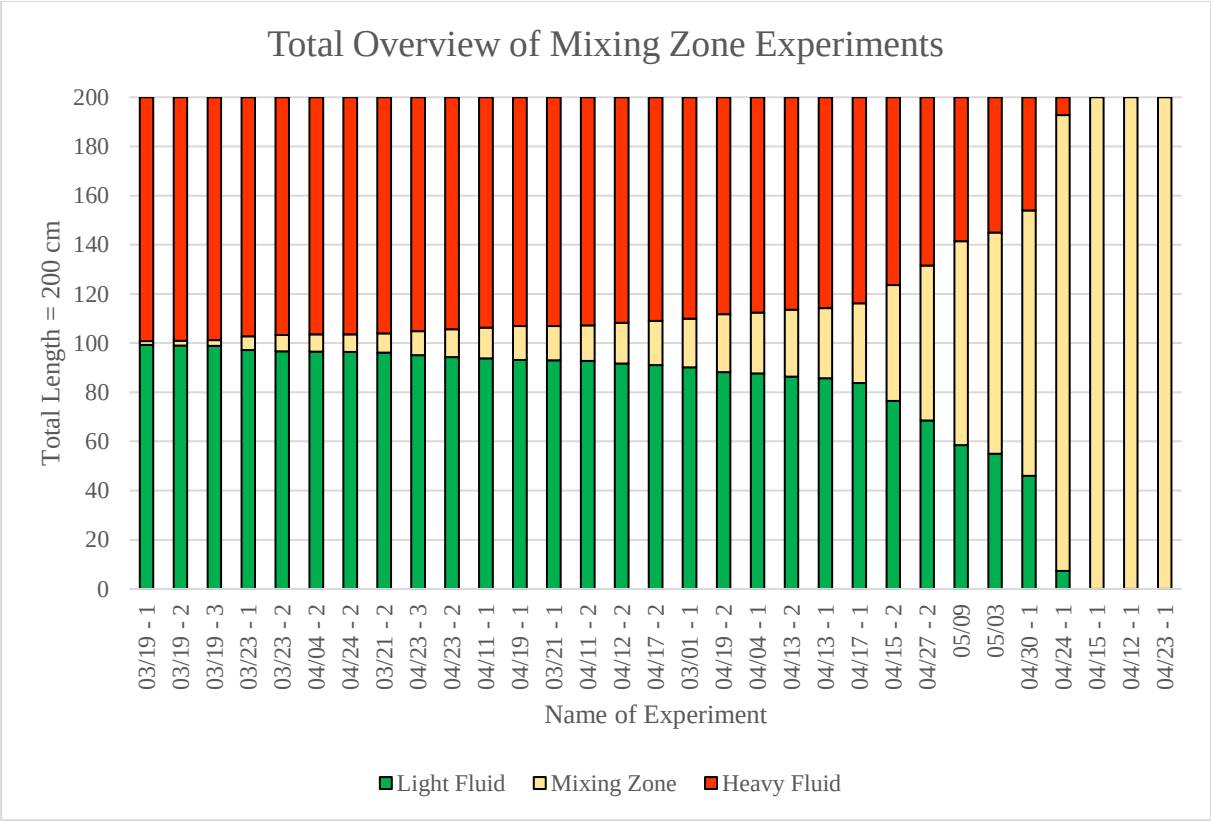

Figure 5.1 - Total overview of all experiments

For the record:

$\Delta\rho = \rho_{heavy\ fluid} - \rho_{light\ fluid}$ [s.g.],

$\Delta PV = PV_{heavy\ fluid} - PV_{light\ fluid}$ [cP],

$\Delta LSYS = LSYS_{heavy\ fluid} - LSYS_{light\ fluid}$ [lbs/100ft^2], and

$Clearance = ID_{well} - OD_{drill\ string}$ [mm].

5.1 EFFECT OF DENSITY

To investigate the effect of density on heavy over light density interface stability, drilling fluids with density difference in the in the range of 0.084 - 0.462 sg were formulated and analyzed. Due to the force of gravity, it is assumed that the difference in density will have a significant role in the mixing zone length. Figure 5.2 displays all experimental mixing zone results plotted against the difference in density, Δρ. As shown, the region below the red dashed line exhibits relatively lower mixing zone. Similarly, the four sets of data bounded in the red circle are relatively in the order of the same density difference with the sets of data bounded in blue rectangle. The main reason for the higher mixing zone was that the yield strength of the light drilling fluid was 1 lbf/100ft^2, which was the same value as the gel strength of the drilling fluid. This was one of the driving mechanisms for the instability of the datasets in the red circle. On the other the yield strength of the dataset in the green circle was in the range of 3.5 - 11 lbf/100ft^2. From this study one can surmise that the gel strength of light drilling fluid is a key for holding the heavier drilling fluid in suspension and is believed to control the mixing zone stability, which eventually will reduce the length.

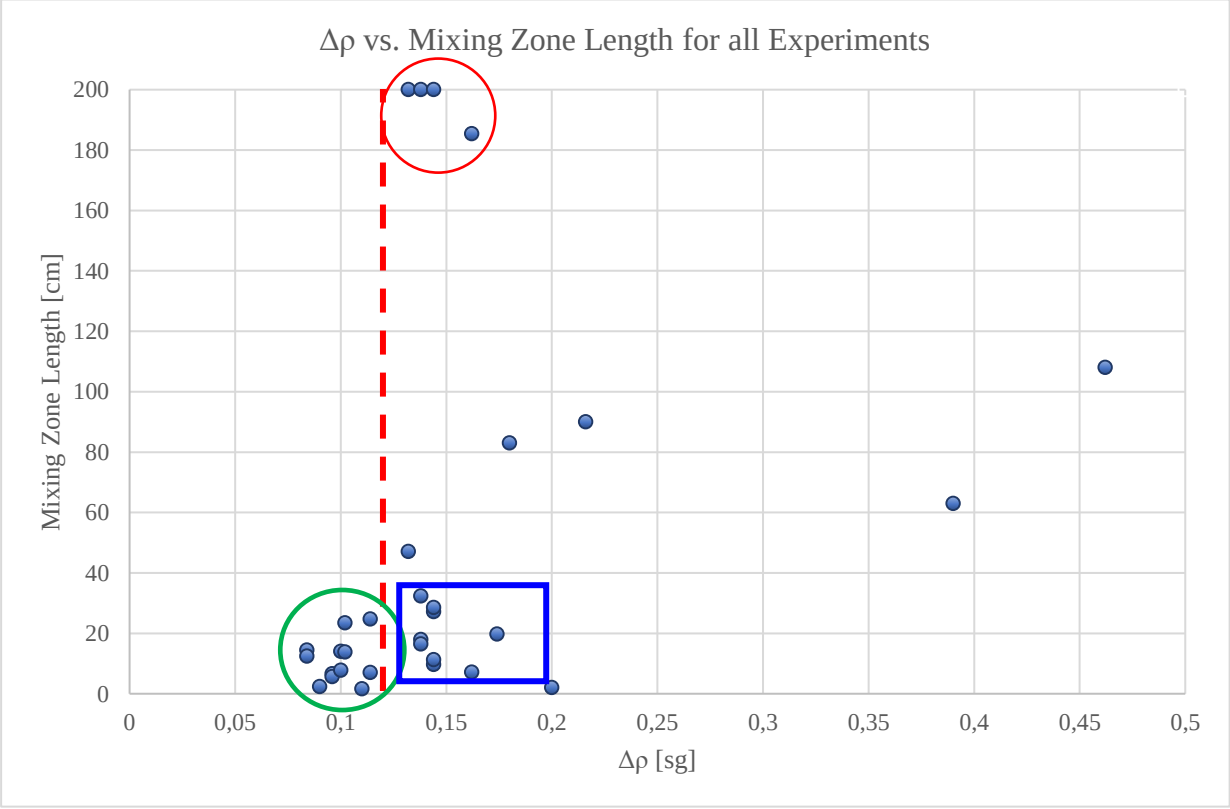

Figure 5.2 - Δρ vs. Mixing Zone length including critical value

From the graphs it is suggested that there exists a critical value for Δρ and that this distinguishes between controlled and uncontrolled mixing zone. The critical value suggested for Δρ is set to 0.120 sg. and is marked with a dashed red line in the graphs above. This applies to all well sizes, clearances and other fluid parameters.

Figure 5.3 shows Δρ versus the mixing zone rate for all experiments.

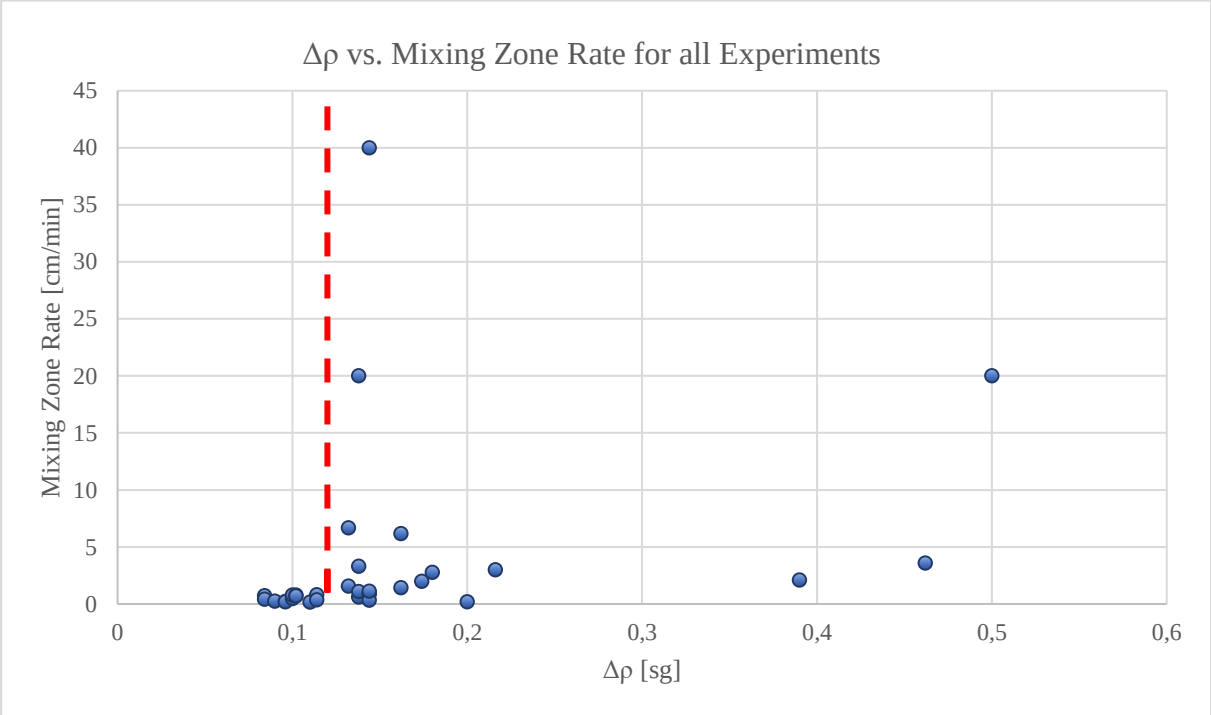

Figure 5.3 - Δρ vs. Mixing Zone Rate including critical value

5.2 EFFECT OF PLASTIC VISCOSITY

To analyze and interpret the effect of plastic viscosity, the difference between heavy and light fluid (ΔPV) was used as an evaluation parameter. Figure 5.4 and figure 5.5 shows ΔPV vs. mixing zone lengths and rates for all experiments. Just like for Δρ, as shown in the figures, a critical ΔPV for all types of wells/clearances considered for the experiments appear to be between 3 and 3.5 cP. The critical value is here sat to 3.25 cP and is marked with a red, dashed line. Similarly, as for Δρ, at the set of data in the ellipse right above the critical point show a higher mixing zone. As explained earlier, the reason was due to the lower yield stress/gel strength of the light drilling fluid.

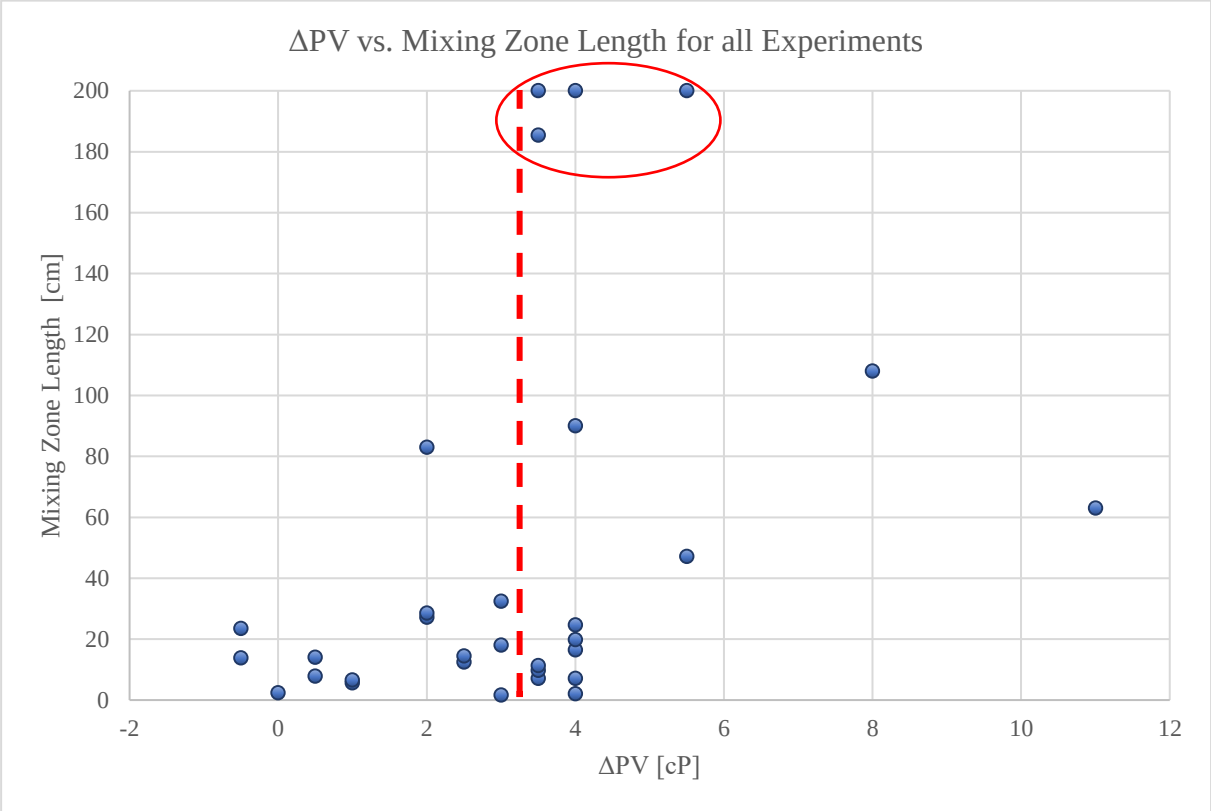

Figure 5.4 - ΔPV vs. Mixing Zone Length including critical value

Figure 5.5 shows ΔPV versus the mixing zone rate for all experiments.

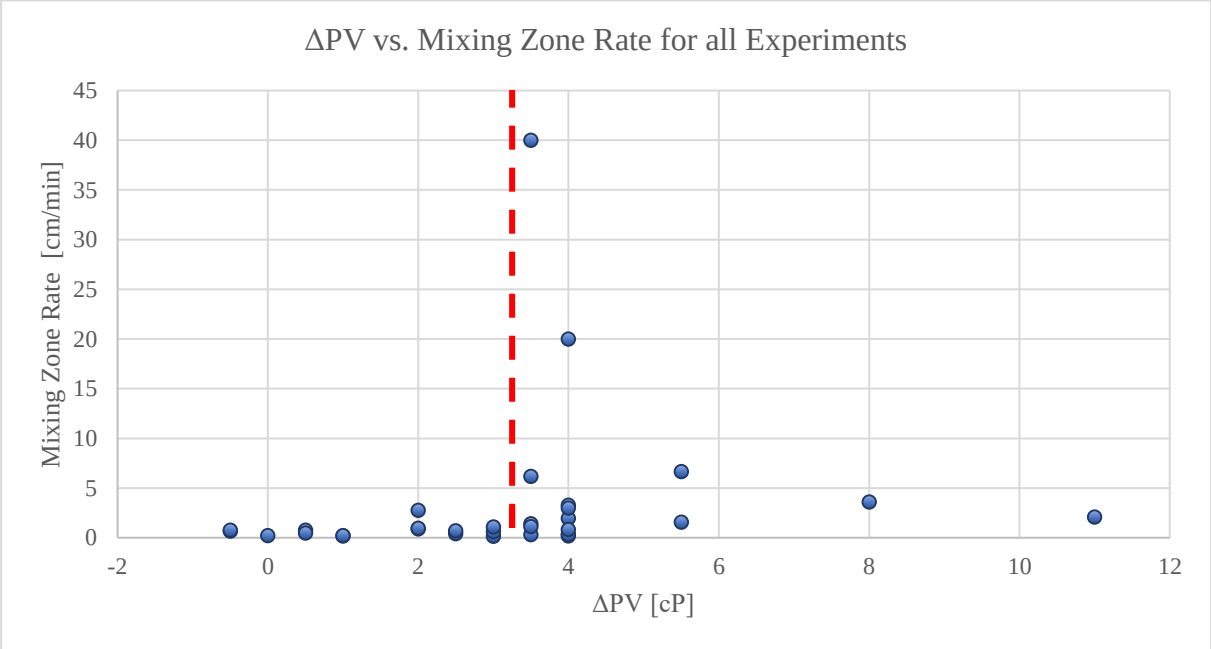

Figure 5.5 - ΔPV vs. Mixing Zone Rate including critical value

5.3 EFFECT OF WELL DIAMETER

During this thesis work, experiments have been conducted in four well sizes (10mm, 19.3mm, 31.5 and 40mm). Results showed that the mixing zone increases with increasing well diameter. Figure 5.6 shows the well diameters used for all experiments plotted against the mixing zone length.

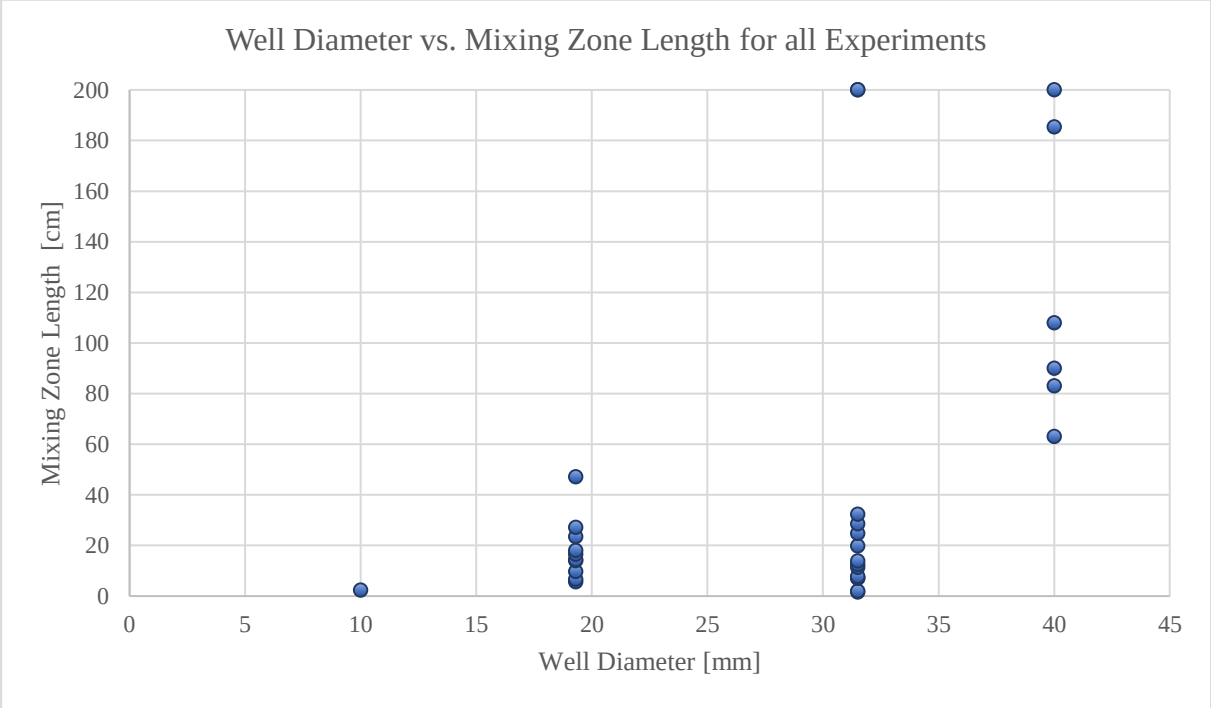

Figure 5.6 - Well Diameter vs. Mixing Zone Length

The effect of well diameter was investigated with several different experiments as shown in figure 5.7. The same HOL fluids were used for both diameters for each experiment, i.e. the only parameters that changed were well diameter and clearance.

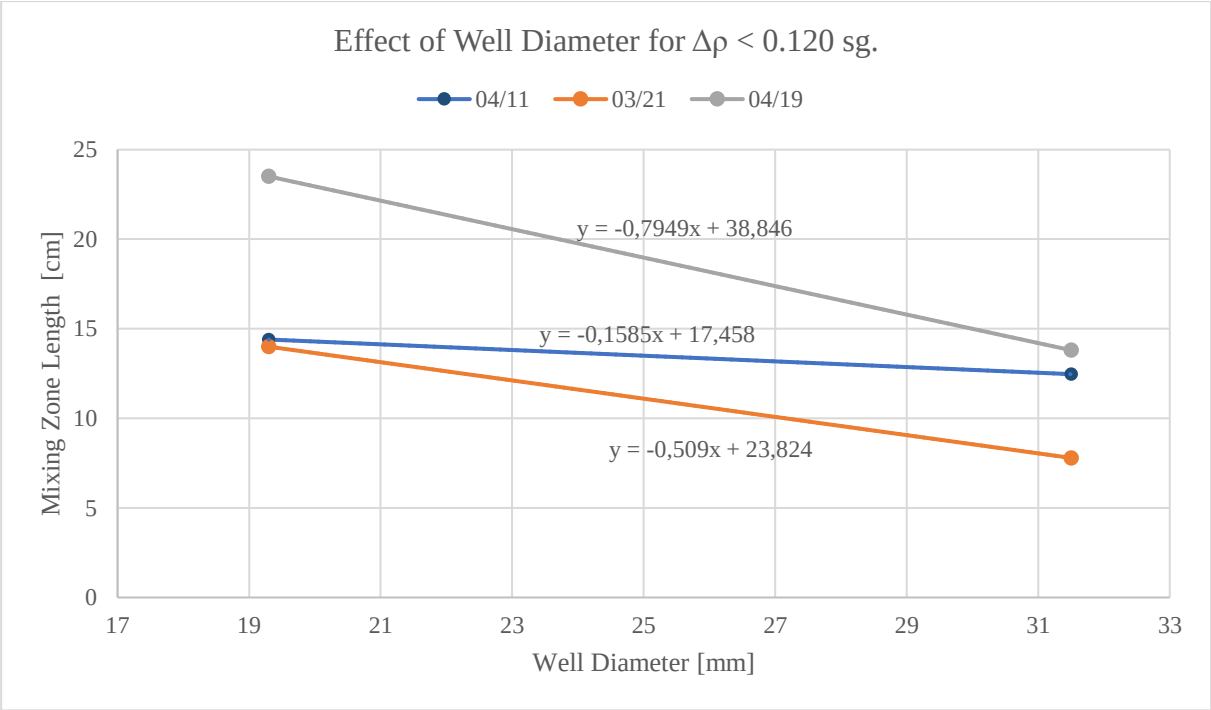

Figure 5.7 - Effect of Well Diameter for Δρ < 0.120 sg

As illustrated above, for Δρ < 0.120 sg, the mixing zone decreases up to 80 % when diameter increase 63 %.

However, for Δρ > 0.120 sg and the same increase in diameter, the mixing zone increases with 325 to 1114 %, as shown in figure 5.8.

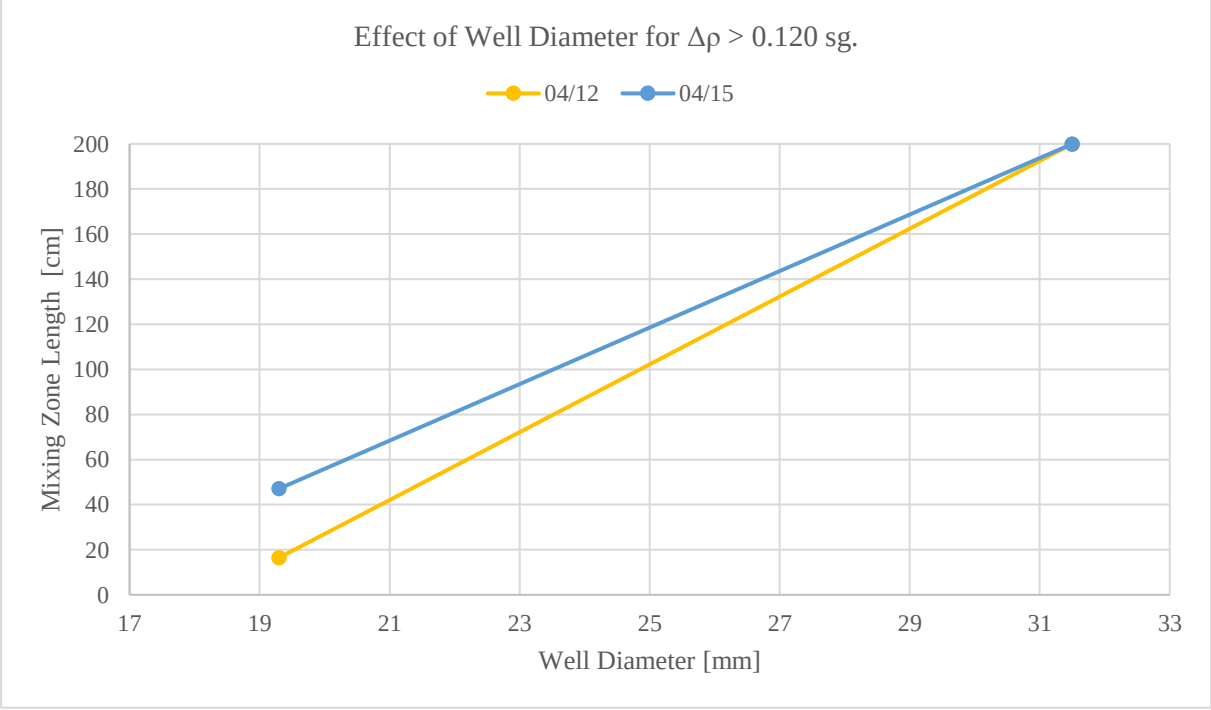

Figure 5.8 - Effect of Well Diameter for Δρ > 0,120 sg

5.4 EFFECT OF CLEARANCE

During the experimental study, it was considered if the clearance could be a factor that affect the mixing zone length and stability. To investigate this, two experiments were conducted and the results are shown in figure 5.9. The rheology of the drilling fluids used for the experiments are labeled as 03/23 and 04/04 according to the date of the fluid formulation and testing. The rheology of the drilling fluids are provided in appendix C.

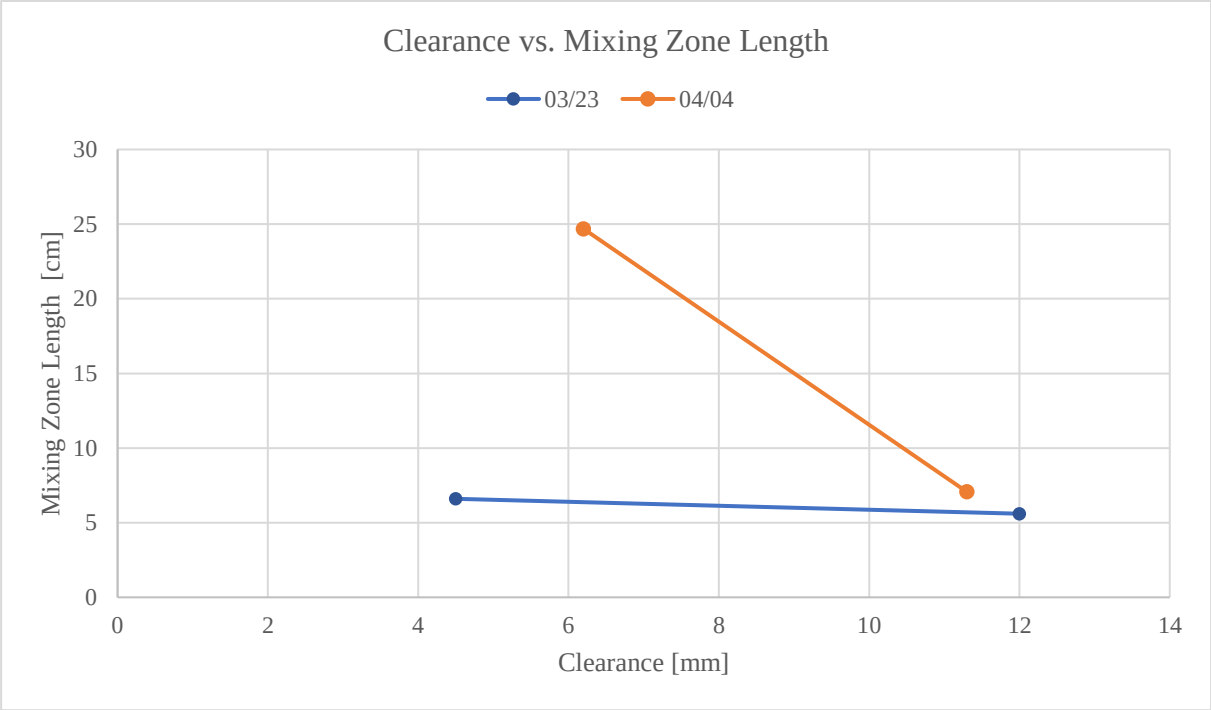

Figure 5.9 - Effect of Clearance

The reason why experiment 04/04 has higher difference in the mixing zone could be because $\Delta PV_{04/04}$ = 3.5 cP, which is slightly higher than the critical value suggested for ΔPV in section 5.2. This indicates that **the mixing zone decreases with increasing clearance**.

5.5 EFFECT OF LIGHT FLUID LSYS

Throughout the experiments it appeared that the LSYS for the light fluid could have an effect on the mixing zone length and mixing zone rate. The correlation for each well size is shown in the three graphs below.

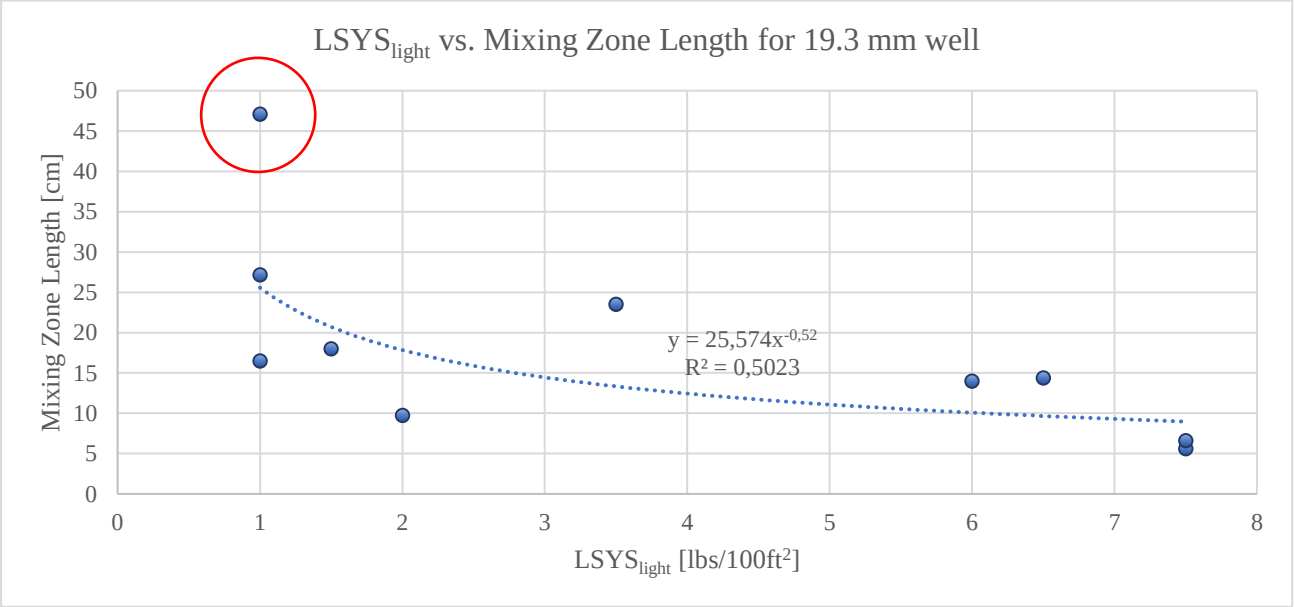

Figure 5.10 - Effect of LSYS$_{light}$ for 19.3 mm well

An abnormal data point in figure 5.10 is marked with a red circle. Compared to the other data points with the same LSYS$_{light}$, this one has larger value for ΔPV, which may indicate that the mixing zone length increases when ΔPV increases.

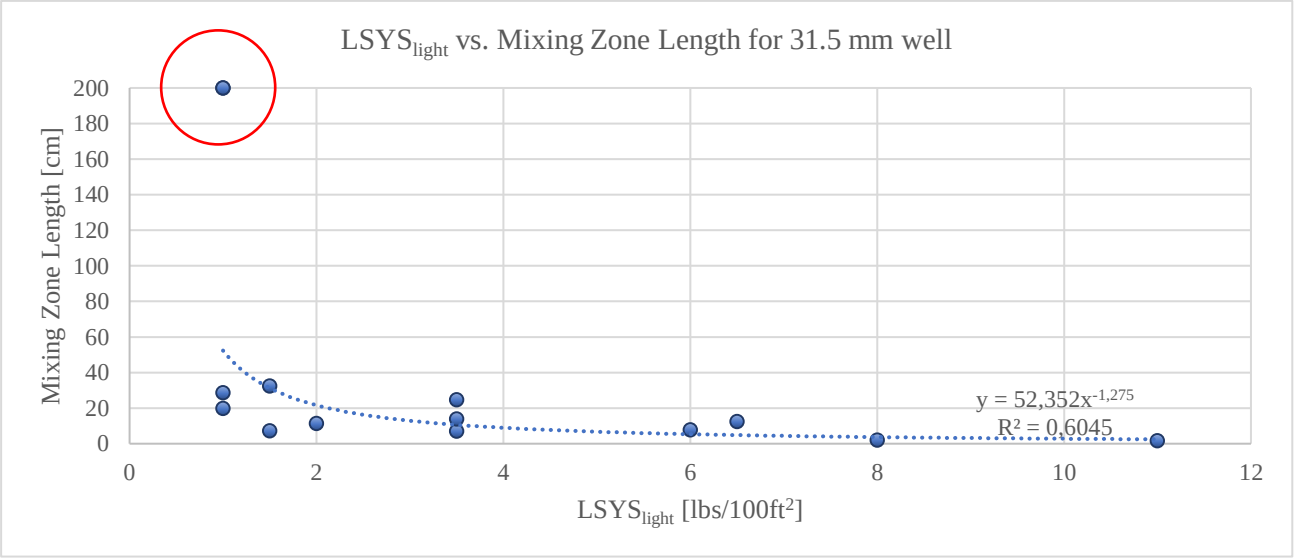

Figure 5.11 - Effect of LSYS$_{light}$ for 31.5 mm well

In figure 5.11, there is two data points located above the rest of the data series with $LSYS_{light}$ = 1 lbs/100ft^2. What separates these two data from the other data with the same value for $LSYS_{light}$ might be that one of the other data points has higher clearance, and the other one has both Δρ and ΔPV below the critical point suggested in section 5.1 and 5.2. This strengthens the suggestion for these critical values and may indicate that the **mixing zone length increases with decreasing clearance**.

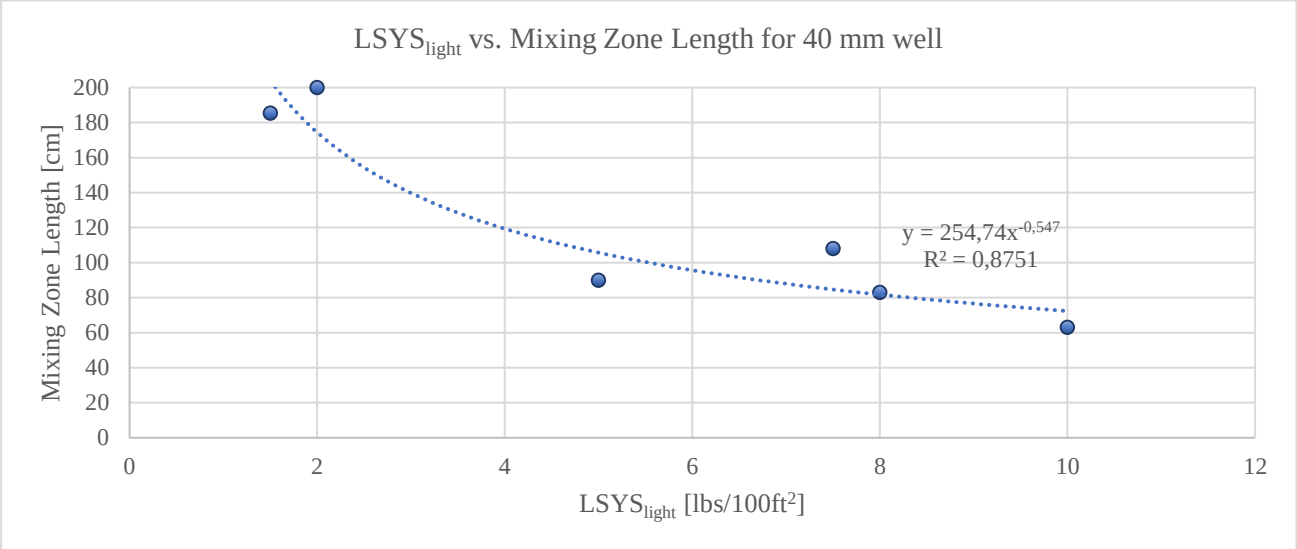

Figure 5.12 - Effect of $LSYS_{light}$ for 40 mm well

The three graphs above indicate that the mixing zone decreases with increasing LSYS for the light fluid.

5.6 EFFECT OF RHEOLOGICAL PARAMETERS

n is, as mentioned in section 3.8.3, the flow index of the Herschel Bulkley Fluid Model. The lower *n* is, the more shear thinning the fluid is. The graphs below may indicate that **when the product of the *n*-values increase, the mixing zone increases**.

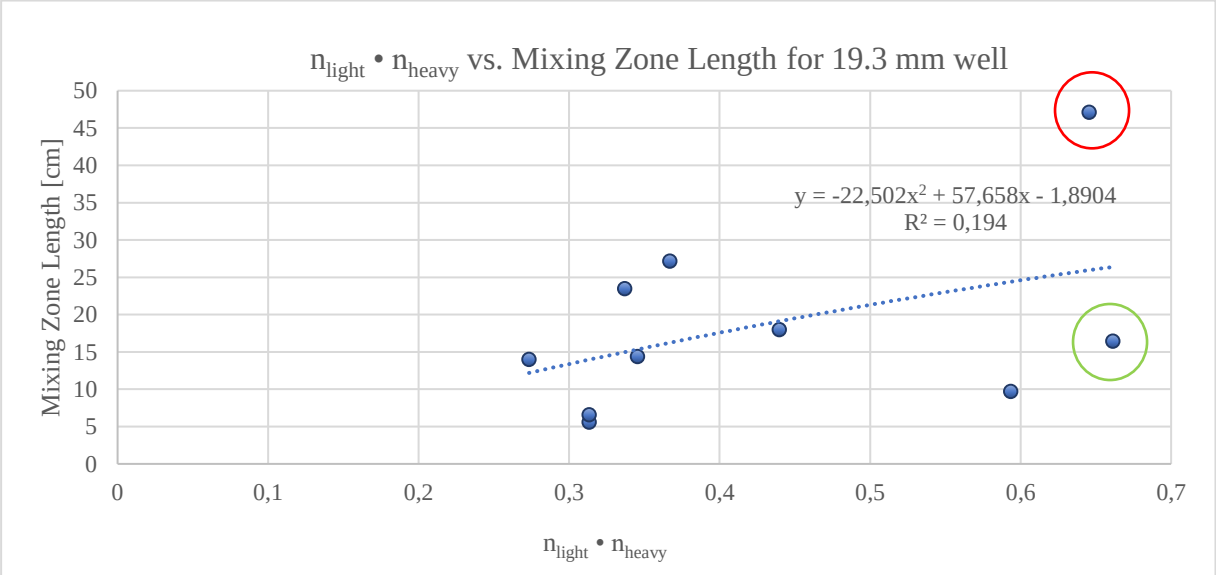

Figure 5.13 - Effect of the product of the n-parameters for 19.3 mm well

For figure 5.13, the anomalous data marked in the red circle may be higher than the data below, marked with a green circle, due to higher ΔPV and higher ΔLSYS. The density values and clearance are the same for both experiments.

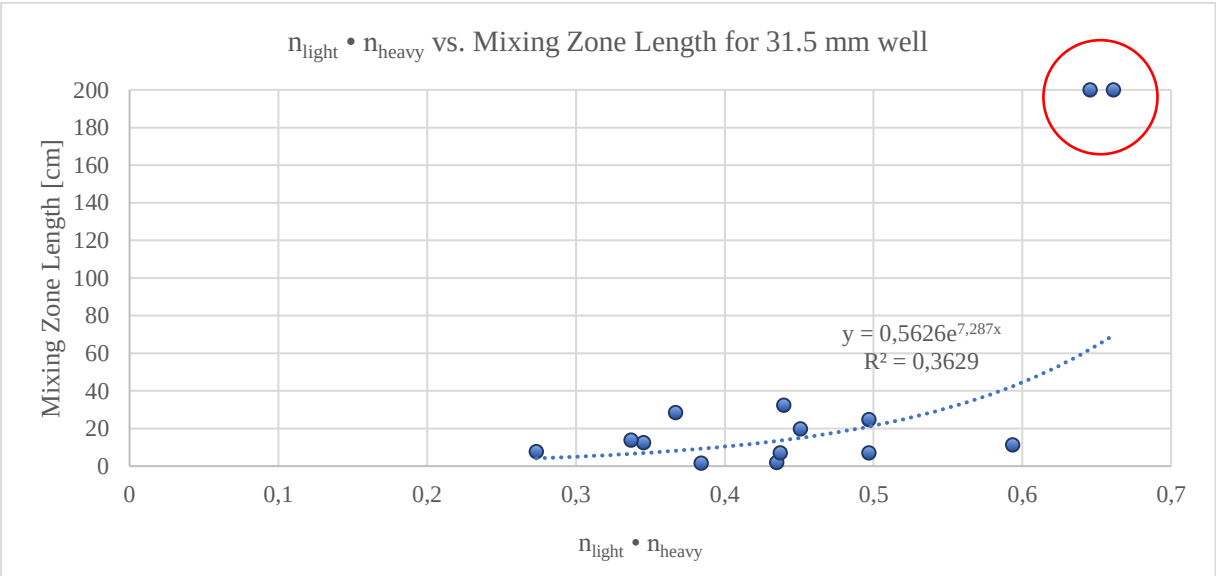

Figure 5.14 - Effect of the product of the n-parameters for 31.5 mm well

For the 31.5 mm well, there are two data points that stands out from the rest, as marked in the red circle in figure 5.14. One of them has a ΔPV = 5.5 cP that is larger than rest of the data points. The other one has a ΔPV = 4 cP, Δρ = 0,138 and ΔLSYS = 6.5. The other points in this data set that have the same or larger values ad a higher clearance than the data point in the red circle. This indicates that **the mixing zone increases with decreasing clearance**.

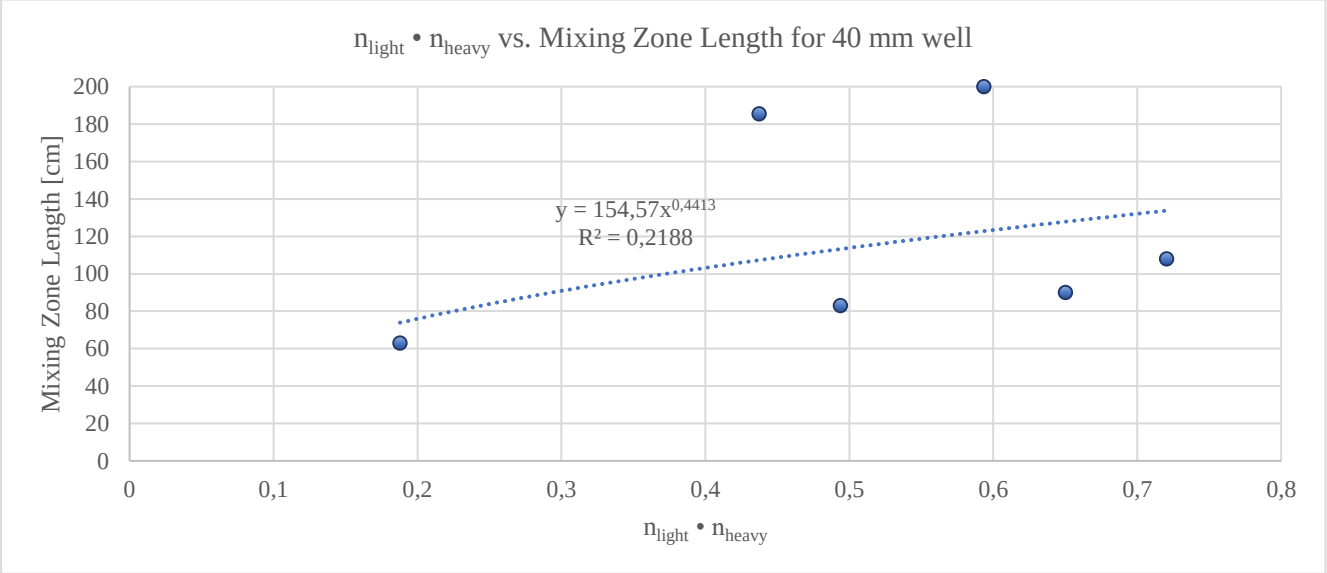

Figure 5.15 - Effect of the product of the n-parameters for 40 mm well

The viscometer readings θ_3 and θ_6 says something about the gel properties of the fluids and may therefore be decisive for the mixing zone. Figure 5.16 shows θ_3 for the light fluid plotted against the mixing zone length.

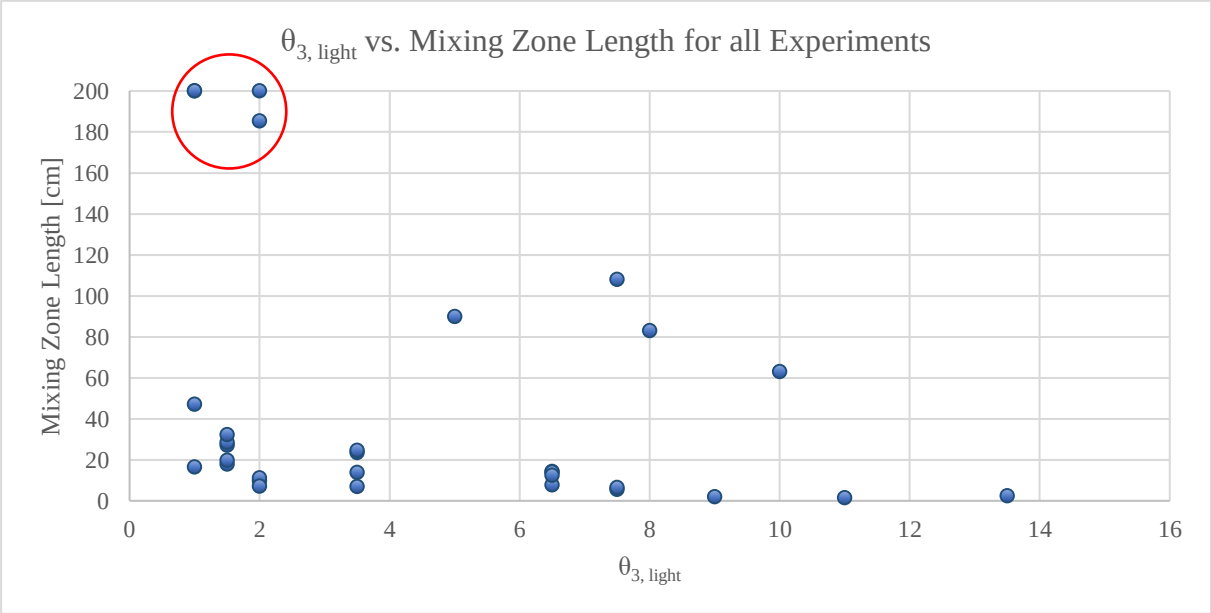

Figure 5.16 - Effect of $\theta_{3, light}$

5.7 VISCOELASTICITY TEST RESULTS

In addition to the rheological parameters, an attempt was made to further characterize and describe the viscoelasticity and investigate if there is a link with the mixing stability. For this, two fluid systems have been selected, namely the most stable and the most unstable of the HOL fluids. The best favorable with less mixing zone length was the fluids formulated and tested on 03/19 and the unstable fluid system was the one tested on 04/12. The rheology of the drilling fluids is provided in Appendix C.

Figure 5.17 shows the Anton Paar Rheometer used for measuring the viscoelasticity of fluid systems. Based on the viscoelasticity measurement, an attempt was made to delineate regions of stability and instability. Figure 5.18 shows the measured rheometer data of the worst HOL fluid (04/12.). As shown in the elastic dominated regions, the maximum storage modulus of the heavy and light fluids is in the order of 840 and 38 Pa respectively. Similarly, the loss modulus in the elastic is 75 and 4.5 Pa respectively.

Figure 5.17 - Anton Paar Rheometer [F05]

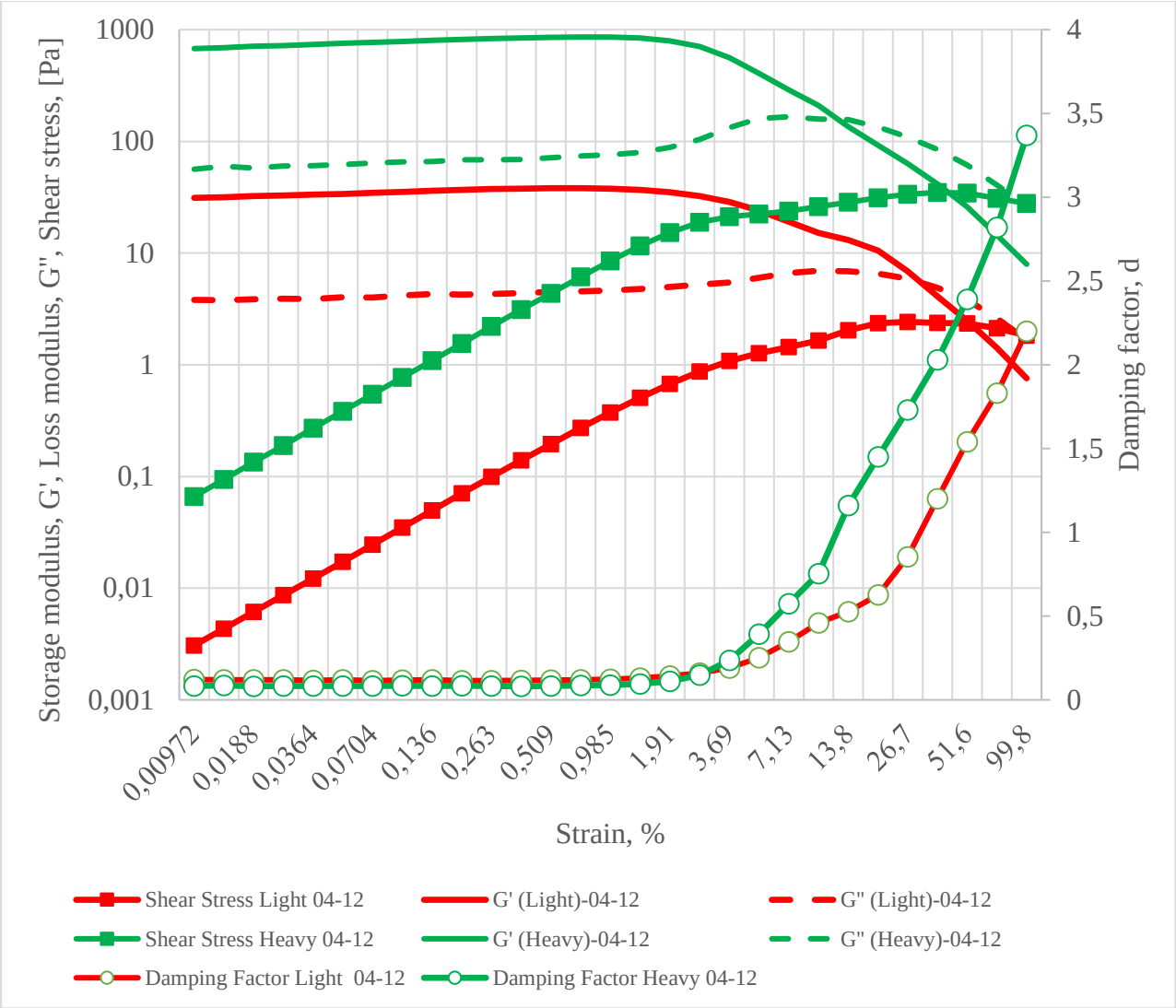

Figure 5.18 - Rheometer responses for the worst HOL mix (04/12)

Figure 5.19 shows the rheometer data for the best HOL fluids (03/19). In the elastic dominated regions, the maximum storage modulus of the heavy and light fluids is over 10 000 and 350 Pa respectively. One can also read that the loss modules are approximately being 370 and 30 Pa respectively.

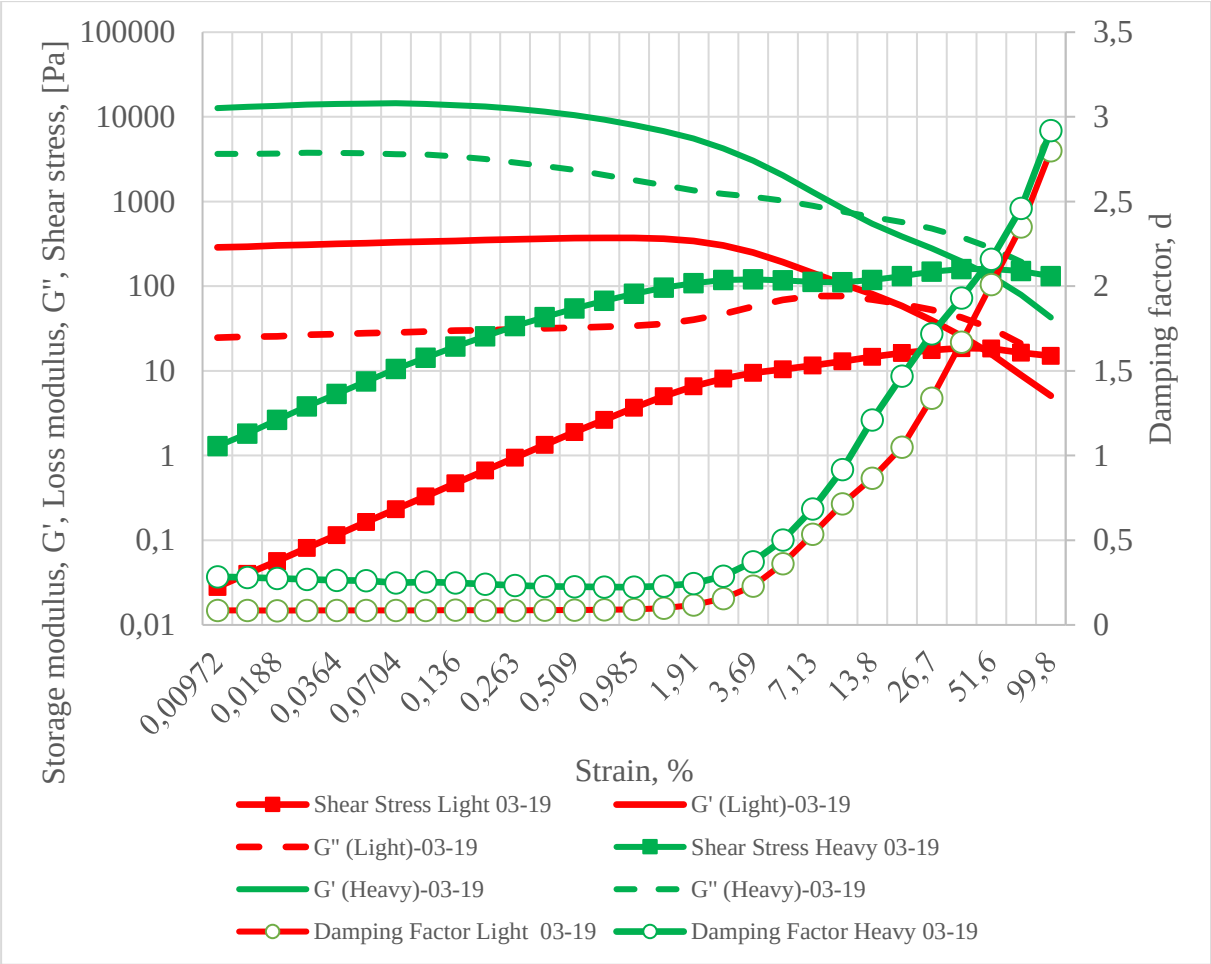

Figure 5.19 – Rheometer responses for the most stable mixing fluids (03/19)

Comparing the most unstable mix fluids with the most stable fluid mix, one can observe a huge difference in the viscoelasticity parameters. However, for a better interpretation, different parameters were combined until a good correlation was achieved. At first, the damping factor of the two fluids are plotted and shown in figure 5.20 and figure 5.21. As shown, the gap between HOL of the stable fluid systems (03/19) is narrower than unstable HOL fluids (04/12).

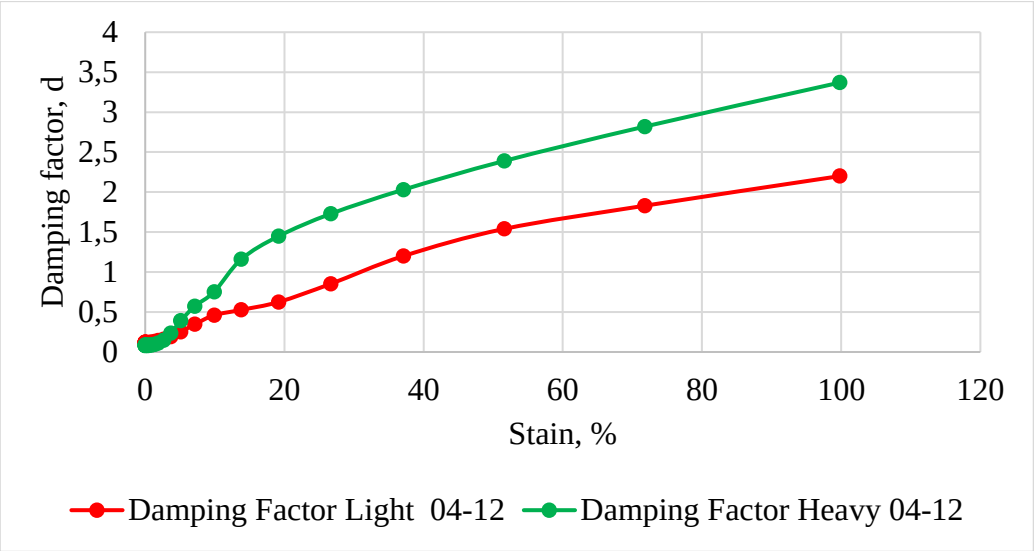

Figure 5.20 - Damping factor for the unstable mixing fluids

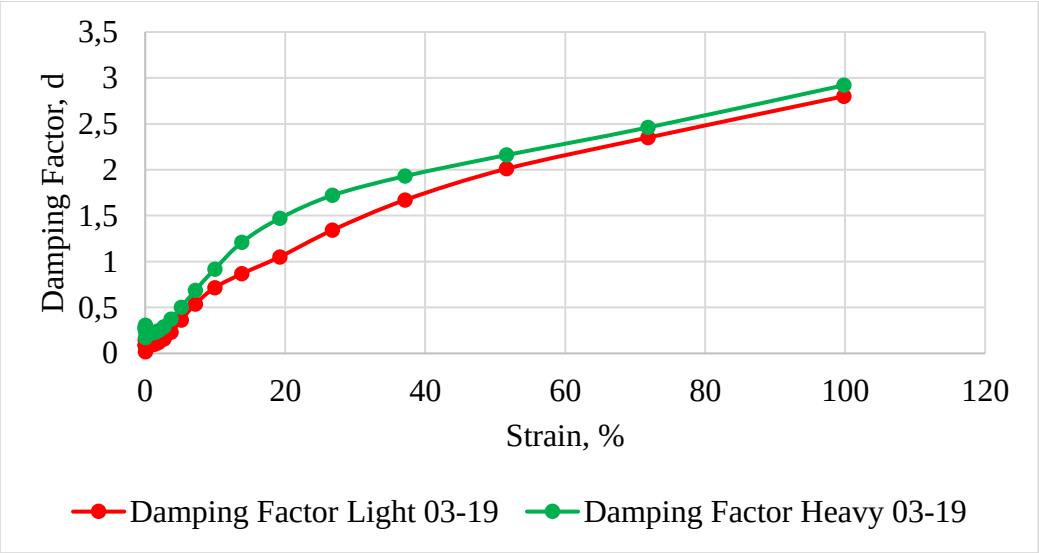

Figure 5.21 - Damping factor for the stable mixing fluids

For better quantification, the moduli difference and their ratio were calculated and displayed as in figure 5.22 and figure 5.23 respectively.

$$\Delta G' = H_{G'} - L_{G'}$$

$$\Delta G'' = H_{G''} - L_{G''}$$

$$\text{Ratio} = \Delta G'/\Delta G''$$

As can be observed from figure 5.23, the ratio = ΔG'/ΔG″ < 4 is associated to the 03/19 fluid and is considered as the stable region. On the other hand, the ratio = ΔG'/ΔG″ > 12 is considered as the unstable region.

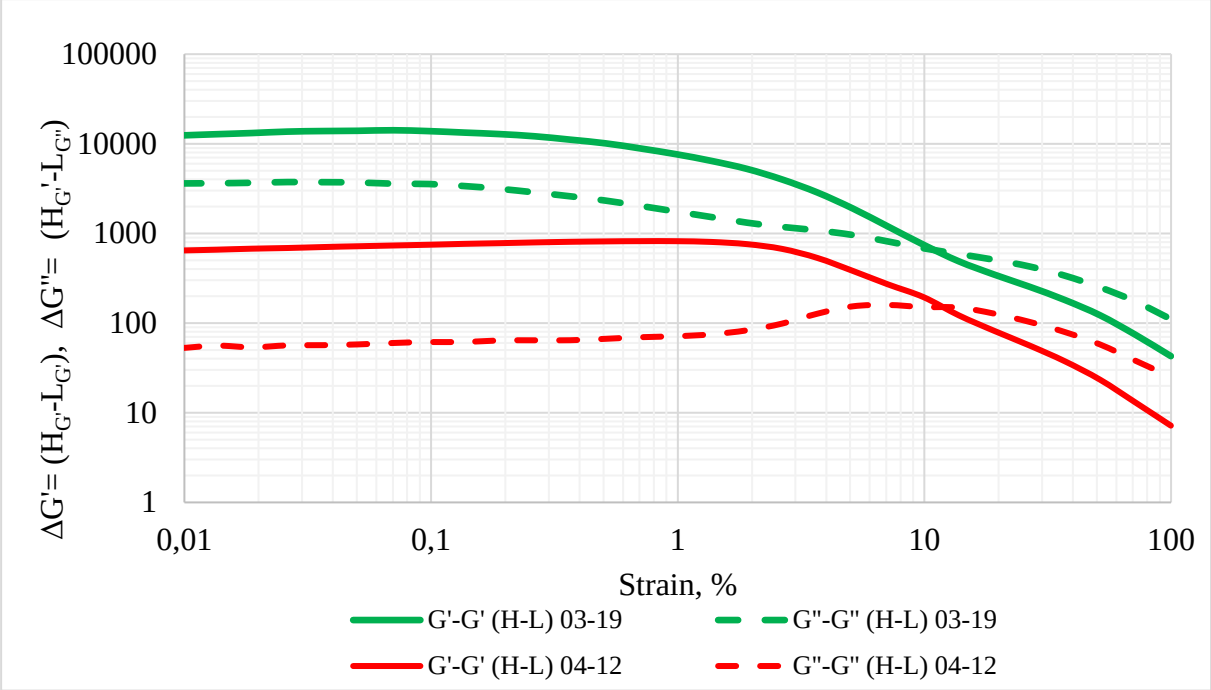

Figure 5.22 - Storage and Loss moduli difference between the HOL fluids

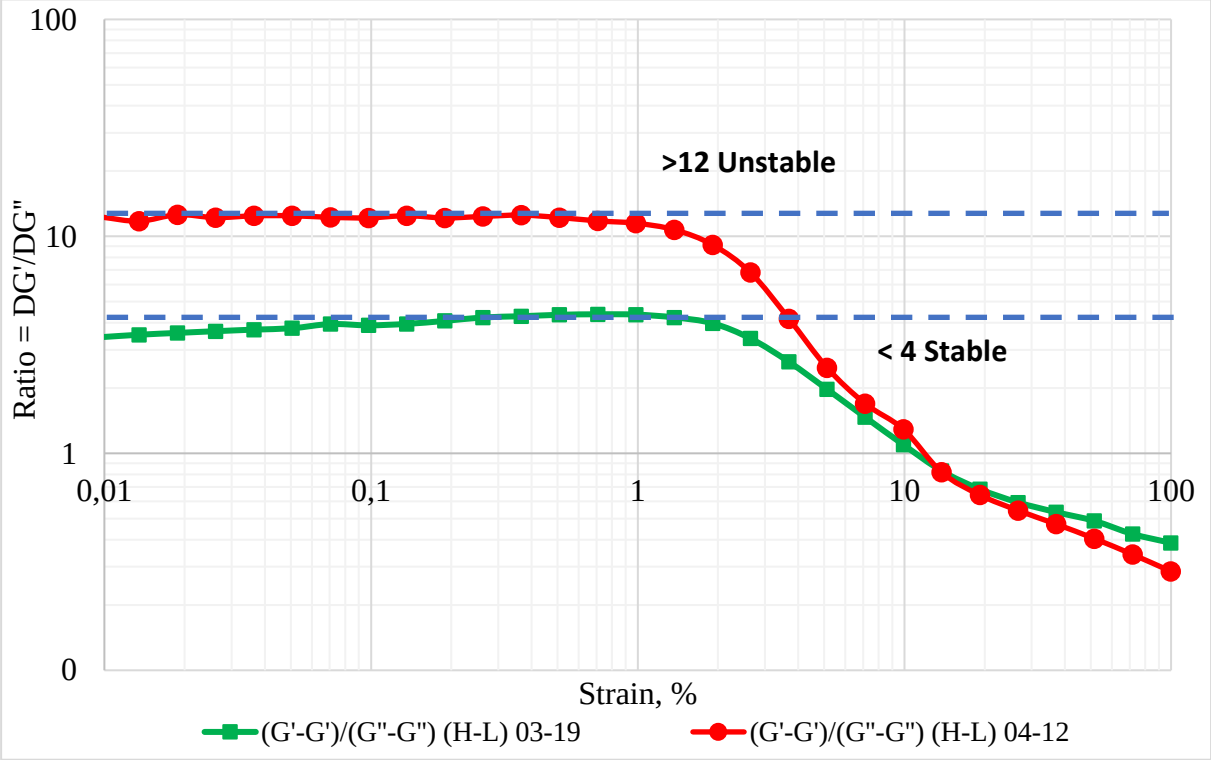

Figure 5.23 - Ratio of the storage modulus difference and the loss modulus difference

6 MODELLING OF EXPERIMENTAL DATA

This chapter presents modelling of experimental mixing zone length as a function of the measured drilling fluid and experimental well sizes. Here, two approaches of modelling will be presented. The first one by generating a correlation factor and the second one is by using multivariate regression technique.

6.1 MIXING ZONE AS A FUNCTION OF CORRELATION FACTOR

A drilling fluid is a complex system, which is described by different rheological and physical properties. During fluid formulation, it is difficult to design a fluid system having the same parameters while varying a single parameter. Therefore, in order to characterize the mix dynamics, an attempt was made to generate a correlation factor which combines several drilling fluid parameters. The results presented here is the best result achieved during the process. One clear observation is that analyzing the results obtained from the three well sizes together did not show trends. However, the analysis of individual well data shows better trends. The best correlation factor (CF) developed is achieved by the combined effect of flow index, plastic viscosity, yield stress and the changed in drilling fluid density of heavy and light is given as:

$$Correlation\ factor\ (CF) = n_{light} n_{heavy} \frac{PV_{heavy}}{PV_{light}} \left(\Delta\rho \cdot LSYS_{light}\right)^{-1} \qquad (6.1)$$

Figure 6.1 shows the fluid mix length versus the correlation factor of the experimental data conducted in 19.3 mm well size. From the curve, a polynomial correlation with $R^2 = 0.5055$ is obtained and the model reads:

$$Mixing\ Zone\ Length\ [cm] = 0.2482 \cdot CF^2 + 0.0941 \cdot CF + 13.052 \qquad (6.2)$$

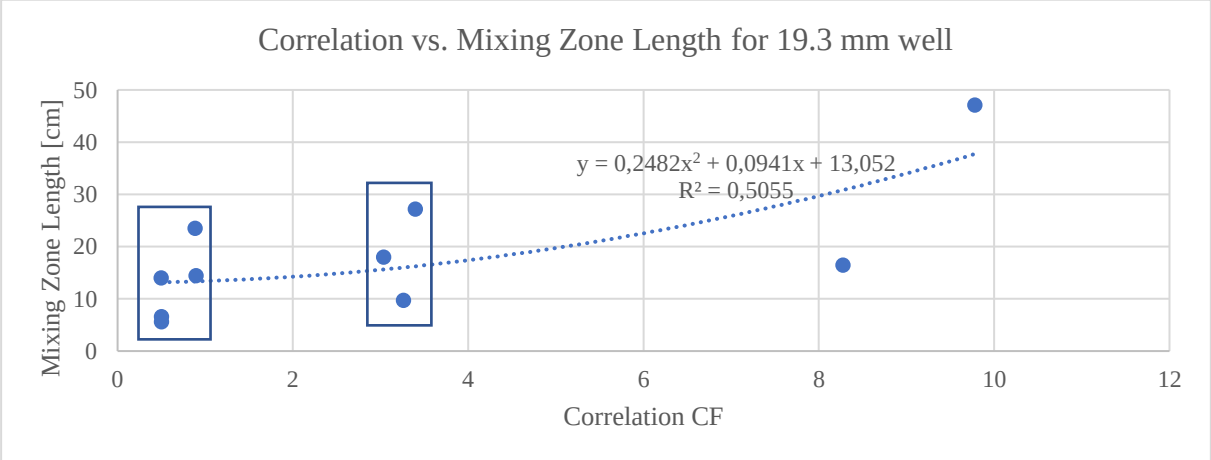

Figure 6.1 – Correlation vs. Mixing Zone Length for 19.3 mm well

As shown in the figure, a correlation factor less than 4 shows a lower mixing zone length. However, for the set of data shown in rectangular box, one need to evaluate further the other drilling fluid properties to judge if other parameters could have effect for the lower mixing zone length as well. The attempt here was just demonstrate the existence of a correlation factor with the mixing zone. However, more repeated experiments and extensive research is required to generate a better correlation factor. This piece of information, however, may provide information for Reelwell when designing drilling fluids.

Figure 6.2 shows correlation CF vs. mixing zone length for 31.5 mm well with an exponential trend line with $R^2 = 0.7568$, given as:

$$Mixing\ Zone\ Length\ [cm] = 4.136e^{0.4278 \cdot CF} \tag{6.3}$$

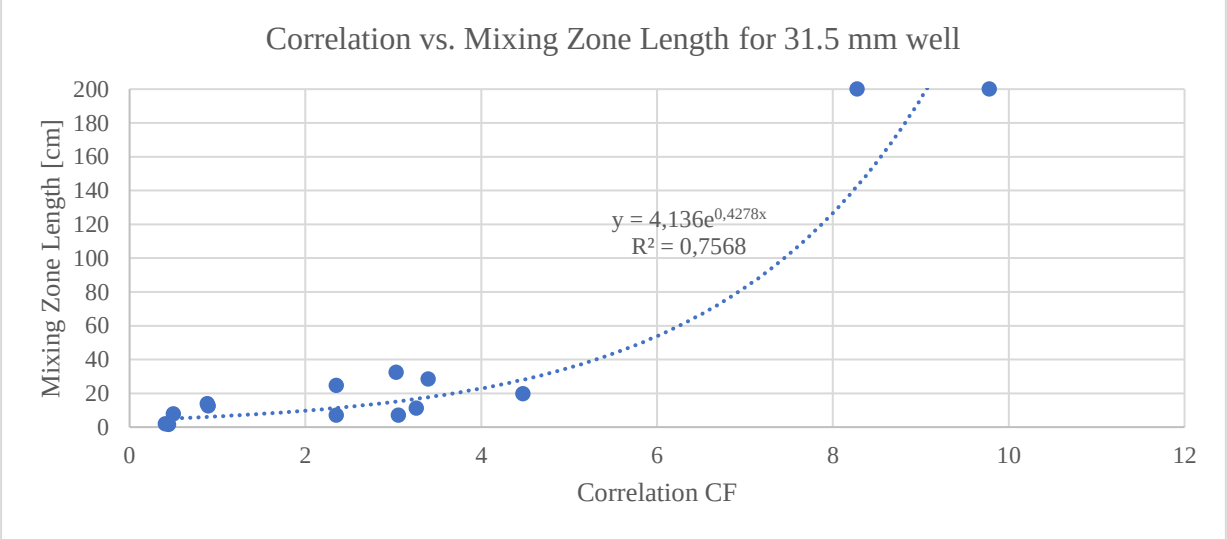

Figure 6.2 - Correlation vs. Mixing Zone Length for 31.5 mm well

Similarly, for the 40 mm wellbore, figure 6.3 shows the empirical mixing zone length vs. CF and ta polynomial model with $R^2 = 0.9452$ is given as:

$$Mixing\ Zone\ Lenght\ [cm] = 5.8343 \cdot CF^2 + 18.662 \cdot CF + 75.197 \tag{6.4}$$

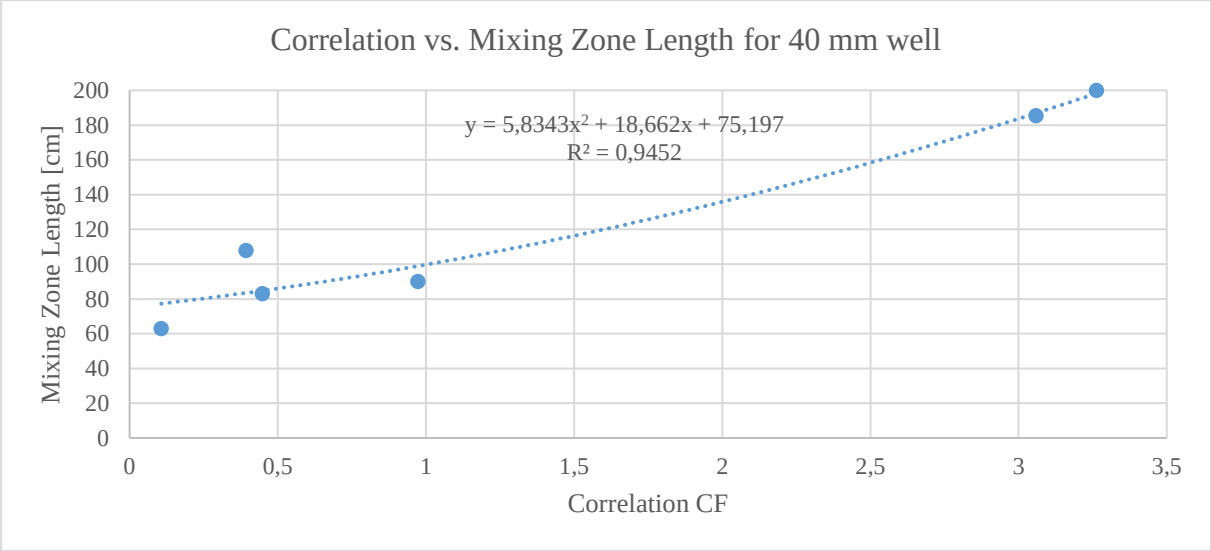

Figure 6.3 - Correlation vs. Mixing Zone Length for 40 mm well

The following three graphs shows the models for correlation factors created above plotted with the experimental data to illustrate the fit of the models.

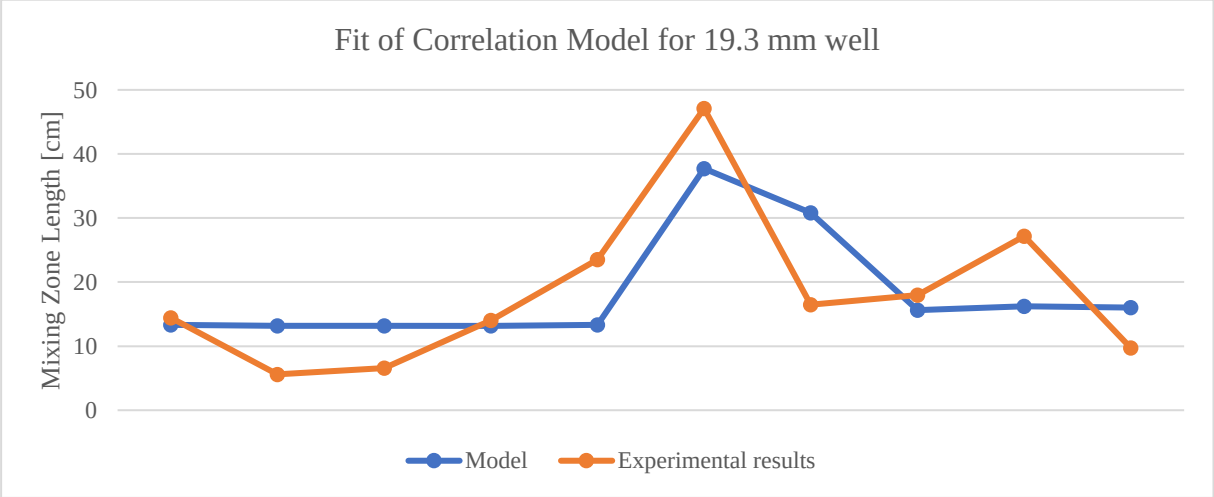

Figure 6.4 - Comparisons between experimental mixing length data with model prediction for 19.3 mm well

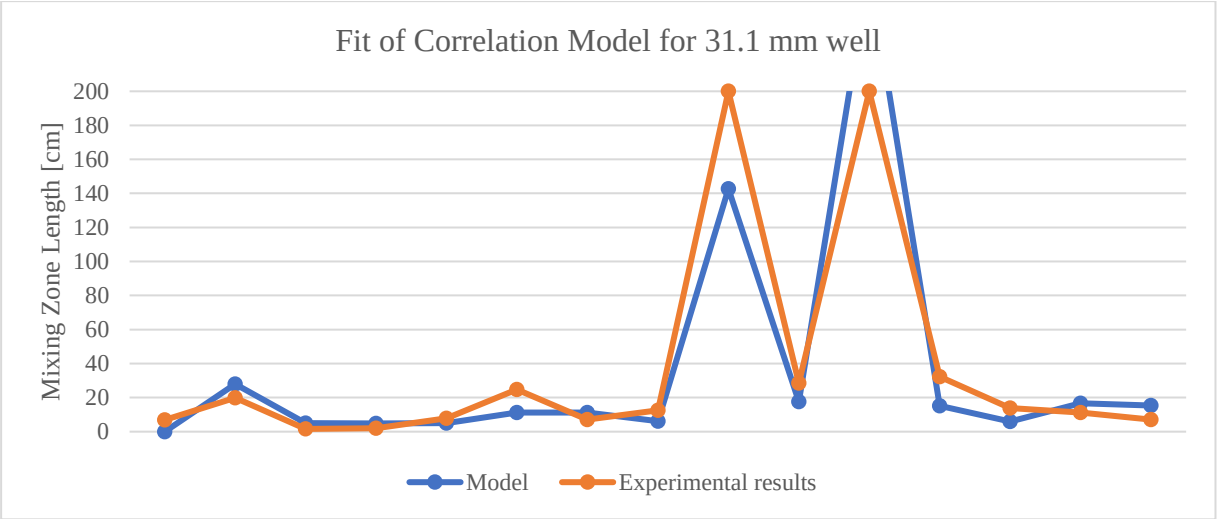

Figure 6.5 – Comparisons between experimental mixing length data with model prediction for 31.5 mm well

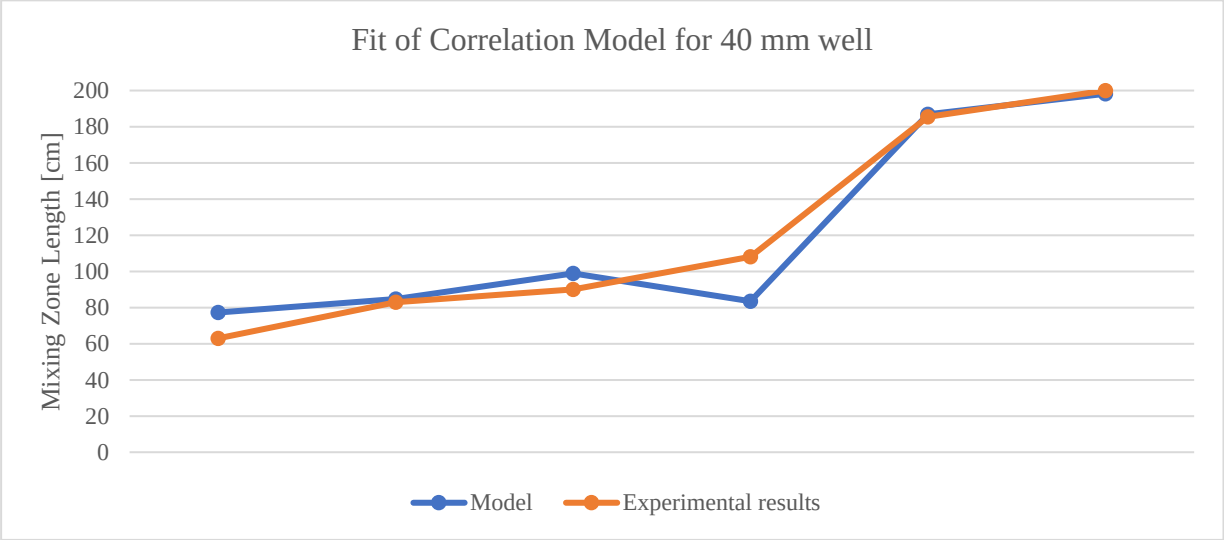

Figure 6.6 - Comparisons between experimental mixing length data with model prediction for 40 mm well

6.2 MULTIVARIATE MIXING ZONE MODELLING

A simple linear regression estimates the value of Y based on a given parameter X. This can be mathematically described by

$$Y = \beta_0 + \beta_1 X, \tag{6.5}$$

where β_0 is the Y intercept and β_1 is the slope of X (or coefficient).

On the other hand, if there are several X parameters such as the experimental data measured in this thesis work, a multivariate regression technique is used instead of equation 6.5. Multivariate regression analysis generates the relationships of measured parameters as a linear combination of several independent variables [T21]. The method is based on statistical principle and its application in diverse. In multiple regression, the independent parameter (Y) is written as a function of independent variables (X_1, X_2, …, X_n), and is given by:

$$Y = \beta_0 + \beta_1 X_1 + \beta_2 X_2 + \beta_3 X_3 + \beta_4 X_4 + \beta_5 X_5 + \beta_6 X_6 + \ldots \beta_n X_n, \tag{6.6}$$

where β_0 is the intercept (constant) and (β_1, β_2, …, β_n) are the regression coefficients. In this thesis work, Y is the mixing zone length and $X_{1\text{-}n}$ are the drilling fluid rheological parameters, well size, clearance and density of heavy and light fluid along with parameter differences.

Example #1

The first attempt to generate an empirical correlation equation used a total of eight selected data. As shown in the table below, a multivariate-based linear regression correlation equation has been developed with $R^2 = 0.98391626$. The model reads:

$$Mixing\ Zone\ [cm] = a \cdot Clearance + b \cdot LSYS_{Heavy} + c \cdot \Delta\rho + d \cdot \Delta PV + e \cdot \Delta LSYS + f, \tag{6.7}$$

where the coefficients are shown in table 6.1.

Table 6.1 – Coefficients of multivariate model example #1

Coefficients	***Values***
a	7.27827766
b	-1.8130386
c	21.6279995
d	-2.51922404
e	1.86128444
f	-6.46203065

Table 6.2 - Higher and lower clearance drilling fluid parameters, experimental and model mix prediction

# of data	Clearance [mm]	$LSYS_{heavy}$	Δρ	ΔPV	ΔLSYS	Experimental data	Model
1 (05/03)	14.7	9	0.216	4	4	90	86
2 (05/09)	14.7	12	0.18	2	4	83	85
3 (04/27 – 2)	14.7	18	0.39	11	8	63	64
4 (04/17 – 1)	6.2	19.5	0.138	3	18	32	32
5 (04/13 – 1)	6.2	13	0.144	2	12	29	36
6 (04/13 – 2)	4.5	13	0.144	2	12	27	23
7 (04/04 – 1)	6.2	7	0.114	4	3.5	25	25
8 (04/19 – 2)	4.5	20.5	0.102	0.5	17	24	22

Results of the comparison between experimental data and model data prediction are shown in figure 6.7.

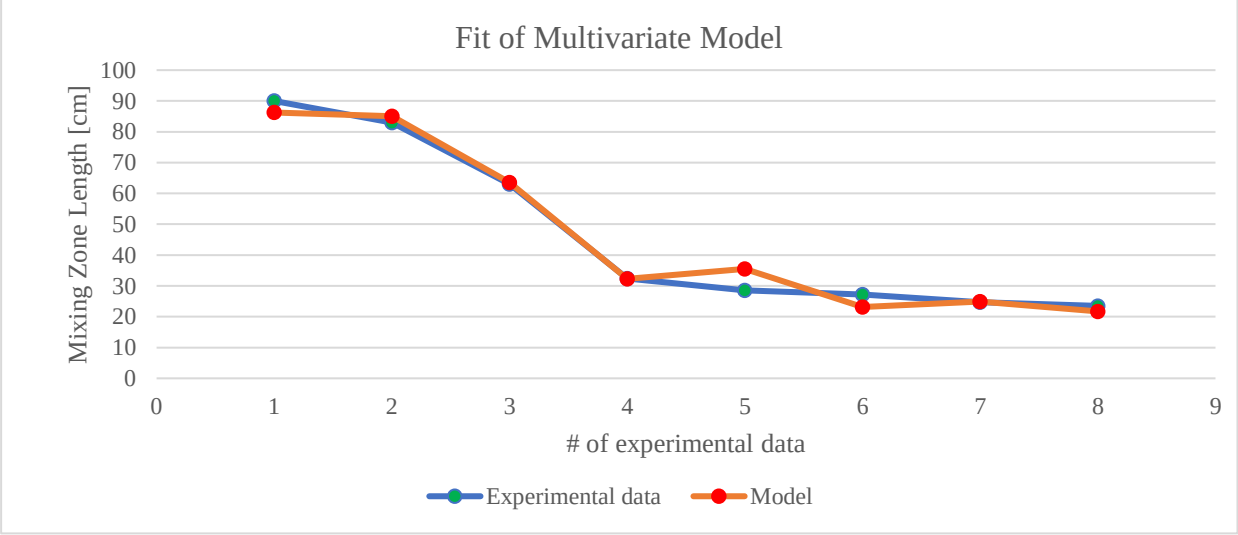

Figure 6.7 – Comparisons between experimental mixing length data with model prediction

Example #1, model testing #1, Lower Clearance

The model given in equation 6.7 has been tested on a lower clearance of five dataset. Table 6.3 provides the drilling fluid parameters and clearances. Figure 6.8 shows the plot comparison between experimental data and model prediction of mixing zone length. Results shows quite good prediction except the last data set.

Table 6.3 - Lower clearance and drilling fluid parameters

# of data	Clearance [mm]	LSYS	Δρ	ΔPV	ΔLSYS
7	4.5	19.5	0.138	3	18
8	4.5	7.5	0.138	4	6.5
9	4.5	13	0.084	2.5	6.5
10	4.5	18	0.1	0.5	12
11	6.2	13	0.084	2.5	6.5

Figure 6.8 - Comparisons between lower clearance experimental mix length data with model prediction

Example #1, model testing #2, Higher Clearance

Further, the model is also tested with higher clearance on four datasets. Table 6.4 shows the drilling fluid parameters and clearance input parameters. Figure 6.9 displays the plot comparison between the experimental data and model prediction of mixing zone length. Results shows quite good prediction except the first data set.

Table 6.4 - Higher clearance and drilling fluid parameters

ID well bore / test #	Clearance	LSYS	Δρ	ΔPV	ΔLSYS
04/30 - 1	14.7	8	0.462	8	0.5
05/03	14.7	9	0.216	4	4
05/09	14.7	12	0.18	2	4
04/27 - 2	14.7	18	0.39	11	8

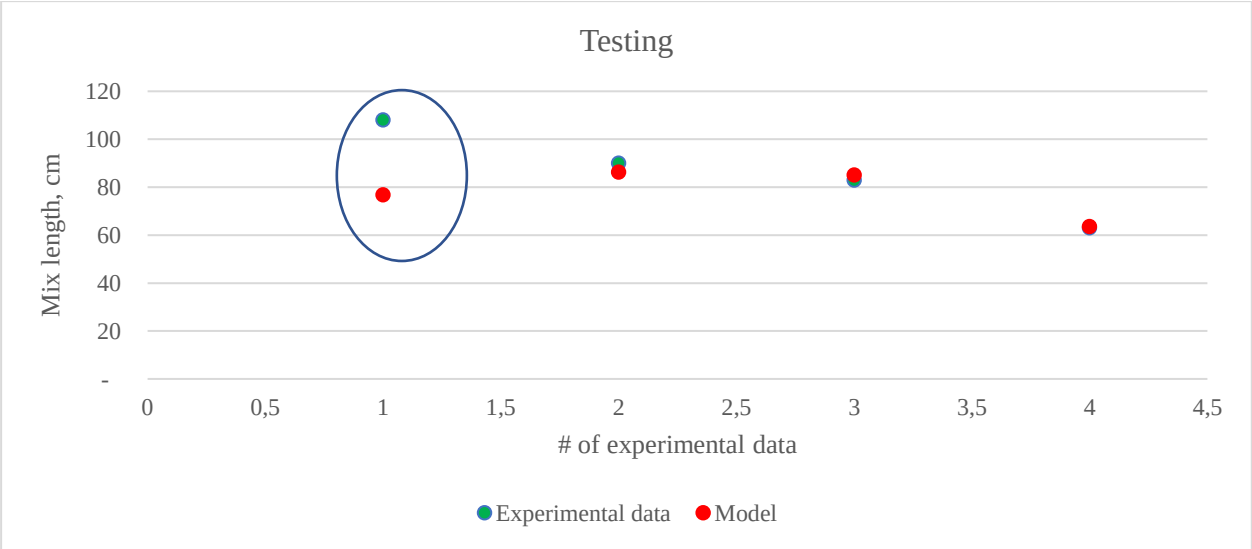

Figure 6.9 - Comparisons between higher clearance experimental mix length data with model prediction

Note that this model is only developed and tested with experiments showing short mixing zones.

Example #2

When analyzing the data, it was found out that the gel strength related to θ_3 is also related to the stability of the mixing zone. In example #2 modelling scenario, several drilling fluid properties which influence the mixing zone are included. Moreover, higher mixing zone lengths associated with the lower gel strength / or light drilling fluid's yield strength are considered.

Based on the 19.3 mm well's 10 experimental data, the mixing zone as a function of well and drilling fluid parameters is given as:

$$Mixing\ Zone\ [cm] = Clearance \cdot a + PV_{light} \cdot b + \theta_{3,\,light} \cdot c + LSYS_{heavy} \cdot d + n_{heavy} \cdot e + \theta_{3,\,heavy} \cdot f + \Delta\rho \cdot g + \Delta PV \cdot h + \Delta LSYS \cdot i + j \quad (6.8)$$

Table 6.5 – Correlation coefficients for 19.3 mm well

Parameters for 19.3 mm well		**Coefficients**
	j	-31,44290565
Clearance [mm]	a	-0,133333333
PV_{light}	b	14,61413492
$\theta_{3,\,light}$	c	98,22576687
$LSYS_{heavy}$	d	-63,59771391
n_{heavy}	e	120,4958877
$\theta_{3,\,heavy}$	f	-37,6324171
$\Delta\rho$	g	-1254,198869
ΔPV	h	10,159317
$\Delta LSYS$	i	102,5032073

Table 6.6 – Regression Statistics for 19.3 mm well

Regression Statistics for 19.3 mm Well	
Multiple R	1
R Square	1
Adjusted R Square	65535
Standard Error	0
Observations	10

Figure 6.10 shows the comparison between the model and the experimental data. As shown, the model perfectly captures the experimental data.

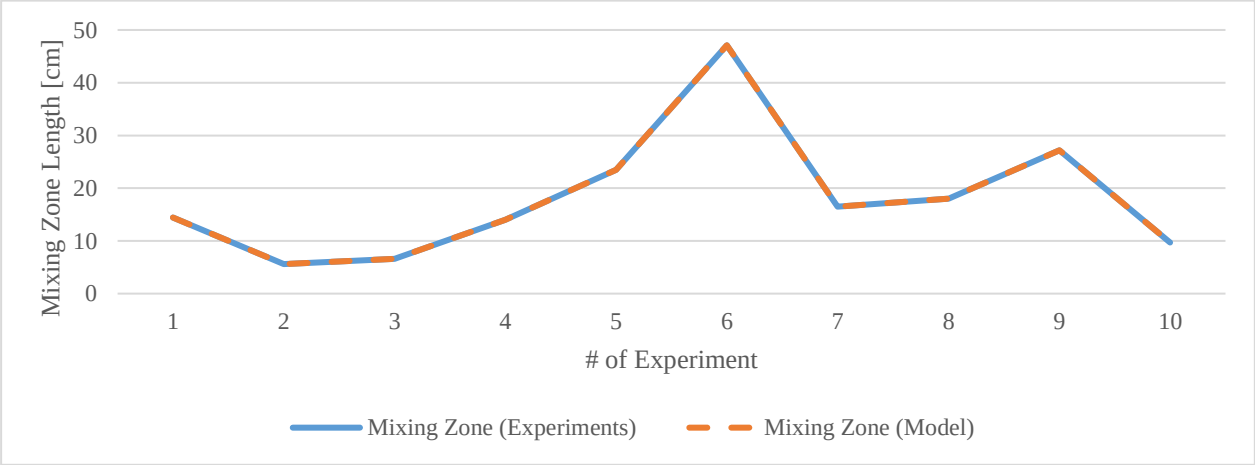

Figure 6.10 – Comparison between experimental mixing zone length data with model prediction for 19.3 mm well

Similarly, for the 31.5 mm well section, modelling of 14 experimental data, the multivariate correlation factor along with the regression statistics are provided in table 6.7 and table 6.8. Figure 6.11 shows the comparisons between the model and the experimental data.

Table 6.7 – Correlation coefficients for 31.3 mm well

Parameters of 31.5 mm well		***Coefficients***
	l	-2776,629316
Clearance [mm]	a	-5,478411811
PV_{light}	b	1,220292818
$LSYS_{light}$	c	-395,5148001
n_{light}	d	687,4623882
$\theta_{3,\ light}$	e	285,1667099
ρ_{heavy}	f	2401,865537
PV_{heavy}	g	-8,047219005
n_{heavy}	h	641,9167726
$\theta_{3,\ heavy}$	i	86,06055743
$\Delta\rho$	h	-5924,317467
ΔLSYS	k	-82,29676977

Table 6.8 – Regression Statistics for 31.5 mm well

Regression Statistics for 31.5 mm Well	
Multiple R	0,979291
R Square	0,959012
Adjusted R Square	-0,26642
Standard Error	35,18843
Observations	14

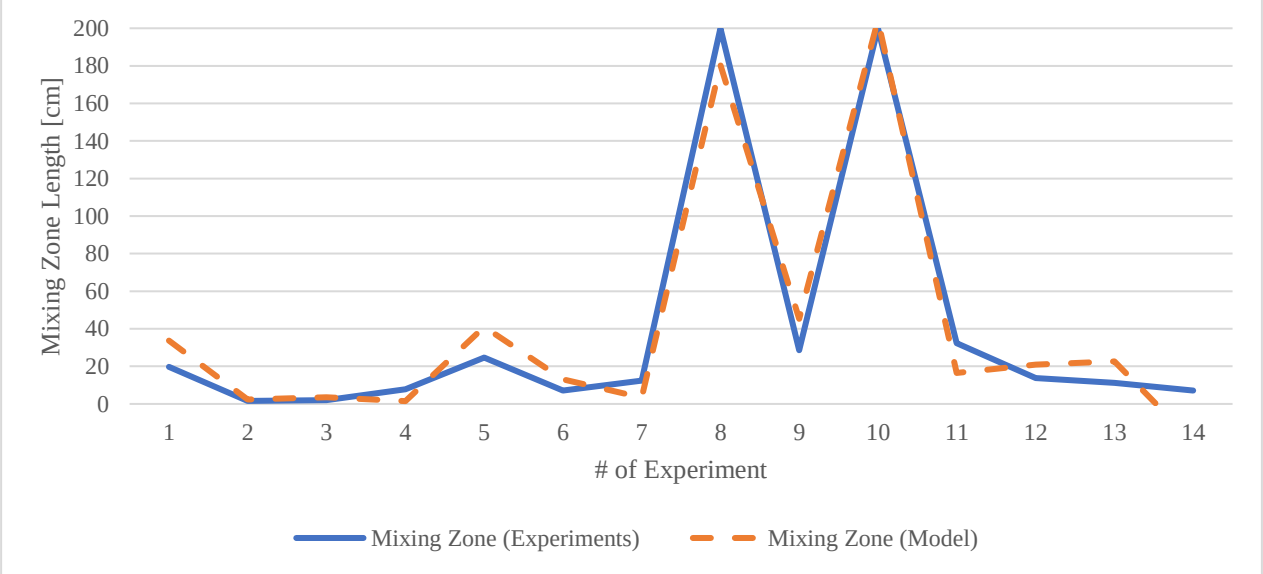

Figure 6.11 - Comparison between experimental mixing zone length data with model prediction for 31.5 mm well

The last analysis was with the 40 mm wellbore, which considered six experimental data. Table 6.9 displays the correlation coefficient and table 6.10 the regression statistical data. Here, one can also observe a perfect match. Figure 6.12 plots the comparison between the model and the experimental data.

Table 6.9 -Correlation coefficients for 40 mm well

Parameters for 40 mm well		***Coefficients***
	f	234,8711789
$LSYS_{light}$ [HB]	a	-21,16317565
n_{light}	b	-390,9043093
PV_{heavy}	c	72,573219
$\theta_{3,\ heavy}$	d	-9,313129005
ΔPV	e	-102,7147114

Table 6.10 – Regression Statistics for 40 mm well

Regression Statistics for 40 mm Well	
Multiple R	1
R Square	1
Adjusted R Square	65535
Standard Error	0
Observations	6

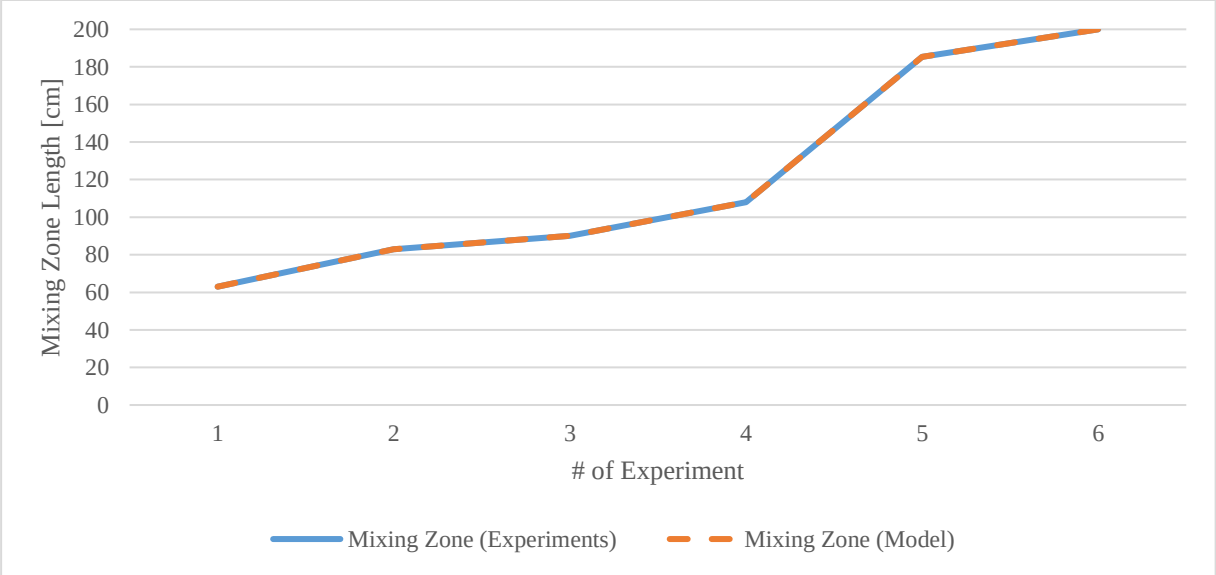

Figure 6.12 - Comparison between experimental mixing zone length data with model prediction for 40 mm well

7 FURTHER RESULTS DISCUSSIONS

In the following sections, the method of analysis, effect of drilling fluid properties and the effect of experimental well geometry are discussed.

7.1 METHOD OF ANALYSIS

One of the main concerns for the validation of the results from this experimental investigation considers the length of the actual mixing zone. All analyses are based on what can be seen on the surface of the plastic pipes. The fluids used are not transparent, i.e. one does not know how it looks at the inner section close to the drill string by using the picture analysis method used in these experiments.

To deal with this concern, the theory presented in the end of section 3.5 is assumed. The theory is that the centrifugal force from the rotation forces the heavy fluid out towards the wall of the pipes. Due to the gravity, the fluid with the greatest density will be exposed to higher gravitational force and therefore move downwards.

With these theories in mind, it is assumed that the heavy fluid will be forced out towards the inner wall of the well pipe and then downwards as seen in figure 7.1.

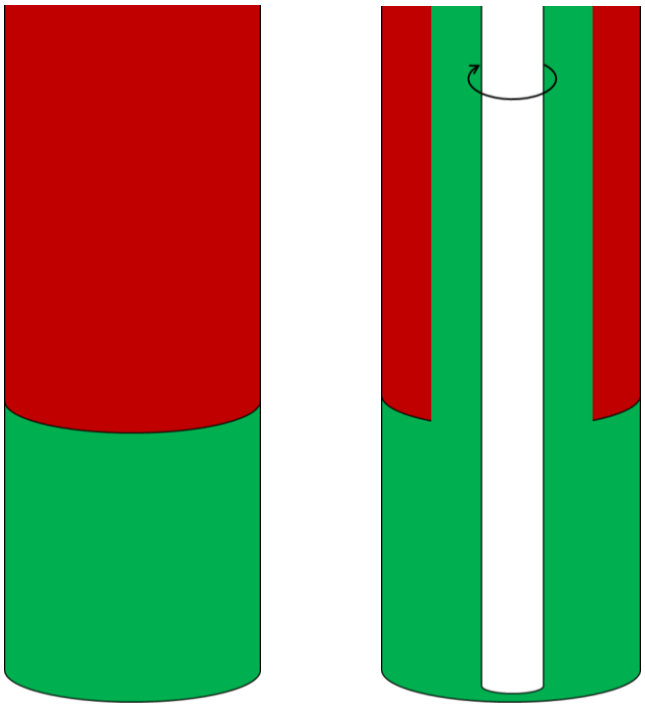

Figure 7.1 - Mixing Zone seen from the outside (left) and inside (right) of the pipe [F04]

The problem is, one does not know how thick the section of heavy fluid near the inner wall of the well pipe is. So, as mentioned in section 4.2.3, it is assumed that if an amount of heavy fluid moves down from its initial spot, the same amount of light fluid has to move upwards. Therefore, when calculating the mixing zone from pictures, both when using visual analysis and MatLab analysis, the downward movement of the heavy fluid is considered as the half of the actual mixing zone. Figure 7.2 illustrates how the assumed mixing zone development appear visually and figure 7.3 illustrates how the actual mixing zone is assumed to be for the same experiments.

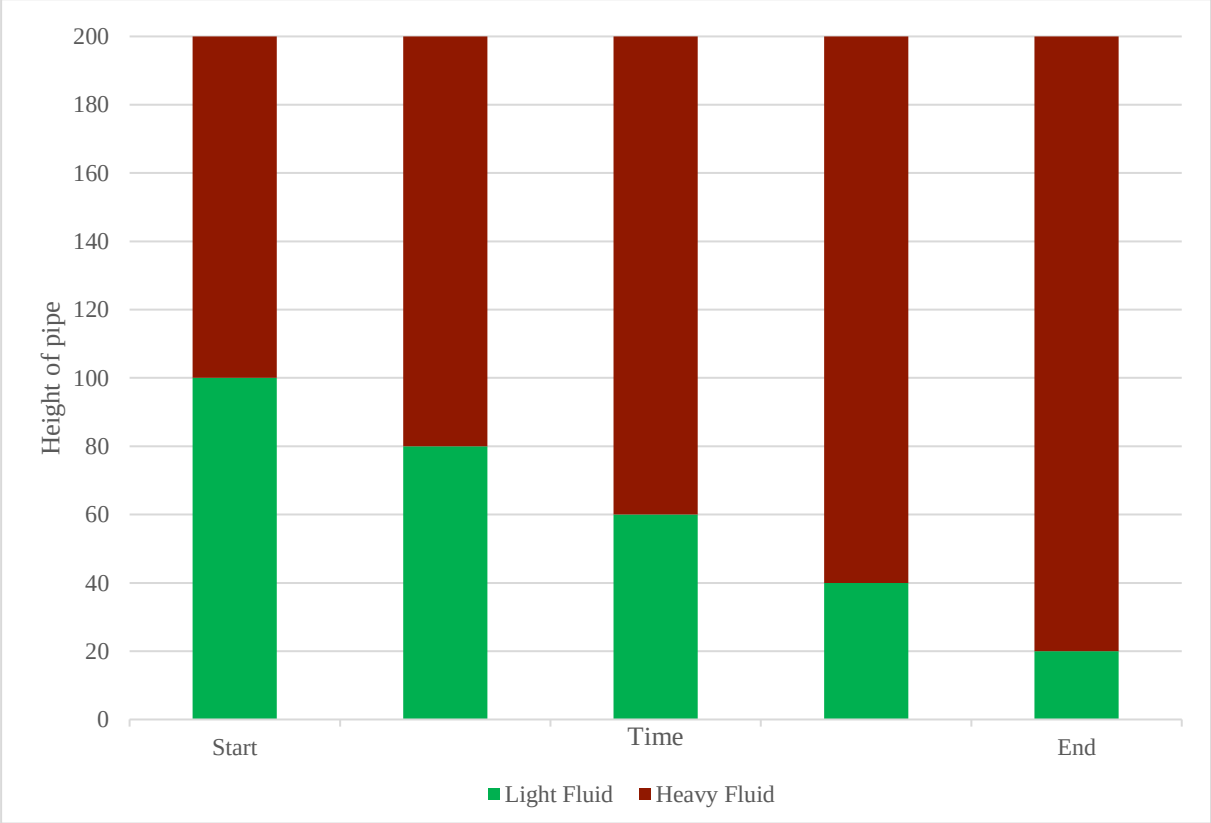

Figure 7.2 – Mixing zone development appearance

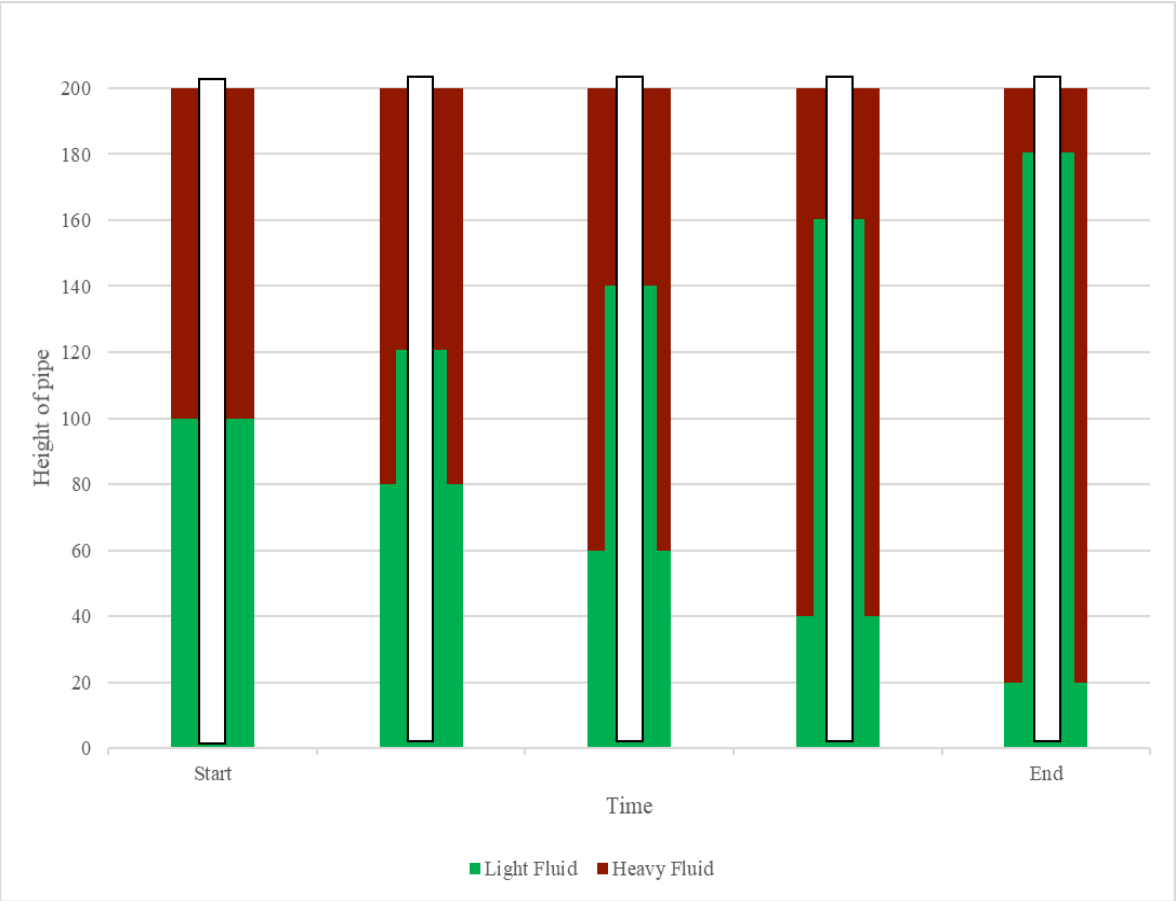

Figure 7.3 – Assumed actual mixing zone development

To investigate this properly in the future, the following experimental methods are suggested:

- Experiments with transparent fluids
- Experimental equipment with the possibility to collect density samples along the pipe during mixing
- Experimental equipment with pressure sensors along the pipe logging the pressure development.

7.2 EFFECT OF DRILLING FLUID PROPERTIES

According to the theory presented in section 3.2, the fluid with the higher density should be forced downwards, but this thesis work showed that that the mixing zone is relatively short and stable for all experiments with $\Delta\rho < 0.120$ sg. This value is suggested as a critical value for the difference in density where one can control the mixing zone below this value, but not for $\Delta\rho$ higher than this value. In this thesis work, this theory is only tested with diameters up to 31.5 mm and needs to be tested further with higher diameters to be verified.

One can also use multivariate modelling regression coefficients to investigate which parameters that increases with increasing mixing zone and which parameters that decreases with increasing mixing zone. Positive coefficients connected to the different parameters describe an increase with increasing mixing zone length. Negative coefficient shows that the related parameter decreases with the mixing zone. This is shown for example #2 in table 7.1, where all the well sizes are compared. For the summary column, a conclusion is made only if two or more of the individual well sizes parameters are consistent and the last well size doesn't show inconsistency with the two others.

Table 7.1 - Increasing and decreasing parameters from multivariate example #2

	Example #2			**Summary**
	19.3 mm well	31.5 mm well	40 mm well	
PV_{light}	Increases	Increases		**Increases**
$LSYS_{light}$		Decreases	Decreases	**Decreases**
n_{light}		Increases	Decreases	
$\theta_{3,light}$	Increases	Increases		**Increases**
ρ_{heavy}		Increases		
PV_{heavy}		Decreases	Increases	
$LSYS_{heavy}$	Decreases			
n_{heavy}	Increases	Increases		**Increases**
$\theta_{3,heavy}$	Decreases	Increases	Decreases	
$\Delta\rho$	Decreases	Decreases		**Decreases**
ΔPV	Increases			
$\Delta LSYS$	Increases	Decreases		

As can be seen from table 7.1, the parameter coefficients vary from well size to well size and it is therefore difficult to make a general conclusion. For the application of the models, it is important to analyze the mixing stability of formulated fluids according to the well size from which the model have been generated.

The plastic viscosity describes the resistance to flow and the higher PV, the higher the resistance to flow. So, one would think that with high values of PV, the mixing zone would be shorter and more stable. The results from these experiments doesn't show trends that match this theory. This is also consistent with the results from A. M. Haaland's master thesis [T17] where the conclusion from data (COMSOL) simulations was that the viscosity has little or no effect on the HOL mixing zone. The modelling approach in COMSOL was based on mass transfer at fluid – fluid interface analogy and the result might be qualitatively describing the mixing behavior for the difference in viscosity.

Banerjee et al. (2011) have also studied the effect of viscosity and surface tension on the Rayleigh-Taylor instability. According to the authors, the bubble height at the mix interface depends only on the magnitude of the viscous coefficient of the upper (denser) fluid [T28].

The yield point is also a part of the flow resistance, and according to theory, one would assume that with high yield points the results would show low and stable mixing zones. It is presented in section 5.5 that the LSYS of the light fluid decreases with increasing mixing zone, just as one would assume. Table 7.1 also conclude that **the LSYS of the light fluid decreases with increasing mixing zone**. The larger the $LSYS_{light}$ is, the shorter is the mixing zone. The HOL data simulations performed by A. M. Haaland in 2016 did also prove that high LSYS led to a stable HOL interface [T17]. This can also be compared to the suspension of particles during drilling operation. Sagging management control issues were analyzed by Scott et al. (2004). In this paper, it was indicated that insufficient LSYS is the main cause for sagging and the most effective method to reduce tendencies of sag is to increase the LSYS of the fluid to obtain desired range [T27].

The flow coefficient, *n*, of the Hershel Bulkley fluid model for the heavy fluid increases with increasing mixing zone, as shown in table 7.1. The graphs in section 5.6 states that the product of the *n*-values for the two HOL fluid increases with increasing mixing zone. *n* suggest the deviation from a Newtonian fluid (for Newtonian fluids, $n = 1$). The more shear thinning the fluids are, the lower are the value of *n*.

7.3 EFFECT OF EXPERIMENTAL WELL GEOMETRI

Multivariate modelling regression (Table 6.5 and Table 6.7) shows that **the clearance decreases with increasing mixing zone** for the 19.3 and 31.5 mm wells. This is consistent with the observations from section 5.4 and the theory presented below.

When looking at equation (3.6), $\gamma = \frac{\omega r_{DP}}{r_w - r_{DP}}$, $(r_w - r_{DP})$ represents the clearance. I.e. the higher the clearance, the lower the shear rate. According to equation (3.17), $\mu = \frac{\tau}{\dot{\gamma}}$, the viscosity is increasing with lower shear rate. As explained in previous sections, according to theory, one would assume that high viscosity leads to more stable and shorter mixing zones.

Hence, the theory states that:

High clearance = lower shear rate = higher viscosity = more stable mixing zone

and for the opposite:

Low clearance = higher shear rate = lower viscosity = more unstable mixing zone

When investigating the effect of well sizes, one can also look at the theory of equation (3.6) and observe that with large diameters and low clearance, the shear rate would be high and hence, the mixing zone would be long and unstable.

8 CONCLUSIONS

By utilizing four different well sizes, several HOL interface experiments have been conducted to document the stability in the vertical well geometry. These experiments have been designed to study the effect of well diameter, rheological properties, viscoelastic properties and density of drilling fluids with respect to the fluid interface mixing behavior. In order to recognize the main controlling parameters for HOL stability, a correlation factor and multivariate based models were developed. Results from the studies are summarized as:

- When the clearance between the well and drill string increases, it was observed that the mixing zone length decreases.
- Based on the mixing zone length mapped with the change in density, a critical density limit was observed where difference in density less than 0.120 sg shows mixing zone stability.
- A critical limit was also observed based on the mixing zone length mapped with the change in plastic viscosity. This showed that with difference in plastic viscosity less than 3.5 cP, the mixing zone is short and stable.
- For the three higher well geometries, it was observed that the LSYS of the light fluid decreases with increasing mixing zone length.
- Since the rotational speed was not controlled, the effect of rotation for lower and higher RPM seems undifferentiated for the results. In theory, the higher RPM generates the higher shear strain and hence, the viscosity of the fluid will be reduced.
- In general, the interface stability is investigated by the combined effects of rheology, clearance, well size and operation parameters.
- The higher the viscosity, yield strength and gel strength of the heavy fluid along with the lower interface, density difference in general reduces the instability.
- Based on the viscoelasticity measurement and the HOL mixing stability, the ratio $(H_{G'} - L_{G'})/(H_{G''} - L_{G''})$ with critical value < 4 has shown a stable interface.
- The lower difference between the damping factors of HOL is most stable of the system.
- Based on the modelling, as the newly developed correlation factor increases, the stability of the mixing zone will be reduced.

- For application of multivariate modelling for analysis of HOL interface stability, it would be advisable to apply the model for respective well size from which experimental data have been performed.

9 RECOMMENDED FURTURE WORK

For further work, it would be preferable to perform a greater amount of experiments;

- With larger well sizes and longer well pipes. The highest ID to mixing zone ratio achieved in these experiments are 1:64 when full mixing of the 31.5 mm well occurred. If this value would be representative for an 8.5 in well, the mixing zone length would only be 13,82 meters which is highly acceptable for the HOL concept.
- Moreover, it would be interesting to conduct the experiments with oil-based drilling fluid and compare the mixing phenomenon with water-based drilling fluid
- Modified experimental rig with the possibility to collect density samples along the pipe during mixing.
- Modified experimental rig with pressure sensors along the pipe logging the pressure development during mixing.

10 REFERENCES

Citation style: IEEE

THEORY

[T01] Engineering ToolBox, Density, Specific Weight and Specific Gravity, 2003. Available at: https://www.engineeringtoolbox.com/density-specific-weight-gravity-d_290.html. Accessed on May 4th 2018.

[T02] Sam-marsh.staff.shef.ac.uk, *Newton's Laws*. Available: http://sammarsh.staff.shef.ac.uk/mas115/docs/week10lab.html. Accessed on: May 2nd, 2018

[T03] B. S. Aadnoy, E. Kaarstad, "Theory and Application of Buoyancy in Wells", presented at IADC/SPE Asia Pacific Drilling Technology Conference and Exhibition, Bangkok, Thailand, 13-15 November 2006.

[T04] B.S. Aadnoy, I. Cooper, S. Z. Miska, R. F. Mitchell, M. L. Payne, *Advanced Drilling and Well Technology*. Richardson, TX, USA: Society of Petroleum Engineers, 2009.

[T05] Oxford University Press, *Centripetal force*, 2009. Available: http://www.oxfordreference.com.ezproxy.uis.no/view/10.1093/acref/9780199233991.001.0001/acref-9780199233991-e-435?rskey=4YzINl&result=464. Accessed on: May 7th, 2018.

[T06] Y. A. Çengel, J. M. Cimbala, *Fluid Mechanics: Fundamentals and Applications.* Second edition. New York: McGraw-Hill, 2014

[T07] S. Evje, K. K. Fjelde, "Hybrid Flux-Splitting Schemes for a Two-Phase Flow Model", Journal of Computational Physics, Vol.175(2), pp.674-701, Jan. 20th 2002. DOI: 10.1006/jcph.2001.6962

[T08] G. L. Asawa, *Laboratory work in hydraulic engineering*. India: New Age Internationals (P) Ltd. Publishers, 2006

[T09] *BIP 200: Øvinger i Bore- og Brønnvæsker*, laboratory booklet, University of Stavanger, 16th Jan. 2014

[T10] Y. Zhou, "Rayleigh–Taylor and Richtmyer–Meshkov instability induced flow, turbulence, and mixing. I*", Phys. Reports*, Vol.720-722, pp.1-136, Dec. 2017. doi: 10.1016/j.physrep.2017.07.005

[T11] Li, X. L., Jin, B. X., Glimm, J., *Numerical Study for the Three-Dimensional Rayleigh-Taylor Instability through the TVD/AC Scheme and Parallel Computation,* revised January 1996

[T12] M. López de Bertodano, W. Fullmer, A. Clausse, V. H. Ransom, *Two-Fluid Model Stability, Simulation and Chaos*. Web. Switzerland: Springer International Publishing, 2017.

[T13] O. Skjeggestad, *Boreslamteknologi: teori og praksis*. Bergen: Alma Mater, 1989.

[T14] MathWorks, *improfile - Pixel-value cross-sections along line segments,* 2018. Available: https://se.mathworks.com/help/images/ref/improfile.html. Accessed on: May 6th, 2018.

[T15] E. A. Vandvik, "Experimental investigation at heavy light interface mixture of Reelwell ERD", Master's Thesis, Faculty of Science and Technology, University of Stavanger, Stavanger, 2014.

[T16] M. Hurum, "Extended Reach Drilling using RDM – Heavy Over Light solution. Stability and control of the well annulus fluid", Master's Thesis, Faculty of Science and Technology, University of Stavanger, Stavanger, 2015.

[T17] A. M. Haaland, "Numerical Simulation and Experimental Study of Reelwell's Heavy over Light Solution in Vertical Well Sections", Master's Thesis, Faculty of Science and Technology, University of Stavanger, Stavanger, 2016.

[T18] G. Boffetta, A. Mazzino, S. Musacchio, *Gallery of Fluid Motion – Rotating Rayleigh-Taylor Turbulence*, 2015. Available: https://gfm.aps.org/meetings/dfd-2015/55f821ca69702d060dae0600. Accessed on: June 6th, 2018.

[T19] M-I Swaco Manual, *Drilling Fluids Engineering Manual, Polymer chemistry and Applications*, M-I Swaco, 1998

[T20] M. A. Ochoa, "Analysis of drilling fluid rheology and tool joint effect to reduce errors in hydraulics calculations", PhD Dissertation, Texas A&M University, 2006.

[T21] S. Weisberg, *Applied Linear Regression*, 3rd edition. New Jersey: Wiley, 2005.

[T22] Kremer Pigmentes, "44200 - Chrome Oxide Green," Material Safety Data Sheet, 2006 [Revised March 2010]

[T23] Kremer Pigments, "48120 - Iron Oxide Red 120 M," Material Safety Data Sheet, 2006 [Revised March 2010]

[T24] Rosneft, *The world's longest well was drilled in Sakhalin*, 2017. Available: https://www.rosneft.com/press/news/item/188679/. Accessed on: June 11th, 2018

[T25] T.G. Mezger, *The rheology handbook: for users of rotational and oscillatory rheometers*, Hannover: Vincentz, 2006.

[T26] B. Bui et al., *Viscoelastic properties of oil-based drilling fluids*, Annual Transactions of the Nordic Rheology Society, 2012.

[T27] P.D. Scott, M. Zamora, "Barite-Sag Management: Challenges, Strategies, Opportunities", presented at IADC/SPE Drilling Conference, 2 - 4 March, Dallas, Texas 2004, SPE-87136-MS

[T28] R. Banerjee, L. Mandal, S. Roy, M. Khan, M. R. Guptam, "Combined effect of viscosity and vorticity on single mode Rayleigh–Taylor instability bubble growth", Physics of Plasmas, Vol.18(2), Feb. 2011, doi: 10.1063/1.3555523

[T29] Flowsquare, *Flowsquare*, 2018. Available: http://flowsquare.com/. Accessed on: June 13th, 2018

REELWELL

[R1] Reelwell, *Reelwell Drilling Method*, 2018. Available: https://www.reelwell.com/rdm. Accessed on: Jan. 4th, 2018

[R2] O. Vestavik, S. Kerr, S. Brown, ‘’Reelwell Drilling Method’’, presented at SPE/IADC Drilling Conference and Exhibition, Amsterdam, Netherlands, 17 – 19 March 2009, SPE/IADC 119491

[R3] O. Vestavik, M. Egorenkov, B. Schmalhorst, J. Falcao, ‘’Extended Reach Drilling – new solution with a unique potential”, presented at SPE/IADC Drilling Conference and Exhibition, Amsterdam, Netherlands, 5 – 7 March 2013, SPE/IADC 163463

[R4] O. Vestavik, J. Thorogood, E. Bourdelet, B. Shcmalhorst, J. P. Roed, “Horizontal Drilling with Dual Channel Drill Pipe”, presented at SPE/IADC Drilling Conference and Exhibition, The Hauge, Netherlands, 14 – 16 March 2017, SPE/IADD-184683-MS

[R5] O. Vestavik, H. Syse, O. Hole, J. Aleksandersen, “New Approach to Improve the Horizontal Drilling Reach”, presented at Canadian Unconventional Resources and International Petroleum Conference, Calgary, Alberta, Canada, 19 – 21 October 2010, SPE-137821-MS

FIGURES

[F01] K. Sonowal, B. Bennetzen, P. Wong, E. Isevcan, “How Continuous Improvement Lead to the Longest Horizontal Well in the World”, presented at SPE/IADC Drilling Conference and Exhibition, Amsterdam, Netherlands, 17 – 19 March 2009, SPE/IADC 119506

[F02] O. Vestavik, J. Thorogood, E. Bourdelet, B. Shcmalhorst, J. P. Roed, “Horizontal Drilling with Dual Channel Drill Pipe”, presented at SPE/IADC Drilling Conference and Exhibition, The Hauge, Netherlands, 14 – 16 March 2017, SPE/IADD-184683-MS

[F03] O. Vestavik, “Heavy Over Light verification for vertical wells”, unpublished.

[F04] Linn Engan Karlsen, Drawn Figures/Illustrations

[F05] Linn Engan Karlsen, Personal Pictures

[F06] M. Belayneh, *Advanced Well and drilling engineering compendium*, University of Stavanger, 2018

[F07] A. T. Veisene, "Well Control during Extended Reach Drilling – conventional drilling compared to the Reelwell Drilling Method," Master thesis, Faculty of Science and Technology, University of Stavanger, Stavanger, 2014

[F08] Wikipedia, *Stokes Law*, 2018. Available: https://en.wikipedia.org/wiki/Stokes%27s_law. Accessed on: June 13th, 2018

APPENDIX

APPENDIX A – WORK PROCEDURES

RHEOLOGY MEASUREMENTS

To measure the rheology of the drilling fluids the Fann viscometer was used. See figure A1. The Fann viscometer measures the relationship between shear stress and shear rate. The mud is placed in the container and the container is placed so that a part of the rheometer is lowered into the fluid. The fluid should fill the gap between the cylinder which is suspended in a torsion spring and the rotating sleeve. When the sleeve rotates, the closest fluid layer will also rotate with approximately the same speed as the sleeve. The fluid layers within will rotate more slowly and the innermost layer closest to the cylinder will transfer a torque to the cylinder. The torsion spring works as a counterforce, but when this is overcome, the cylinder rotates. The size of the rotation is read from the scale on top of the viscometer and this gives a measurement on the shear stress.

Figure A 1 – Viscometer [F05]

Measurements are done with readings for 600 rpm, 300 rpm, 200 rpm, 100 rpm, 60 rpm, 30 rpm, 6 rpm and 3 rpm. Viscosity is then calculated from equations described in section 3.8 [T13]. For yield point determination, the Herschel Bulkley model was used.

GEL STRENGTH DETERMINATION

The gel strength expresses the mud's ability to stiffen as the fluid remains quiescent. Gel strength is associated with attraction forces between the particles in the mud when the mud is at rest. Gel strength is measured by stirring the mud at high rate (600 rpm) in the viscometer for 10 seconds. The mud is then at rest in 10 seconds and the maximum reading is measured at 3 rpm. Then the mud is stirred again at 600 rpm in 10 seconds and then put to rest in 10 minutes. Then the maximum reading is measured at 3 rpm. The gel strength is reported as maximum reading after 10 seconds / maximum reading after 10 minutes [T09].

DENSITY DETERMINATION

The density is measured by using a bariod mud balancer (figure A2). The cup on one of the ends is completely filled with mud. The lid, which has a hole in the middle, is placed with a rotational motion on the cup so that the excessive mud is pressed out through the hole. The container is then wiped and dried before the balance arm is placed on the base, with the knife edge resting on the fulcrum. The rider along the balancing arm is moved until the arm is horizontal, indicated by the level vial on the beam. Then the density is read from the placement of the rider. The unit used is p.p.g. [T13].

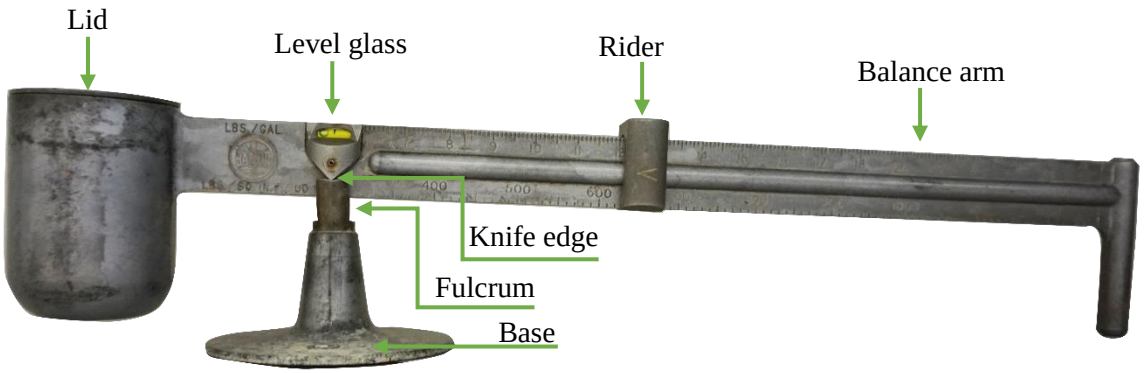

Figure A 2 - Baroid mud balancer [F05]

RPM MEASUREMENTS

RPM is measured simply by counting rounds when taking the time. Because the RPM of the electric drill is very unstable, it is not possible to obtain a constant RPM for the experiments. The RPM reported is therefore highly variable.

APPENDIX B – EQUIPMENT

Table A. 1 - Laboratory safety equipment

Laboratory safety equipment		
Nr.	**Name**	**Purpose**
S1	Laboratory coat	Protects body and clothes.
S2	Safety glasses	Eye protection.
S3	Disposable latex gloves	Protects skin.

Table A. 2 - Measuring equipment

Measuring equipment		
Nr.	**Name**	**Purpose**
M1	Measuring tape	Measure mixing zone.
M2	Vernier caliper	Measure ID and OD of pipes and poles.
M3	Laboratory scale	Weighing of small amounts of ingredients or components used for drilling fluids.
M4	Disposable syringe	Used for accurate measurements of small amounts of fluids.
M5	Mud balance	Used to measure density of a drilling fluid.
M6	Fann viscometer	Used to measure viscosity and gel strength of a drilling fluid.
M7	pH meter	Measures the hydrogen-ion activity in a fluid, indicating the pH value.

Table A. 3 - Experimental equipment

Experimental equipment		
Nr.	**Name**	**Purpose**
E1	Plastic pipes	With several different IDs used to simulate a well bore. ID = 10 mm, 19.3 mm, 31.5 mm and 40 mm
E2	Curtain wire	Used to simulate a rotating drill string with OD = 6 mm
E3	Plastic poles	Used to simulate a rotating drill string with OD = 7.3 mm and 14.8 mm.

Experimental equipment		
E4	Metal poles	Used to simulate a rotating drill string with OD = 20.2 mm and 25.3 mm
E5	Electric drill	Used to rotate the drill string
E6	Jack stands	Used to support the plastic pipes in horizontal experiments.
E7	Duct tape	Used to restrain and secure objects
E8	Plastic strips	Used to restrain objects
E9	Sony α6000 Hybrid camera	Used to capture the mixing zone development
E10	Hama Star 700 EF Digital Camera stand	Used to place the camera in desired positions
E11	Light-blocking roller blinds	Used to create a light-constant environment for optimal photography during experiments
E12	Large stand	Used to fasten the light-blocking roller blinds
E13	2-meter-high stand	Used to hold the electric drill in place during experiments
E14	Plastic stopper	Used to seal the bottom of the 40 mm plastic pipe
E15	Measuring cups	Used to contain drilling fluid and to be able to pour the drilling fluid in a controlled manner
E16	Hei-TORQUE Value 100	Overhead stirrer used to disperse the drilling fluid substances and mix the drilling fluid during preparation
E17	Plastic funnel	Used to channel drilling fluid into containers with a small opening
E18	Plastic hose	Used to transport the drilling fluid to the bottom of the plastic pipes to prevent spilling of fluid on the inner walls of the plastic pipe.

APPENDIX C – DIRECTLY READ LABORATORY VALUES, RHEOLOGY PLOTS AND RESULTS

This appendix presents all the directly ready laboratory values from the viscometer and the density read from the baroid mud balancer. Underneath all the tables there will be two graphs; one showing the Herschel Bulkley model for each drilling fluid and one representing the result from each experiment.

For all graphs: The explanation for the curves represent the ID of the pipe unless otherwise is stated.

Table A. 4 - Directly read laboratory values for experiment 03/01 - 1

EXPERIMENT 03/01 - 1		
Viscometer readings	Light fluid	Heavy Fluid
θ_{600}	14,5	40
θ_{300}	9	30,5
θ_{200}	7,5	26
θ_{100}	5	20
θ_{60}	4	18
θ_{30}	3	16
θ_{6}	2	13
θ_{3}	1,5	12,5
Gel strength [10 sec / 10 min]	2/10	15/25
Density [ppg]	8,5	9,95

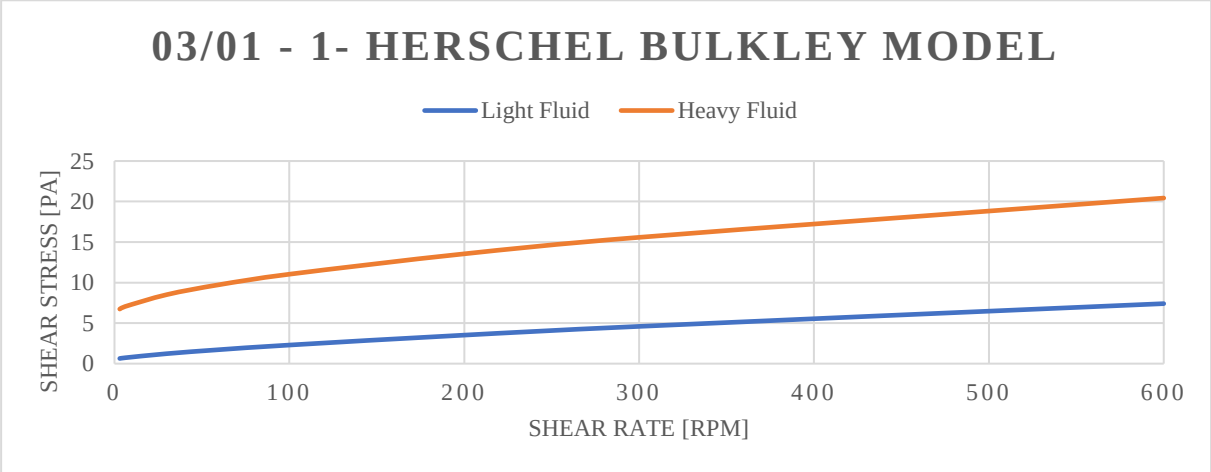

Figure A 3 - Herschel Bulkley Model for experiment 03/01 – 1

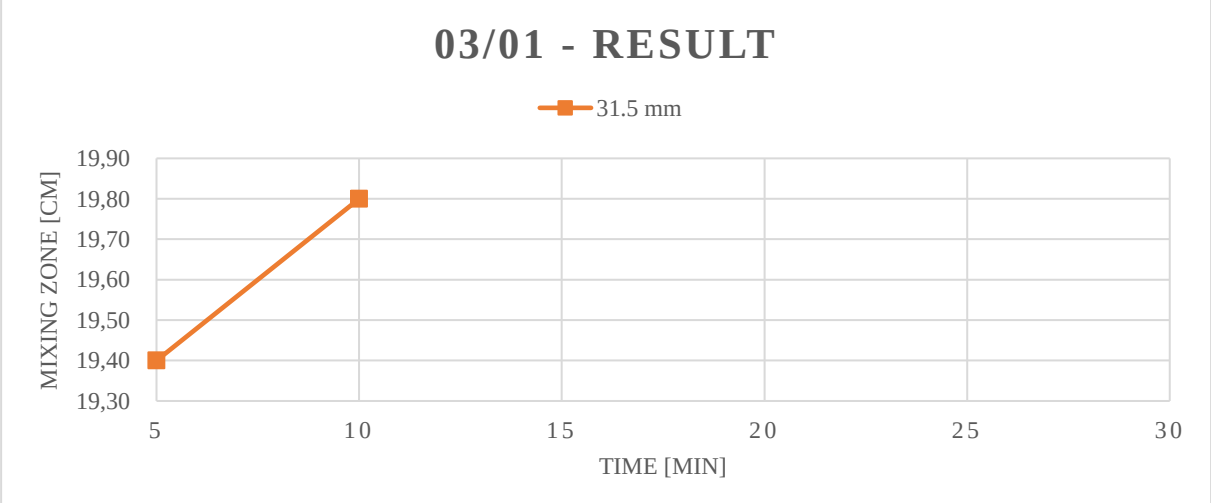

Figure A 4 - Results for experiment 03/01

Table A. 5- Directly read laboratory values for experiment 03/19 - 1

EXPERIMENT 03/19 - 1		
Viscometer readings	Light fluid	Heavy Fluid
θ_{600}	32,5	46
θ_{300}	25	35,5
θ_{200}	21,5	31
θ_{100}	17	25
θ_{60}	15,5	22,5
θ_{30}	14	21
θ_{6}	11	18
θ_{3}	11	17
Gel strength [10 sec / 10 min]	14/28	21/31
Density [ppg]	9,2	10,1

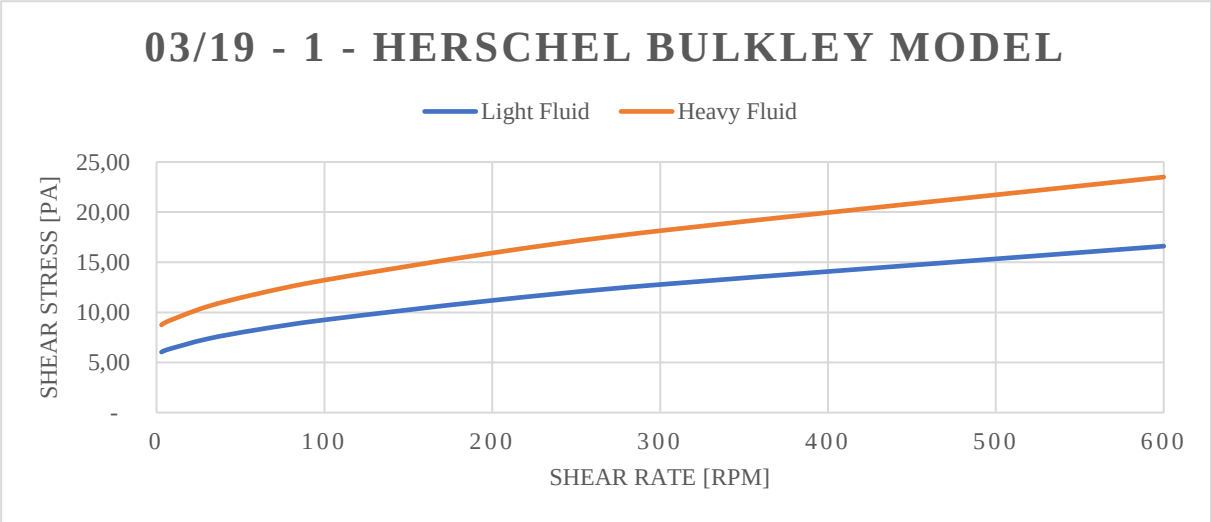

Figure A 5 - Herschel Bulkley Model for experiment 03/13 – 1

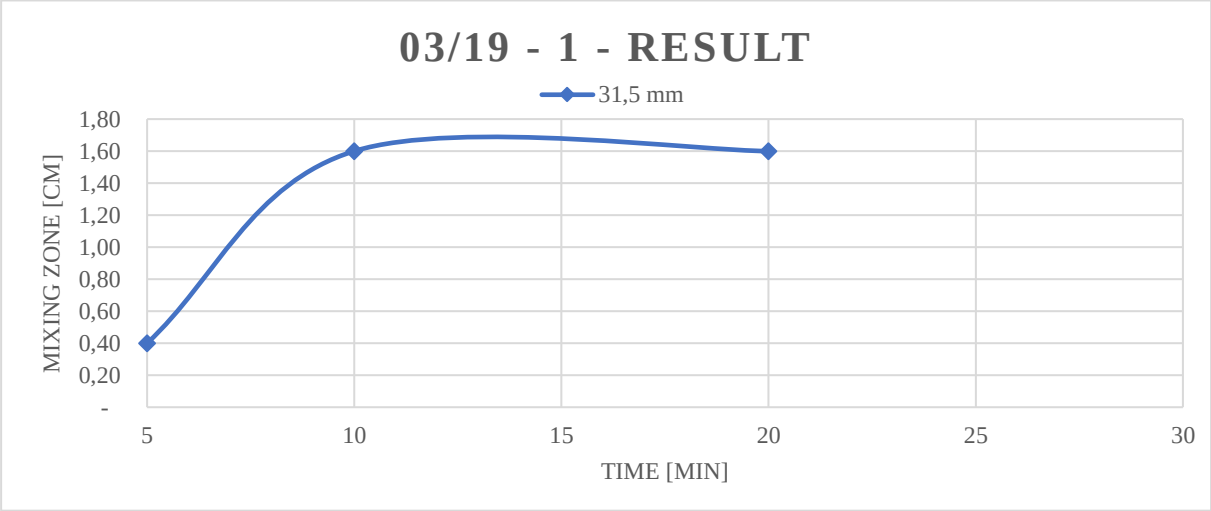

Figure A 6 - Results for experiment 03/19 - 1

Table A. 6 - Directly read laboratory values for experiment 03/19 - 2

EXPERIMENT 03/19 –2		
Viscometer readings	Light fluid	Heavy Fluid
θ_{600}	31	44
θ_{300}	23	32
θ_{200}	19.5	26.5
θ_{100}	15	20
θ_{60}	13.5	18
θ_{30}	12	15
θ_{6}	10	13
θ_{3}	9	13
Gel strength [10 sec / 10 min]	-	-
Density [ppg]	9.2	10.85

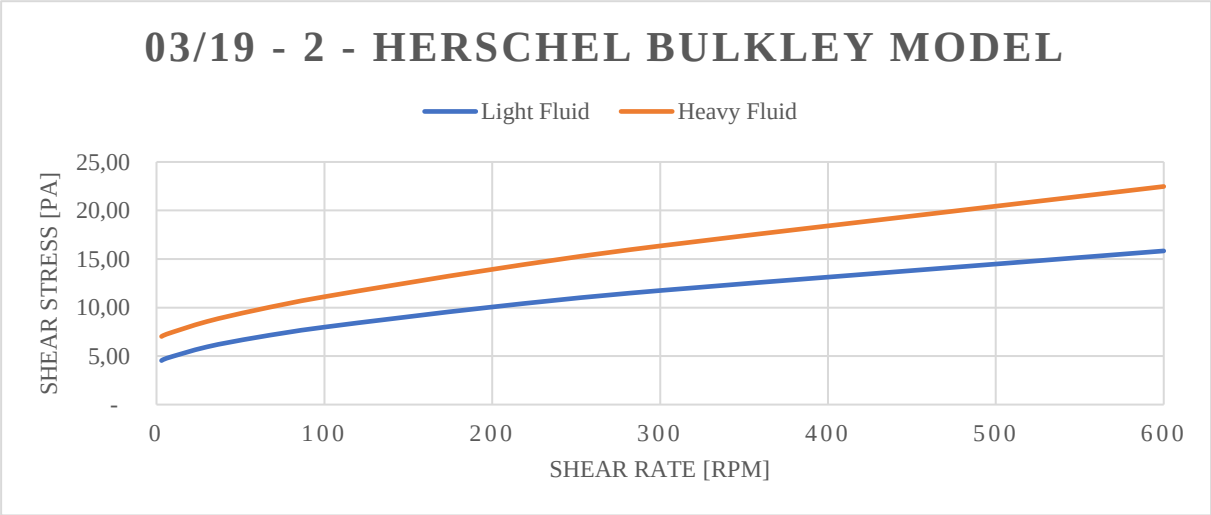

Figure A 7 - Herschel Bulkley Model for experiment 03/19 – 2

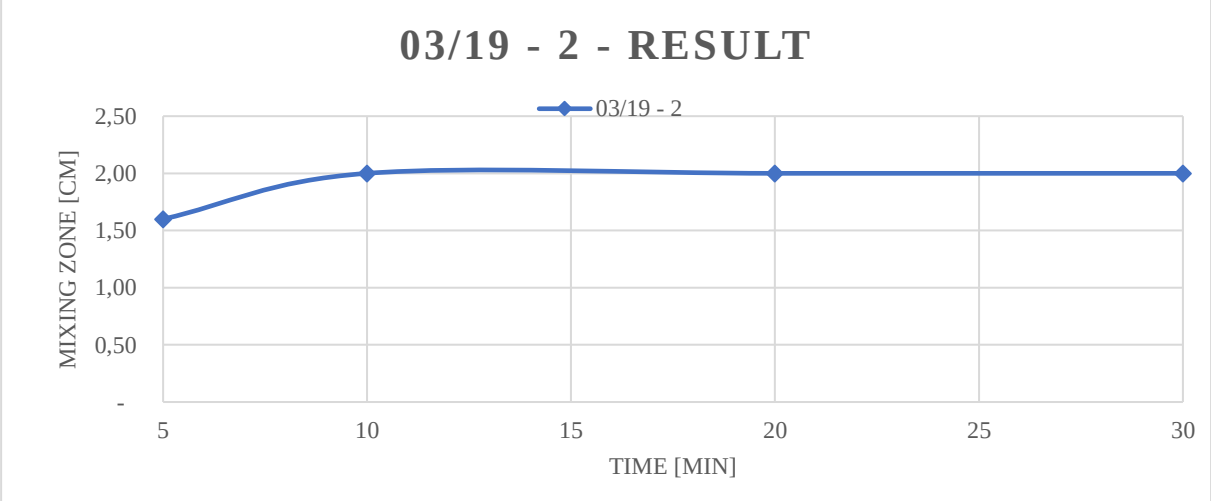

Figure A 8 - Results for experiment 03/19 - 2

Table A. 7 - Directly read laboratory values for experiment 03/21

EXPERIMENT 03/21		
Viscometer readings	Light fluid	Heavy Fluid
θ_{600}	23	39
θ_{300}	17,5	33
θ_{200}	15	30
θ_{100}	12	26
θ_{60}	10,5	24
θ_{30}	9	22
θ_{6}	7	19
θ_{3}	6,5	18,5
Gel strength [10 sec / 10 min]	7/13	20/32
Density [ppg]	8,5	9,35

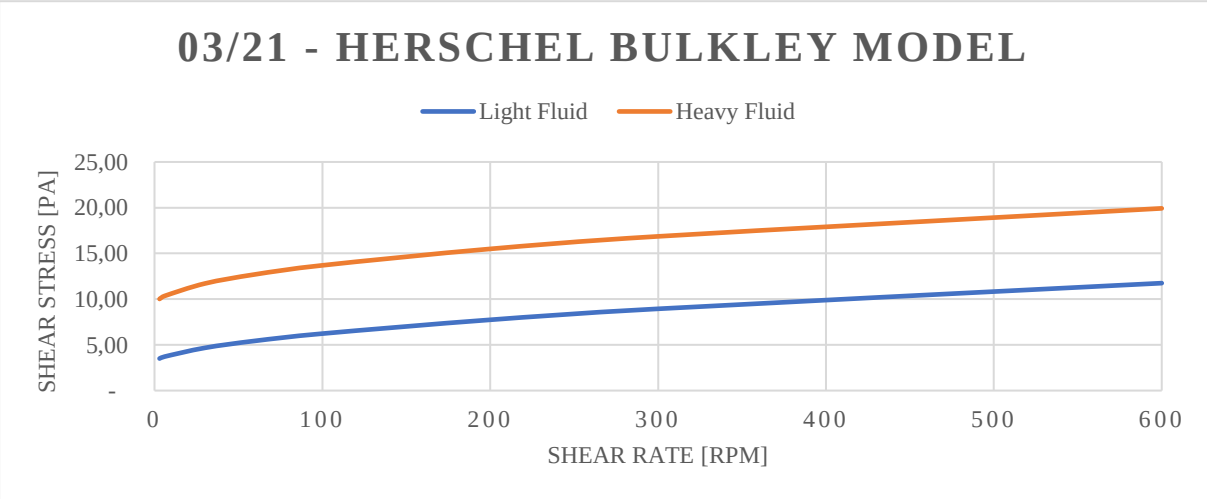

Figure A 9 - Herschel Bulkley Model for experiment 03/21

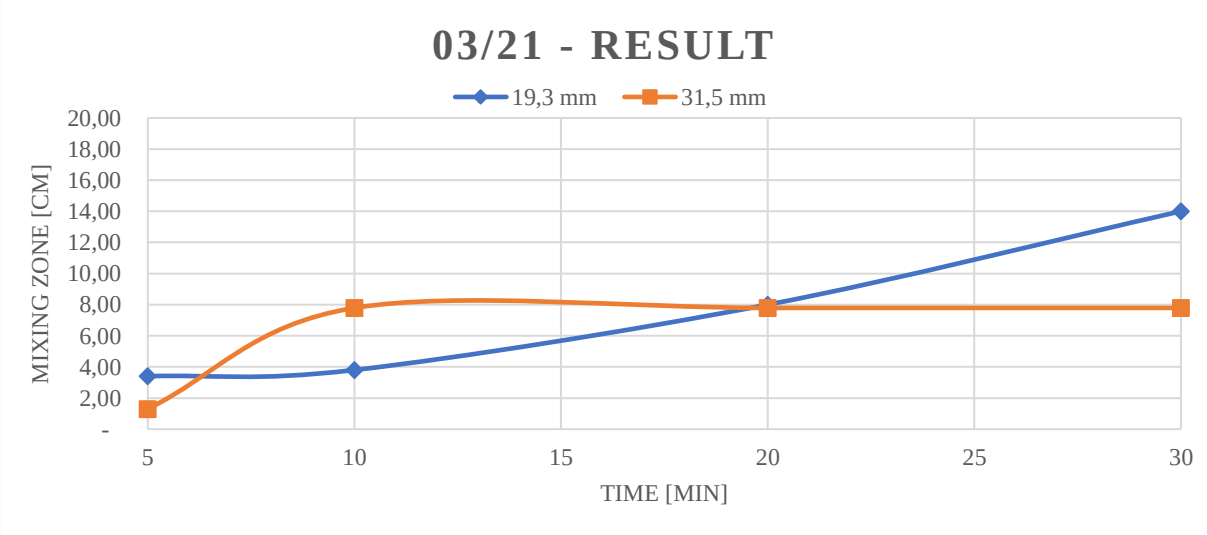

Figure A 10 - Results for experiment 03/21

Table A. 8 - Directly read laboratory values for experiment 03/23

EXPERIMENT 03/23		
Viscometer readings	Light fluid	Heavy Fluid
θ_{600}	26	45,5
θ_{300}	19,5	38
θ_{200}	17	35
θ_{100}	13,5	29
θ_{60}	11,5	27
θ_{30}	10	24
θ_{6}	7,5	20
θ_{3}	7,5	20
Gel strength [10 sec / 10 min]	-	-
Density [ppg]	8,5	9,3

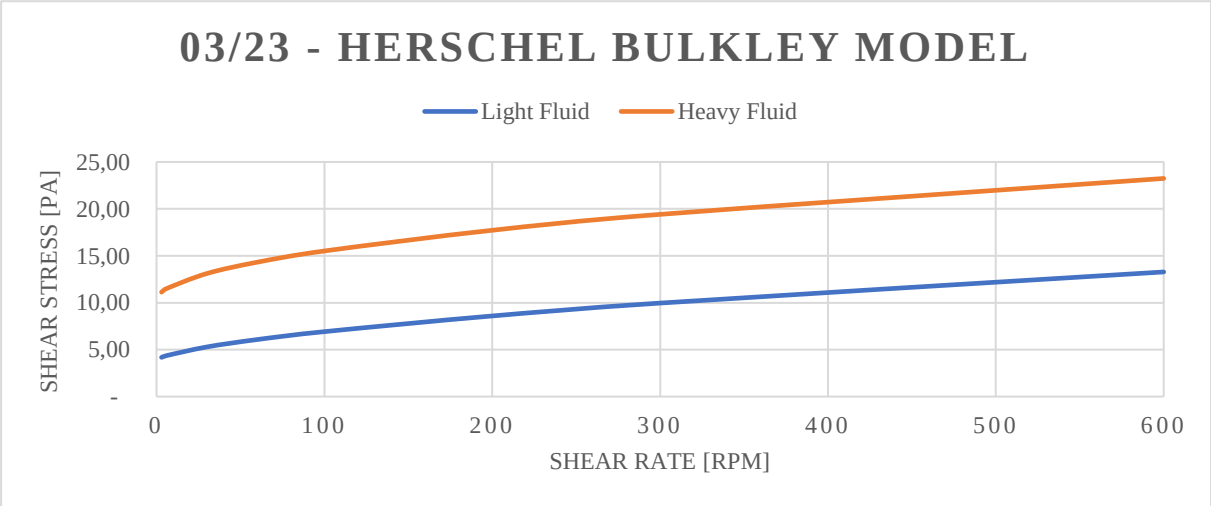

Figure A 11 - Herschel Bulkley Model for experiment 03/23

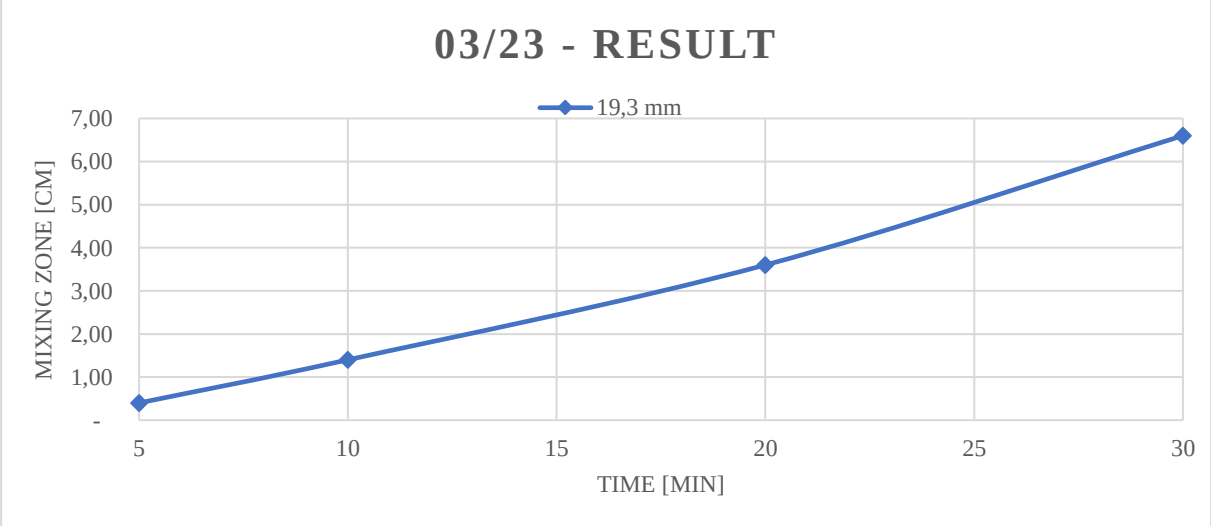

Figure A 12 - Results for experiment 03/23

Table A. 9 - Directly read laboratory values for experiment 04/04

EXPERIMENT 04/04		
Viscometer readings	Light fluid	Heavy Fluid
θ_{600}	16	27,5
θ_{300}	11,5	19
θ_{200}	9,5	15
θ_{100}	7	11,5
θ_{60}	6	10
θ_{30}	4,5	8,5
θ_{6}	3,5	7
θ_{3}	3,5	7
Gel strength [10 sec / 10 min]	5/14	10/24
Density [ppg]	8,5	9,45

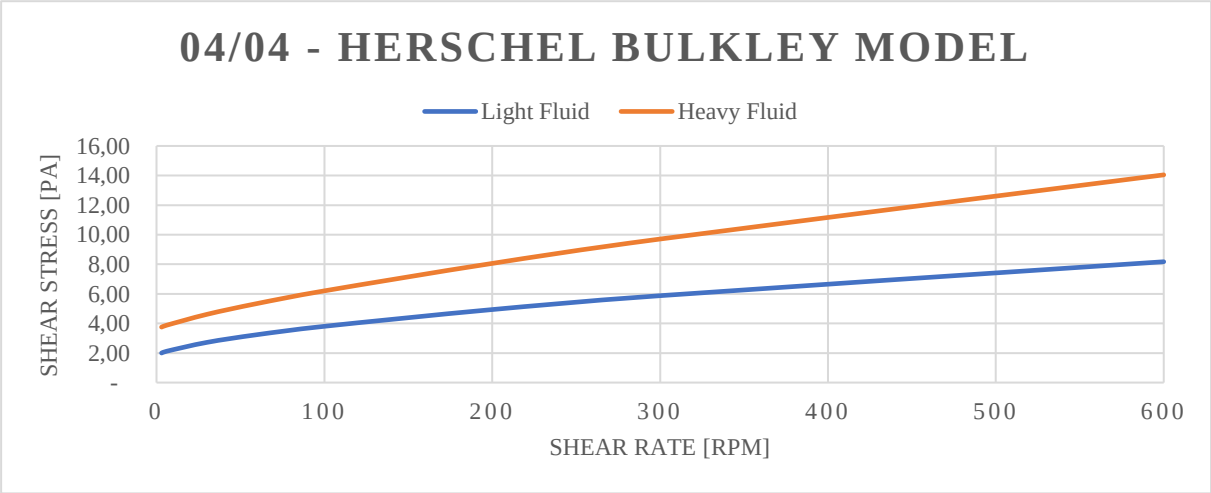

Figure A 13 - Herschel Bulkley Model for experiment 04/04

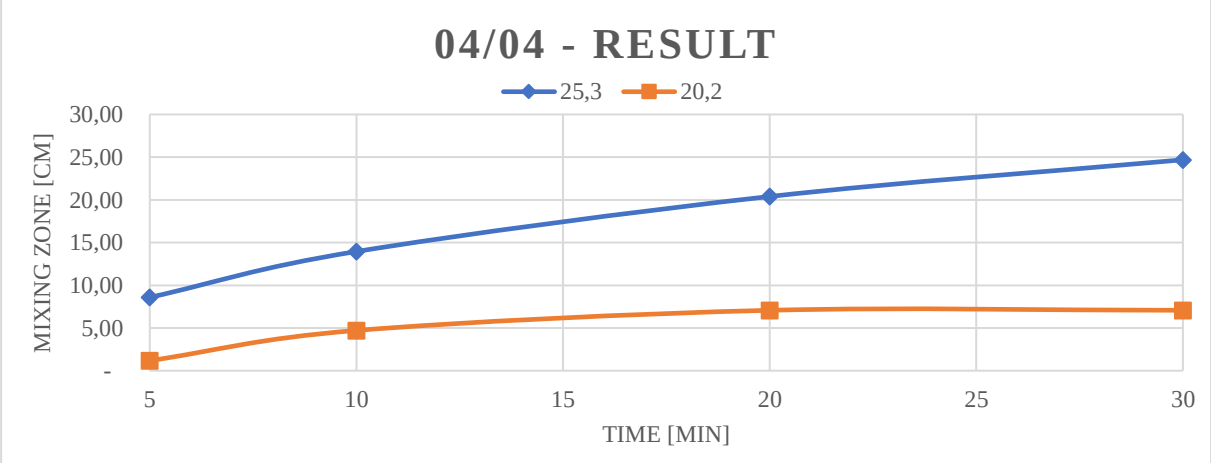

Figure A 14 - Results for experiment 04/04

Table A. 10 - Directly read laboratory values for experiment 04/11

EXPERIMENT 04/11		
Viscometer readings	Light fluid	Heavy Fluid
θ_{600}	24	39
θ_{300}	18	30,5
θ_{200}	15	27
θ_{100}	12	22
θ_{60}	10	19
θ_{30}	8,5	17
θ_{6}	6,5	14
θ_{3}	6,5	13,5
Gel strength [10 sec / 10 min]	-	-
Density [ppg]	8,6	9,3

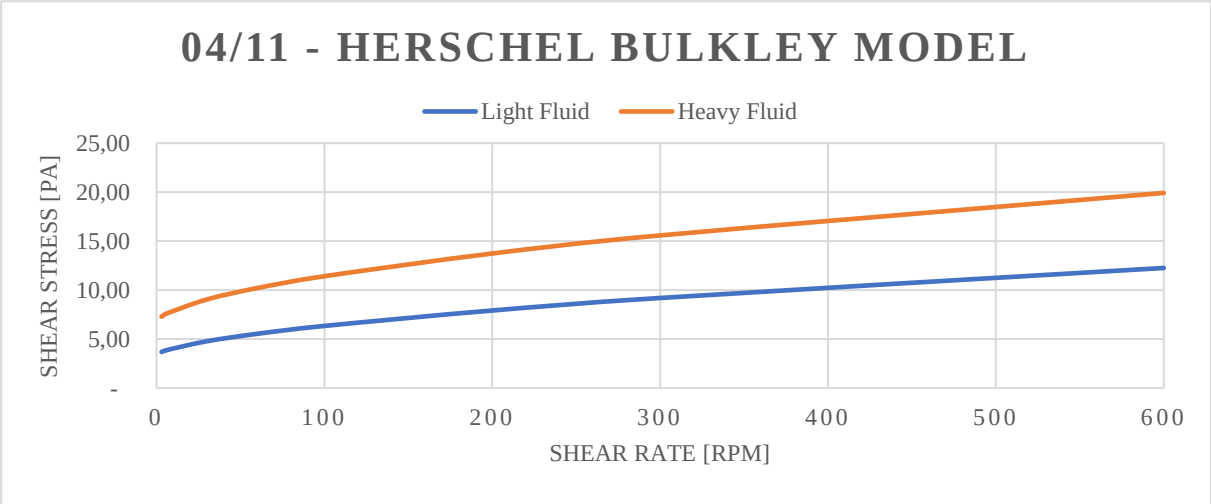

Figure A 15 - Herschel Bulkley Model for experiment 04/11

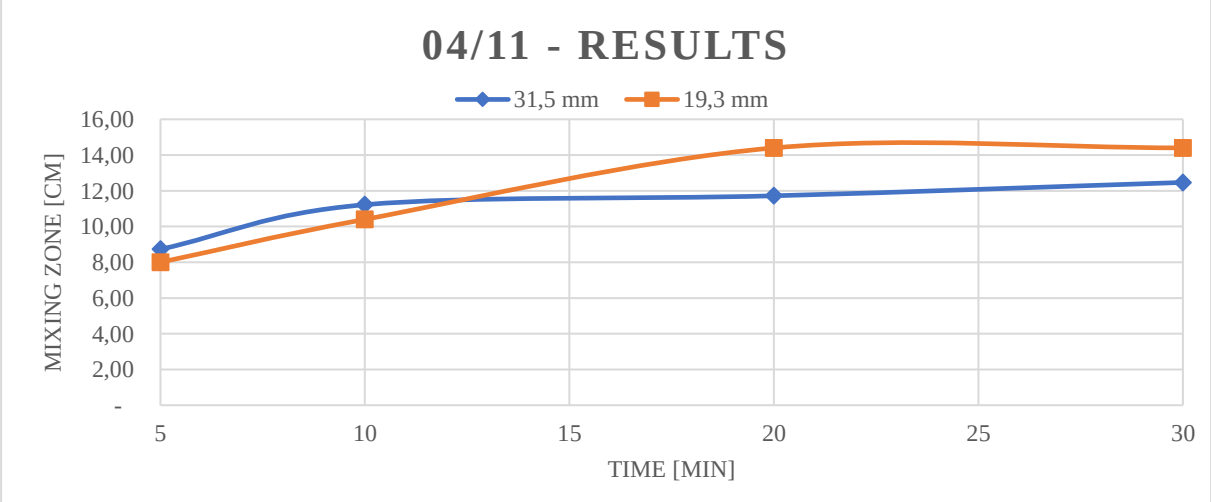

Figure A 16 - Results for experiment 04/11

Table A. 11 - Directly read laboratory values for experiment 04/12

EXPERIMENT 04/12		
Viscometer readings	Light fluid	Heavy Fluid
θ_{600}	13,5	30
θ_{300}	8	20,5
θ_{200}	6	17
θ_{100}	4	13
θ_{60}	3,5	11
θ_{30}	2	9
θ_{6}	1	7,5
θ_{3}	1	7,5
Gel strength [10 sec / 10 min]	1/1,5	11/20
Density [ppg]	8,55	9,7

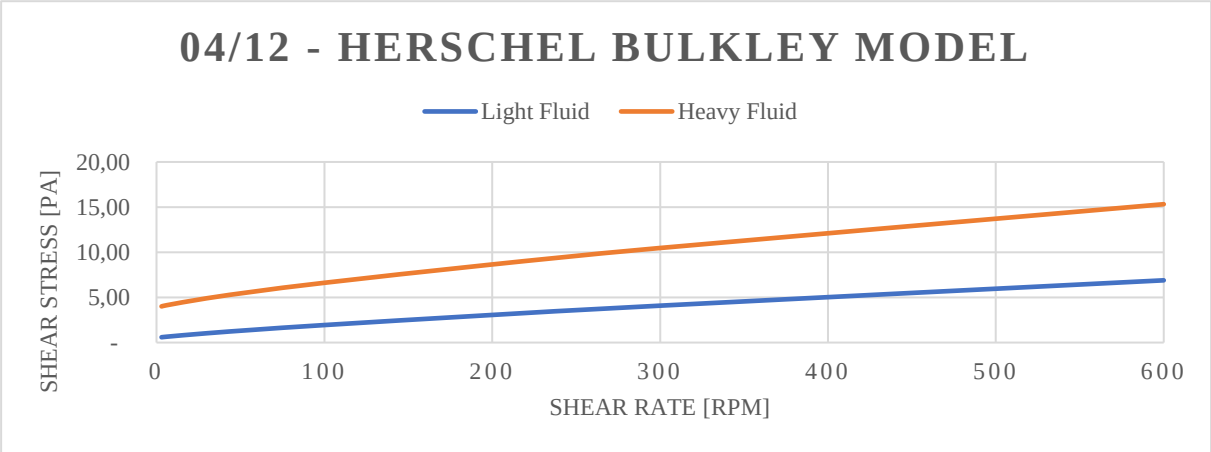

Figure A 17 - Herschel Bulkley Model for experiment 04/12

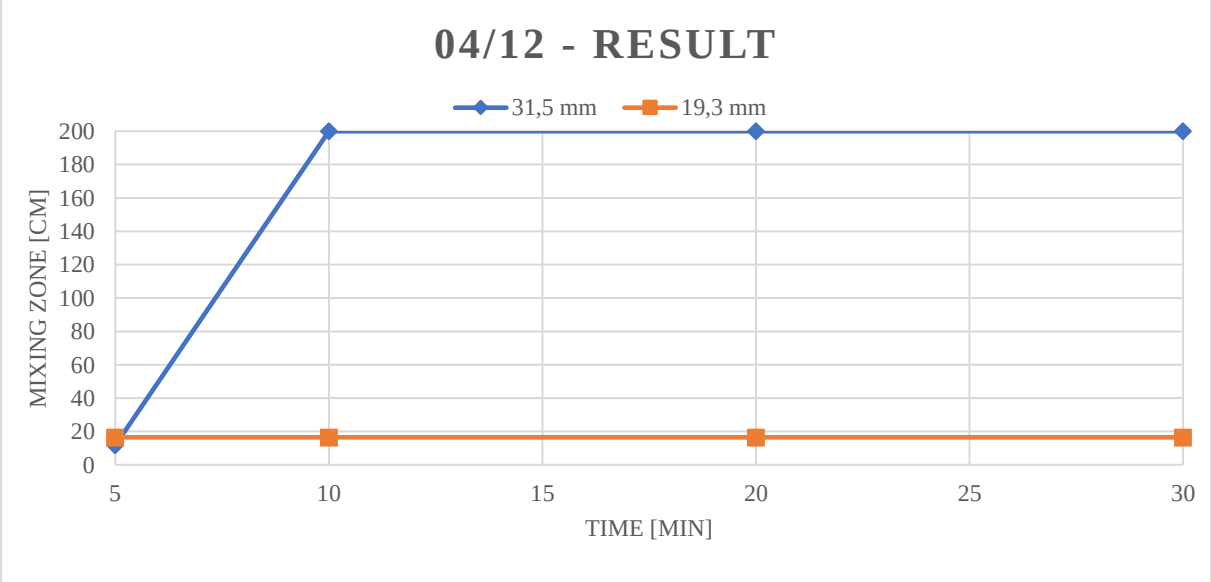

Figure A 18 - Results for experiment 04/12

Table A. 12 - Directly read laboratory values for experiment 04/13

EXPERIMENT 04/13		
Viscometer readings	Light fluid	Heavy Fluid
θ_{600}	18	37
θ_{300}	12	29
θ_{200}	9,5	24,5
θ_{100}	6,5	20
θ_{60}	5,5	18
θ_{30}	3	16
θ_{6}	2	13
θ_{3}	1,5	13
Gel strength [10 sec / 10 min]	2/13	12/92
Density [ppg]	8,5	9,7

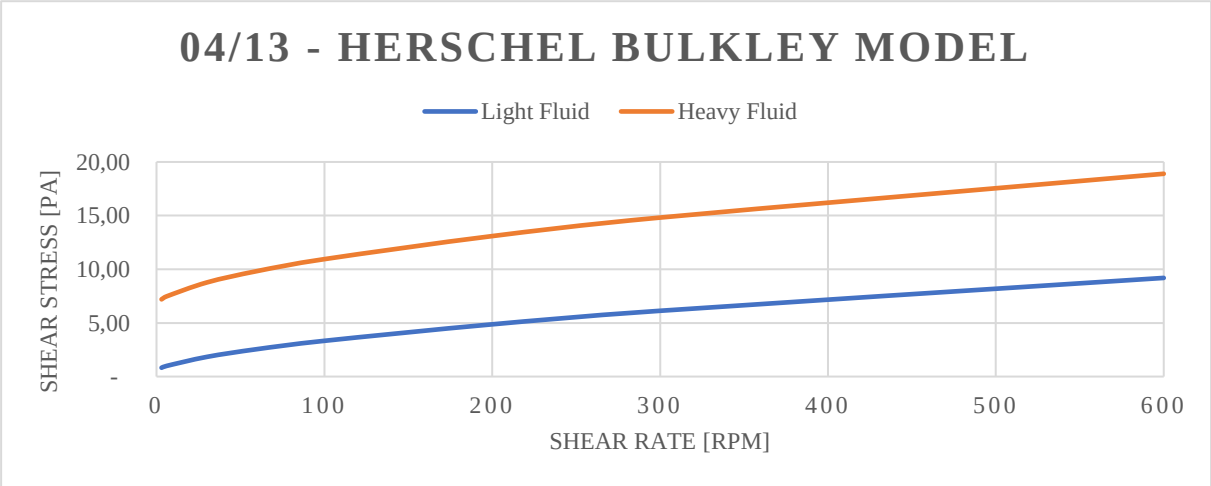

Figure A 19 - Herschel Bulkley Model for experiment 04/13

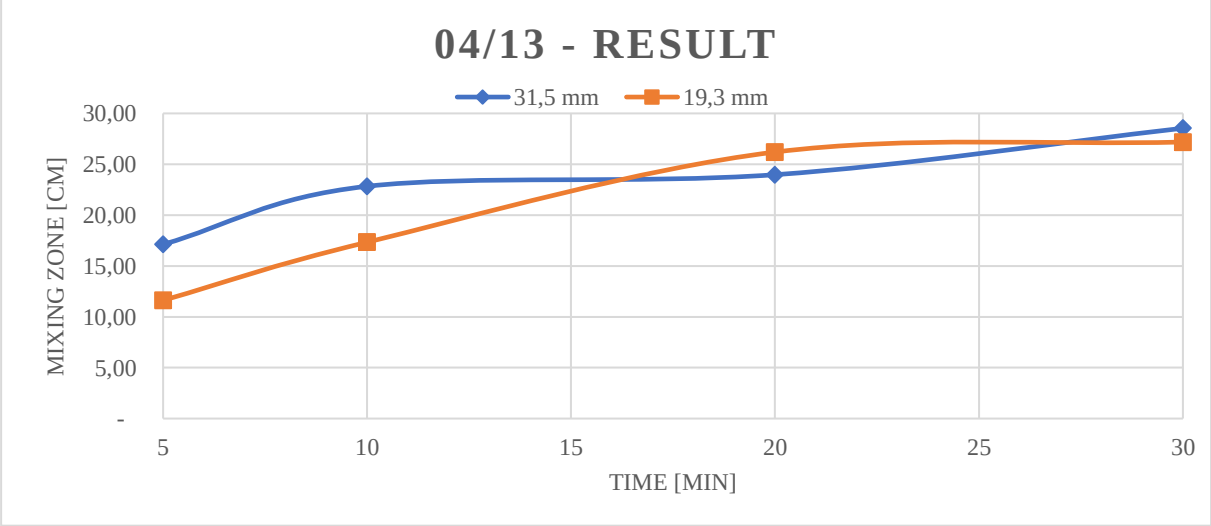

Figure A 20 - Results for experiment 04/13

Table A. 13 - Directly read laboratory values for experiment 04/15

EXPERIMENT 04/15		
Viscometer readings	Light fluid	Heavy Fluid
θ_{600}	14	37
θ_{300}	8,5	26
θ_{200}	6	23
θ_{100}	4	18
θ_{60}	3	16
θ_{30}	2,5	13,5
θ_{6}	1	11,5
θ_{3}	1	11,5
Gel strength [10 sec / 10 min]	1/5	15/25
Density [ppg]	8,6	9,7

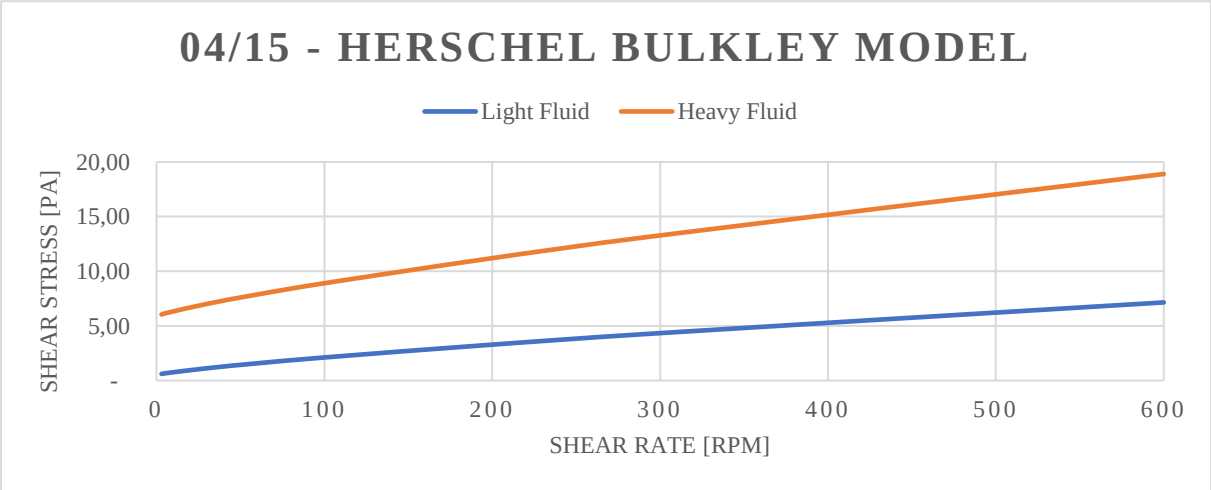

Figure A 21 - Herschel Bulkley Model for experiment 04/15

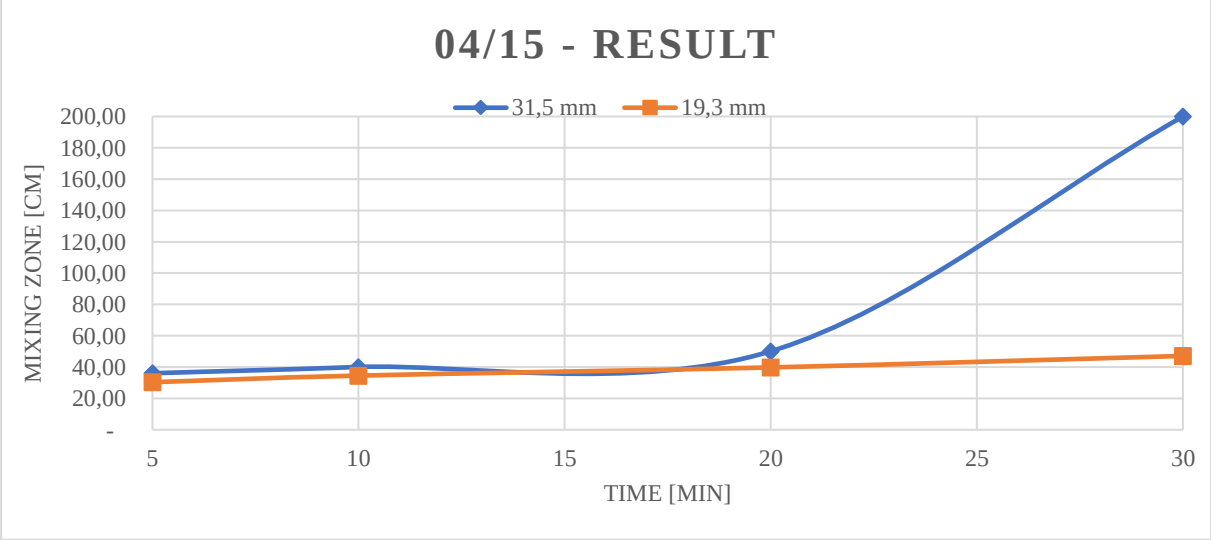

Figure A 22 - Results for experiment 04/15

Table A. 14 - Directly read laboratory values for experiment 04/17

EXPERIMENT 04/17		
Viscometer readings	Light fluid	Heavy Fluid
θ_{600}	19	49
θ_{300}	12	39
θ_{200}	9,5	34
θ_{100}	6,5	27,5
θ_{60}	4,5	25,5
θ_{30}	3,5	23
θ_{6}	1,5	19,5
θ_{3}	1,5	19,5
Gel strength [10 sec / 10 min]	1,5/11	21/32
Density [ppg]	8,55	9,7

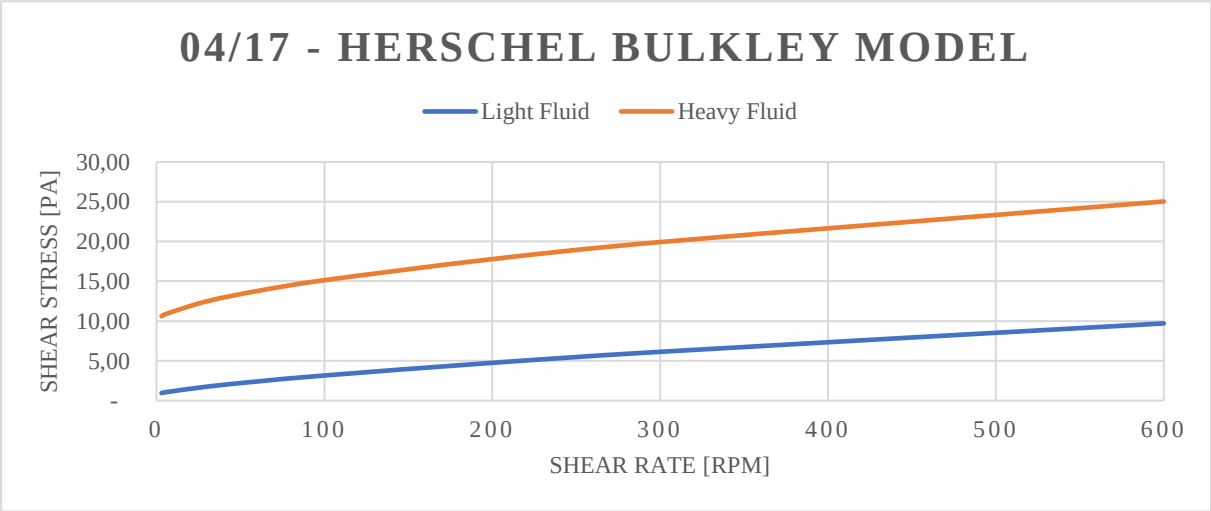

Figure A 23 - Herschel Bulkley Model for experiment 04/17

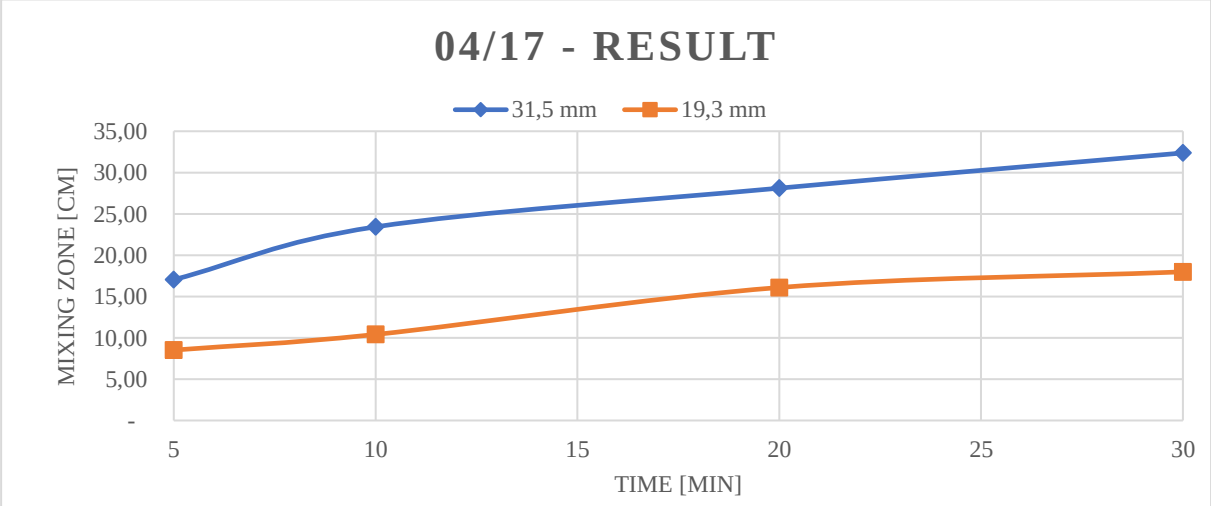

Figure A 24 - Results for experiment 04/17

Table A. 15 - Directly read laboratory values for experiment 04/19

EXPERIMENT 04/19		
Viscometer readings	Light fluid	Heavy Fluid
θ_{600}	25	46
θ_{300}	17	38,5
θ_{200}	14	34,5
θ_{100}	10	29
θ_{60}	8	27
θ_{30}	6	25
θ_{6}	3,5	20,5
θ_{3}	3,5	20,5
Gel strength [10 sec / 10 min]	5/16	23/35
Density [ppg]	8,6	9,45

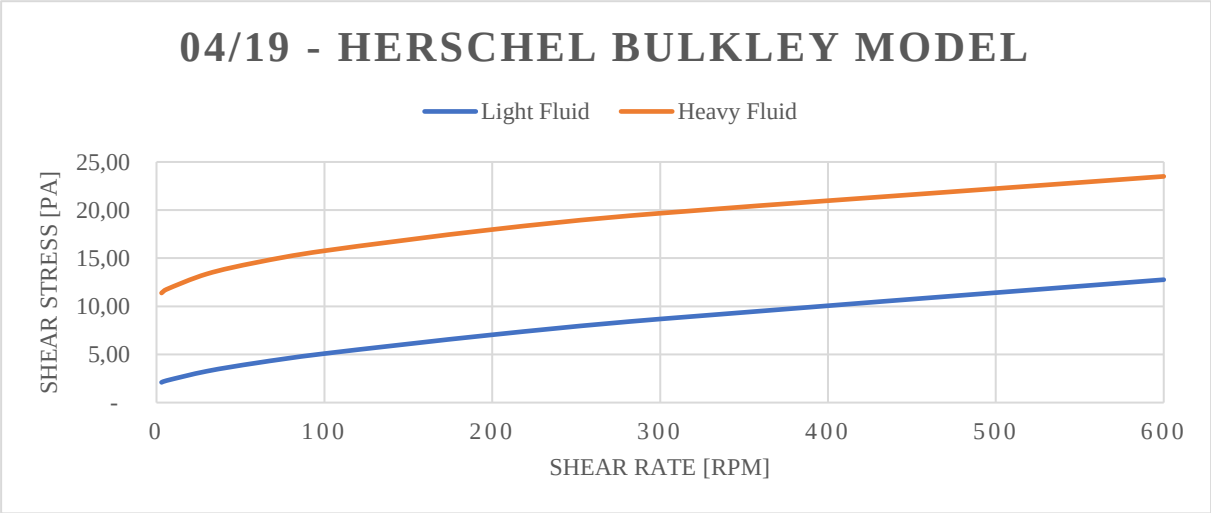

Figure A 25 - Herschel Bulkley Model for experiment 04/19

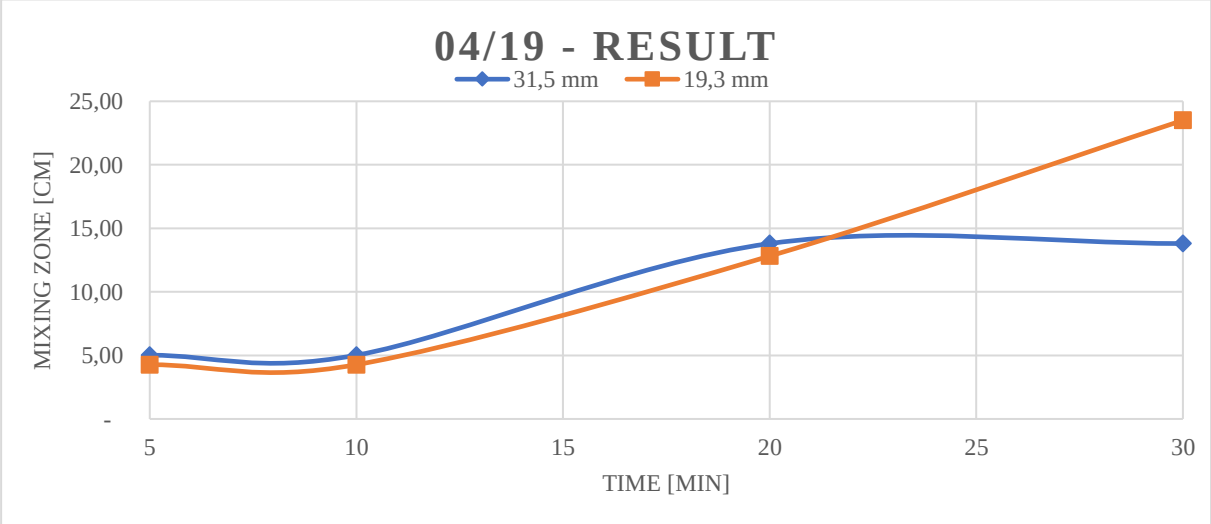

Figure A 26 - Results for experiment 04/19

Table A. 16 - Directly read laboratory values for experiment 04/23

EXPERIMENT 04/23		
Viscometer readings	Light fluid	Heavy Fluid
θ_{600}	17,5	26,5
θ_{300}	11,5	17
θ_{200}	9,5	13,5
θ_{100}	6	9,5
θ_{60}	5	8,5
θ_{30}	4	7
θ_{6}	2	5
θ_{3}	2	5
Gel strength [10 sec / 10 min]	2,5/11,5	7/15
Density [ppg]	8,5	9,7

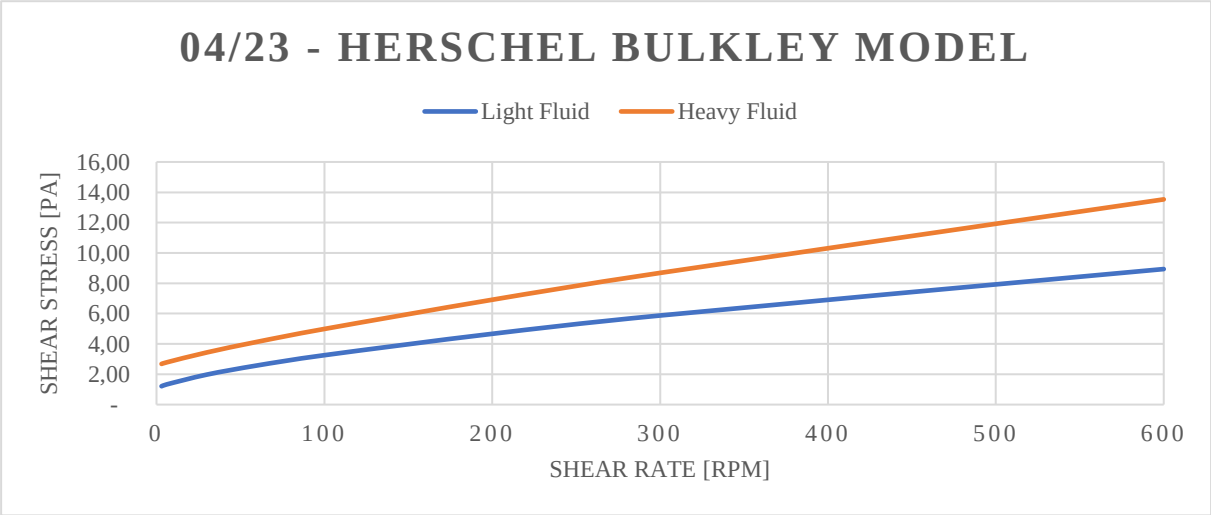

Figure A 27 - Herschel Bulkley Model for experiment 04/23

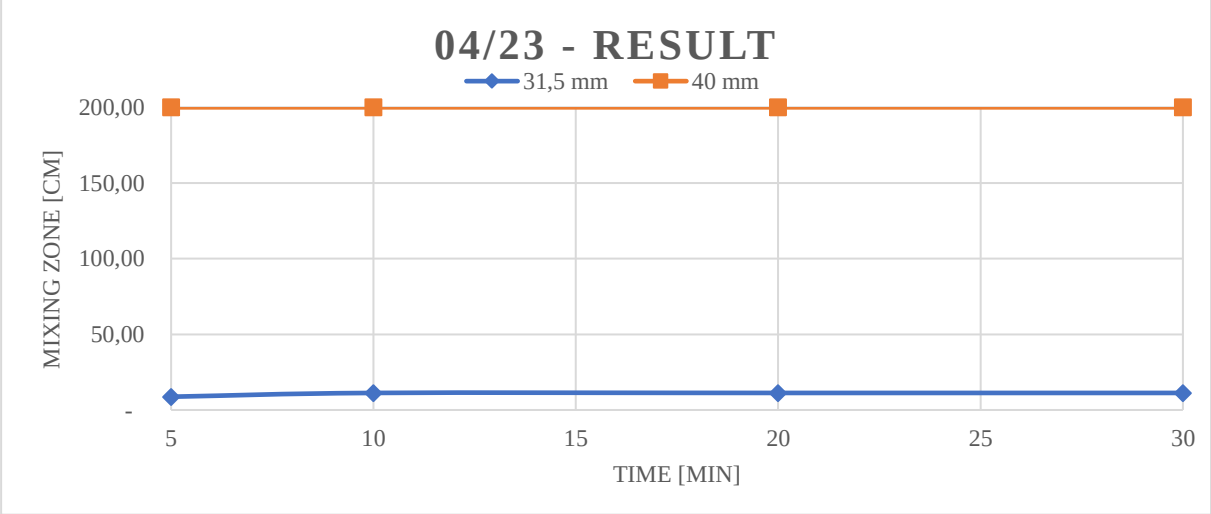

Figure A 28 - Results for experiment 04/23

Table A. 17 - Directly read laboratory values for experiment 04/24

EXPERIMENT 04/24		
Viscometer readings	Light fluid	Heavy Fluid
θ_{600}	16,5	26
θ_{300}	11,5	17,5
θ_{200}	8,5	13
θ_{100}	7	9,5
θ_{60}	5,5	8
θ_{30}	4	7
θ_{6}	2,5	5
θ_{3}	2	5
Gel strength [10 sec / 10 min]	3/13	7/15
Density [ppg]	8,55	9,85

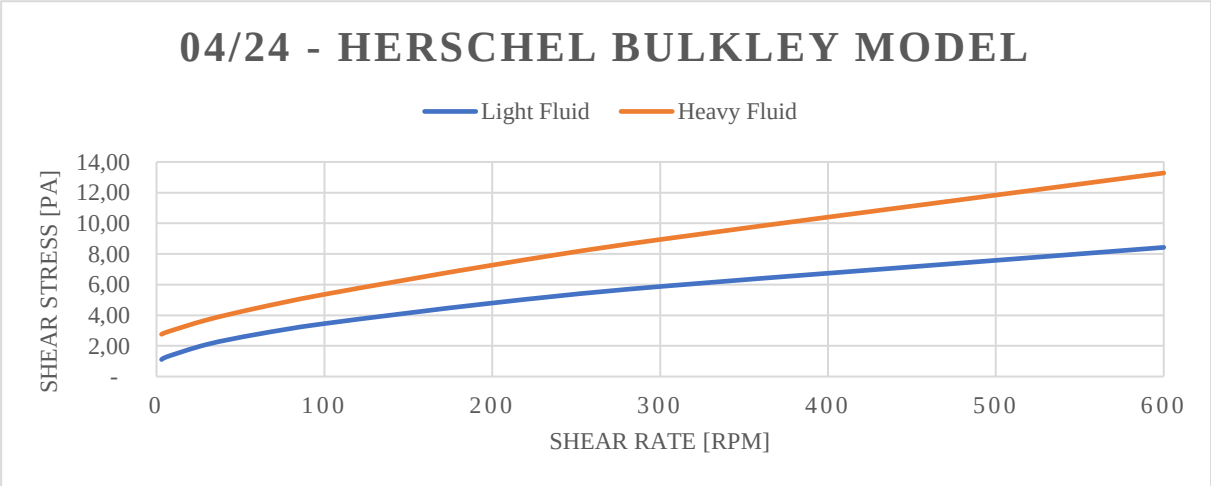

Figure A 29 - Herschel Bulkley Model for experiment 04/24

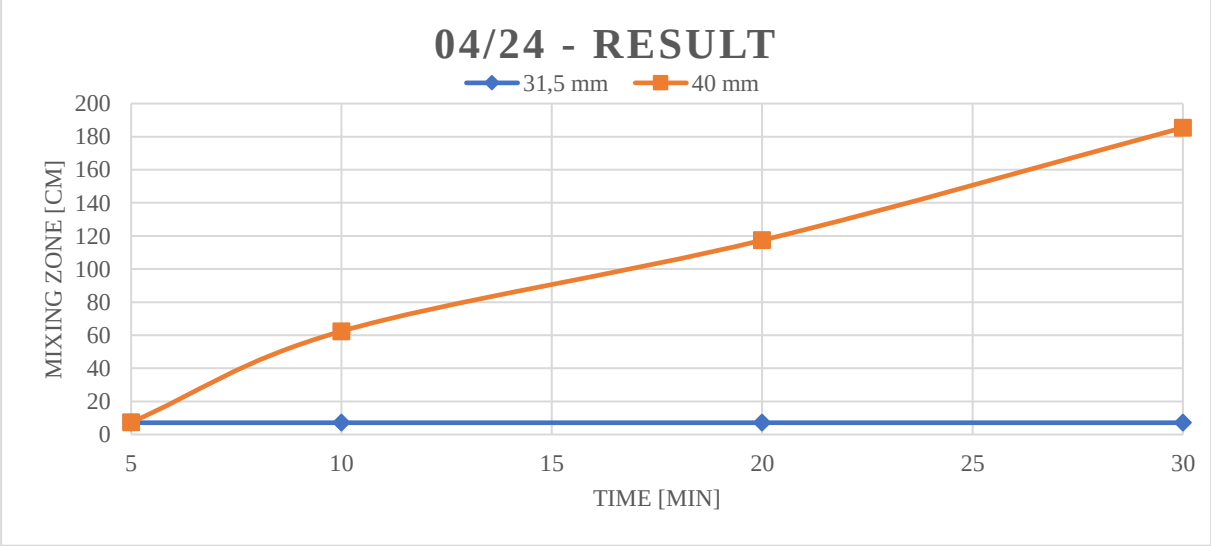

Figure A 30 - Results for experiment 04/24

Table A. 18 - Directly read laboratory values for experiment 04/27

EXPERIMENT 04/27		
Viscometer readings	Light fluid	Heavy Fluid
θ_{600}	29	71
θ_{300}	20,5	47
θ_{200}	16,5	38
θ_{100}	12,5	28
θ_{60}	11	24
θ_{30}	9	21
θ_{6}	7	18
θ_{3}	7	18
Gel strength [10 sec / 10 min]	10/15	22/37
Density [ppg]	9,3	14,75

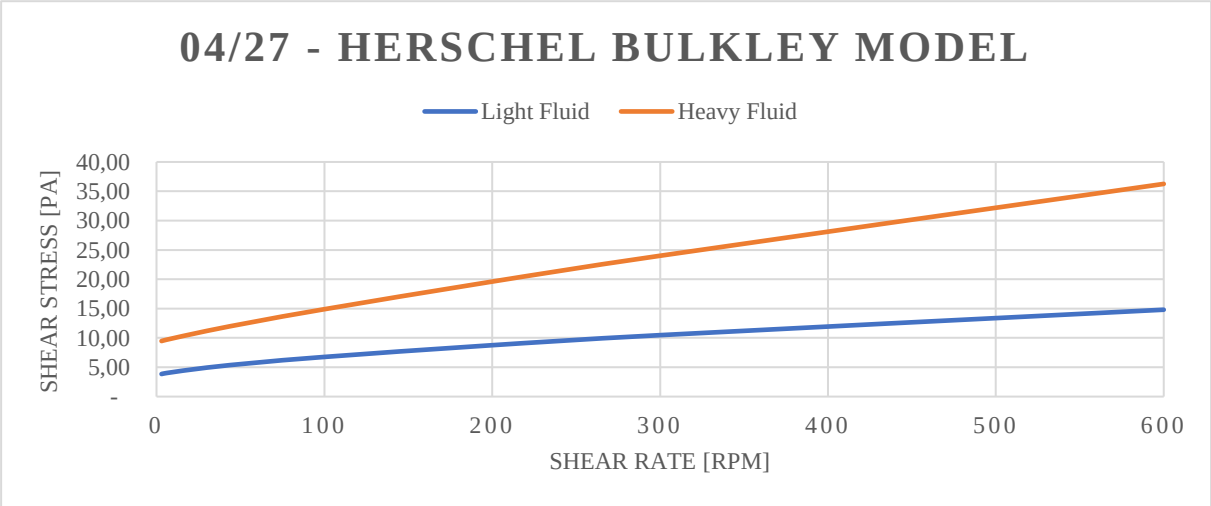

Figure A 31 - Herschel Bulkley Model for experiment 02/27

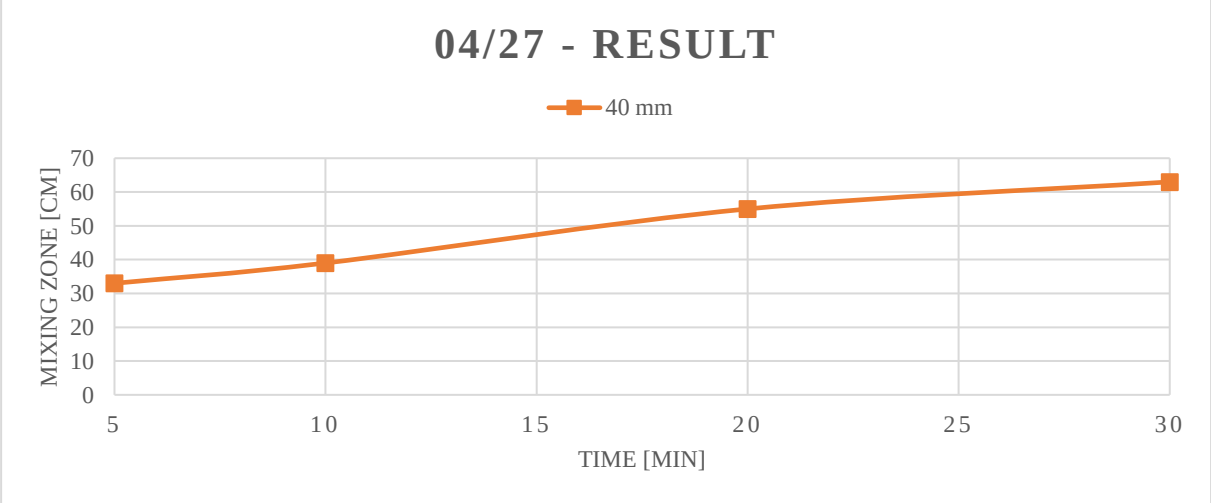

Figure A 32 - Results for experiment 04/27

Table A. 19 - Directly read laboratory values for experiment 04/30

EXPERIMENT 04/30 - 1		
Viscometer readings	Light fluid	Heavy Fluid
θ_{600}	29	44
θ_{300}	20	27
θ_{200}	16,5	21
θ_{100}	11,5	14
θ_{60}	10	12
θ_{30}	9	10
θ_{6}	7,5	8
θ_{3}	7,5	8
Gel strength [10 sec / 10 min]	11/20	9/21
Density [ppg]	9,3	13,1

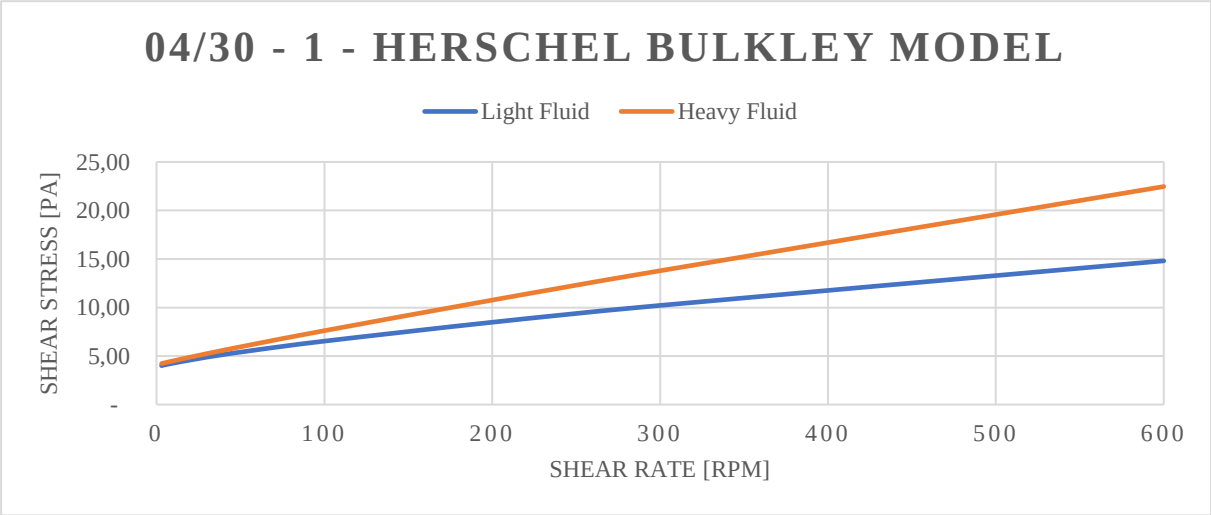

Figure A 33 - Herschel Bulkley Model for experiment 04/30 – 1

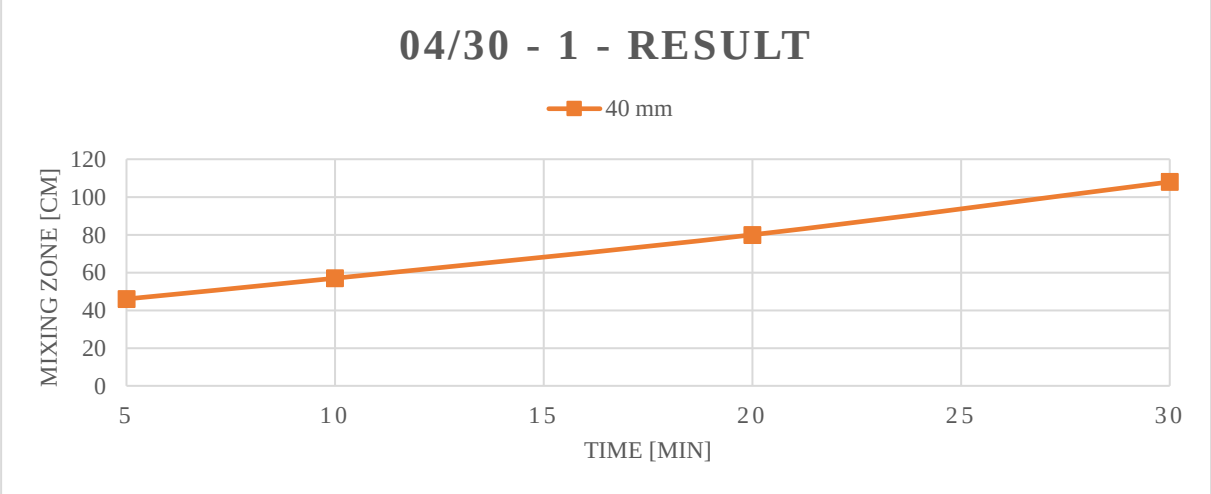

Figure A 34 - Results for experiment 04/30

Table A. 20 - Directly read laboratory values for experiment 05/03

EXPERIMENT 05/03		
Viscometer readings	Light fluid	Heavy Fluid
θ_{600}	20,5	33
θ_{300}	14	22,5
θ_{200}	11,5	18
θ_{100}	8	13,5
θ_{60}	6,5	12,5
θ_{30}	5,5	10
θ_{6}	5	9
θ_{3}	5	9
Gel strength [10 sec / 10 min]	7/13,5	12,5/20
Density [ppg]	8,6	10,4

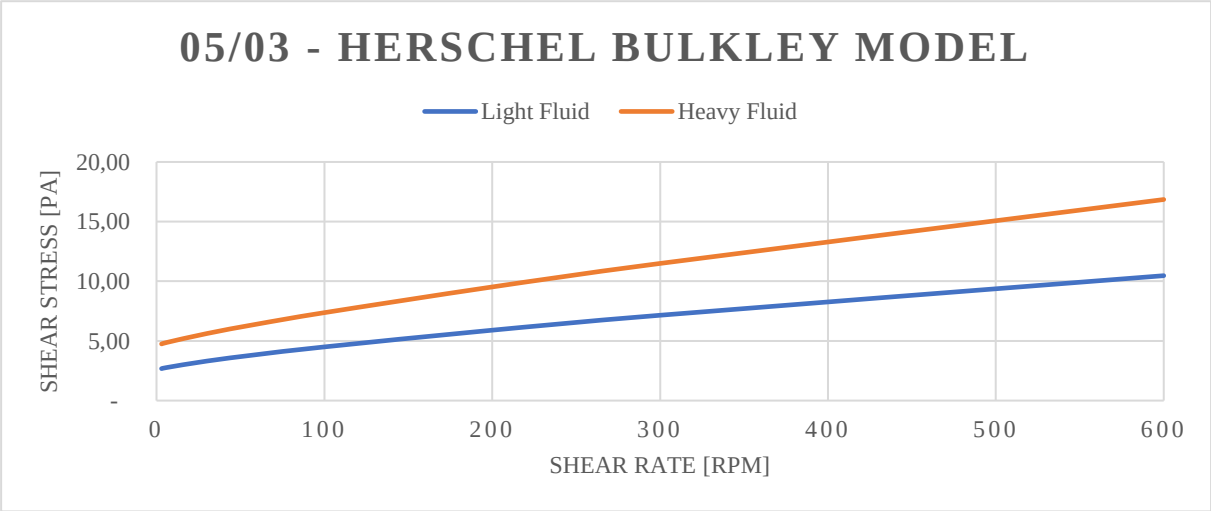

Figure A 35 - Herschel Bulkley Model for experiment 05/03

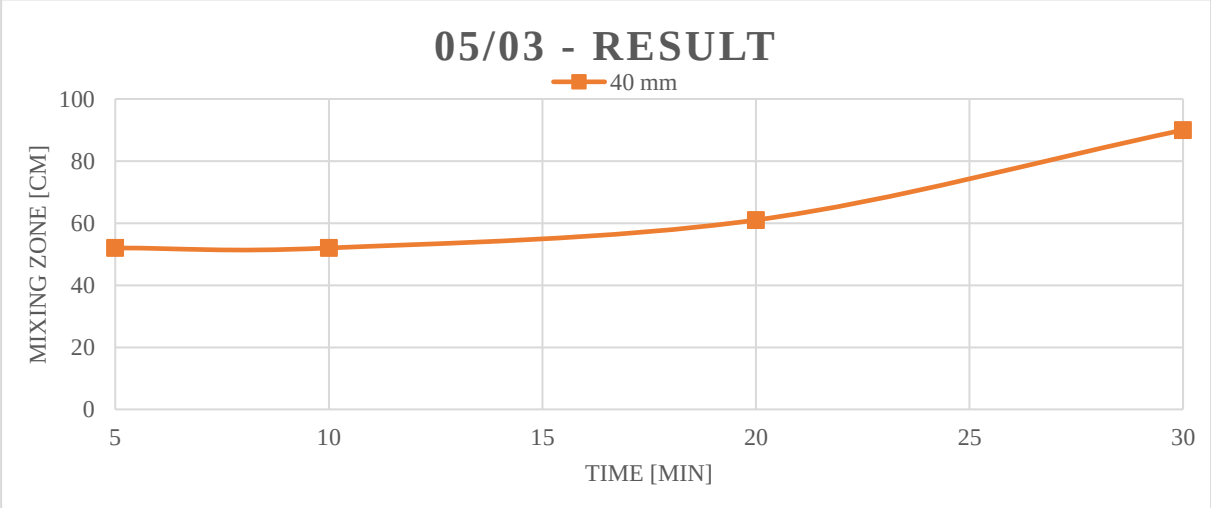

Figure A 36 - Results for experiment 05/03

Table A. 21 - Directly read laboratory values for experiment 05/09

EXPERIMENT 05/09		
Viscometer readings	Light fluid	Heavy Fluid
θ_{600}	24,5	34,5
θ_{300}	18	26
θ_{200}	15	22
θ_{100}	11,5	17
θ_{60}	10,5	16
θ_{30}	8,5	15
θ_{6}	8	12
θ_{3}	8	12
Gel strength [10 sec / 10 min]	10/21,5	15/25
Density [ppg]	8,6	10,1

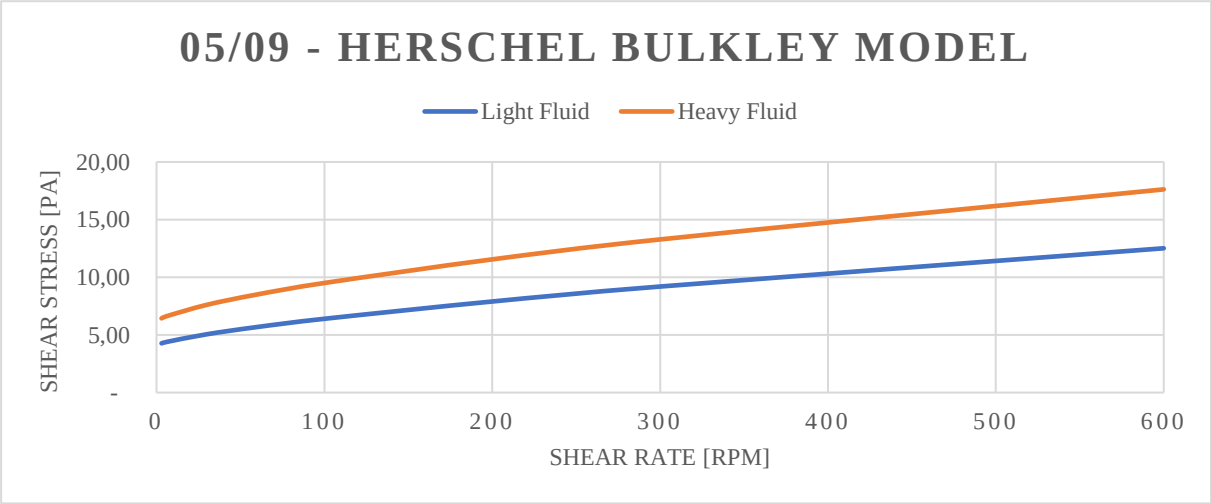

Figure A 37 - Herschel Bulkley Model for experiment 05/09

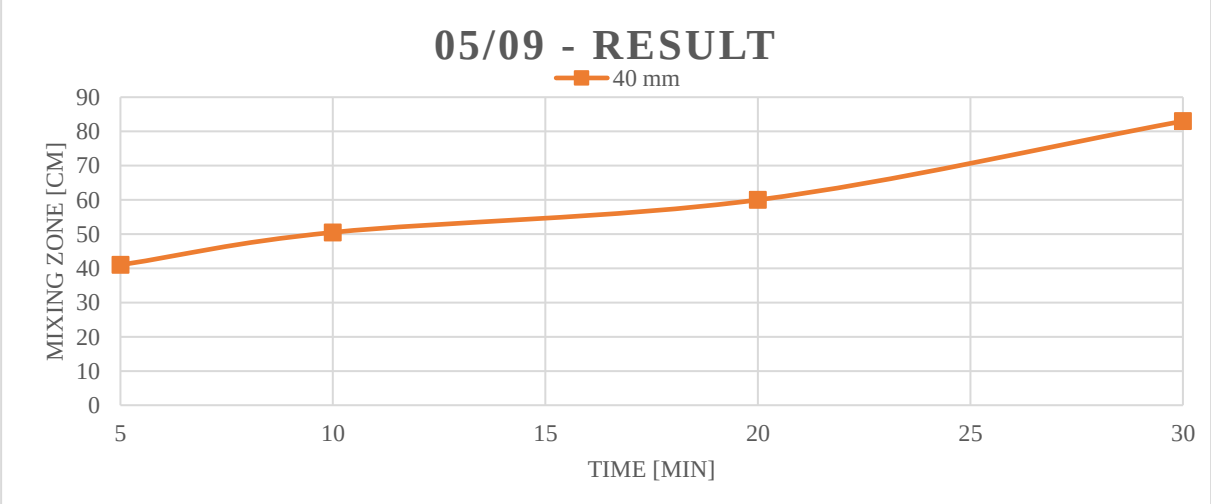

Figure A 38 - Results for experiment 05/09

APPENDIX D – EXPERIMENTAL RESULTS

All vertical experimental results are listed in the table below, where method *V* states that the visual analysis procedure of mixing zone determination is used and method *M* states that the MatLab analysis procedure for mixing zone determination is used.

Table A. 22 - All experimental results

			Light fluid			Heavy fluid						Mixing zone [cm]				
ID well bore / test #	**OD Drill string**	**Clearance [mm]**	**ρ [s.g.]**	**PV [cP]**	**LSYS [HB]**	**ρ [s.g.]**	**PV [cP]**	**LSYS [HB]**	**Δρ**	**ΔPV**	**ΔLSYS**	**5 min**	**10 min**	**20 min**	**30 min**	**Method**
10 mm																
03/19 - 3	7.3	2.7	1.03	8.5	13.5	1.12	8.5	13.5	0.09	0	0	0.60	2.40			V
19,3 mm																
03/21 - 1	14.8	4.5	1.02	5.5	6	1.12	6	18	0.1	0.5	12	3.40	3.80	8.00	14.00	V
03/23 - 1	7.3	12	1.02	6.5	7.5	1.116	7.5	20	0.096	1	12.5	3.40	3.40	4.60	5.60	V
03/23 - 2	14.8	4.5	1.02	6.5	7.5	1.116	7.5	20	0.096	1	12.5	0.40	1.40	3.60	6.60	V
04/11 - 2	14.8	4.5	1.032	6	6.5	1.116	8.5	13	0.084	2.5	6.5	8.00	10.40	14.40	14.40	V
04/12 - 2	14.8	4.5	1.026	5.5	1	1.164	9.5	7.5	0.138	4	6.5	16.47	16.47	16.47	16.47	M
04/13 - 2	14.8	4.5	1.02	6	1	1.164	8	13	0.144	2	12	11.62	17.34	26.20	27.19	M
04/15 - 2	14.8	4.5	1.032	5.5	1	1.164	11	11.5	0.132	5.5	10.5	30.35	34.54	39.77	47.10	M
04/17 - 2	14.8	4.5	1.026	7	1.5	1.164	10	19.5	0.138	3	18	8.52	10.41	16.09	17.99	M
04/19 - 2	14.8	4.5	1.032	8	3.5	1.134	7.5	20.5	0.102	-0.5	17	4.27	4.27	12.82	23.50	M
04/23 - 3	14.8	4.5	1.02	6	2	1.164	9.5	5	0.144	3.5	3	1.08	1.08	6.48	9.72	M
31,5 mm																
03/01 - 1	20.2	11.3	1.02	5.5	1	1.194	9.5	12	0.174	4	11	19.40	19.80			V
03/19 - 1	20.2	11.3	1.1	7.5	11	1.21	10.5	16	0.11	3	5	0.40	1.60	1.60		V
03/19 - 2	20.2	11.3	1.1	8	8	1.3	12	13	0.2	4	5	1.60	2.00	2.00	2.00	V

03/21 - 2	20.2	11.3	1.02	5.5	6	1.12	6	18	0.1	0.5	12	1.30	7.79	7.79	7.79	M
04/04 - 1	25.3	6.2	1.02	4.5	3.5	1.134	8.5	7	0.114	4	3.5	8.59	13.95	20.39	24.69	M
04/04 - 2	20.2	11.3	1.02	4.5	3.5	1.134	8.5	7	0.114	4	3.5	1.18	4.71	7.07	7.07	M
04/11 - 1	25.3	6.2	1.032	6	6.5	1.116	8.5	13	0.084	2.5	6.5	8.73	11.22	11.72	12.47	M
04/12 - 1	25.3	6.2	1.026	5.5	1	1.164	9.5	7.5	0.138	4	6.5	11.7	200	200	200	M
04/13 - 1	25.3	6.2	1.02	6	1	1.164	8	13	0.144	2	12	17.13	22.83	23.98	28.54	M
04/15 - 1	25.3	6.2	1.032	5.5	1	1.164	11	11.5	0.132	5.5	10.5	36.06	40.07	50.08	200.00	M
04/17 - 1	25.3	6.2	1.026	7	1.5	1.164	10	19.5	0.138	3	18	17.04	23.43	28.12	32.38	M
04/19 - 1	25.3	6.2	1.032	8	3.5	1.134	7.5	20.5	0.102	-0.5	17	5.02	5.02	13.81	13.81	M
04/23 - 2	20.2	11.3	1.02	6	2	1.164	9.5	5	0.144	3.5	3	8.76	11.27	11.27	11.27	M
04/24 - 2	20.2	11.3	1.02	5	1.5	1.182	8.5	5	0.162	3.5	3.5	7.12	7.12	7.12	7.12	M
40 mm																
04/23 - 1	25.3	14.7	1.02	6	2	1.164	9.5	5	0.144	3.5	3	200	200	200	200	M
04/24 - 1	25.3	14.7	1.02	5	1.5	1.182	8.5	5	0.162	3.5	3.5	7.4	62.4	117.4	185.4	V
04/27 - 2	25.3	14.7	1.11	9	10	1.5	20	18	0.39	11	8	33	39	55	63	V
04/30 - 1	25.3	14.7	1.11	9	7.5	1.572	17	8	0.462	8	0.5	46	57	80	108	V
05/03	25.3	14.7	1.032	6.5	5	1.248	10.5	9	0.216	4	4	52	52	61	90	V
05/09	25.3	14.7	1.032	6.5	8	1.212	8.5	12	0.18	2	4	41	50.5	60	83	V

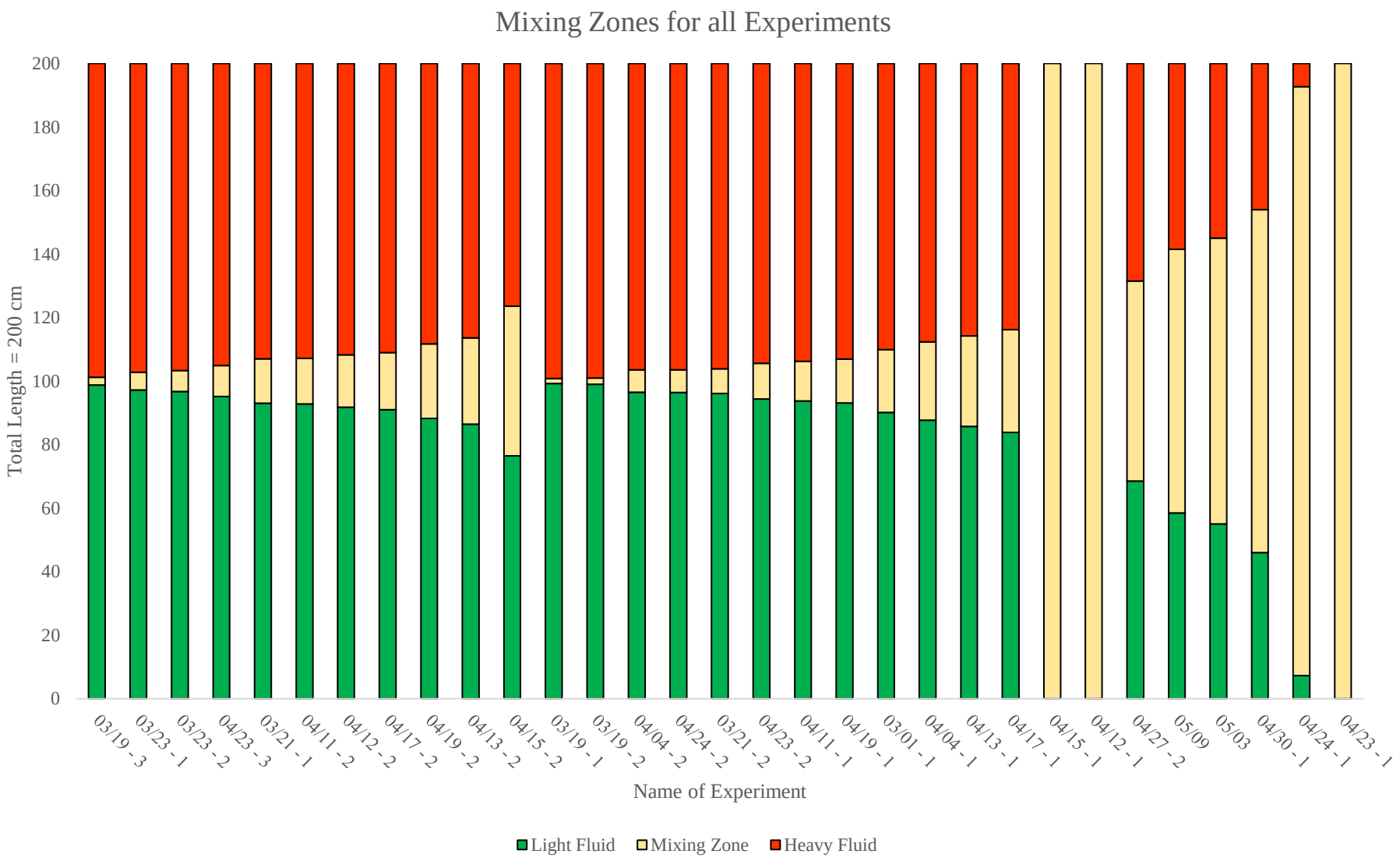

Figure A 39 - Graphic illustration of the mixing zones for all experiments